**Title**

Computer-Assisted Navigation Techniques for MRI-Guided Percutaneous Interventions

**Author**

Li, Xinzhou

**Publication Date**

2021

UNIVERSITY OF CALIFORNIA
Los Angeles

# Computer-Assisted Navigation Techniques for MRI-Guided Percutaneous Interventions

A dissertation submitted in partial satisfaction of the
requirements for the degree Doctor of Philosophy
in Bioengineering

by

Xinzhou Li

2021

# ABSTRACT OF THE DISSERTATION

## Computer-Assisted Navigation Techniques for MRI-Guided Percutaneous Interventions

by

Xinzhou Li
Doctor of Philosophy in Bioengineering
University of California, Los Angeles, 2021
Professor Holden H. Wu, Chair

Image-guided minimally invasive percutaneous interventions, including needle-based targeted biopsy and focal therapy, play key roles in cancer diagnosis and treatment. With excellent soft tissue contrast and the absence of ionizing radiation, magnetic resonance imaging (MRI) has become a promising imaging modality for intra-procedural and real-time guidance of percutaneous interventions. However, MRI-guided percutaneous interventions still face two main challenges: limited access to patients inside the scanner and tissue displacement due to physiological motion. MRI-compatible remotely controlled systems for instrument manipulation inside the scanner are being developed to address the first challenge. To address the second challenge, computer-assisted navigation methods using intra-procedural and real-time MRI are being investigated to provide essential information regarding tissue and instrument positions to guide percutaneous interventions.

Accurate tissue motion tracking and automatic needle localization techniques are the core components for computer-assisted navigation. Respiratory motion remains the main challenge for procedures in abdominal organs. The tissue target tracking accuracy is negatively impacted by the system latency of the MRI acquisition, reconstruction, and processing pipeline. In addition, passive needle tracking using MR images is challenged by variations of the needle-induced signal void feature in different situations. Discrepancies between the needle feature position on MRI and the underlying physical needle position could increase needle localization errors during procedures. Therefore, this dissertation aims to address these challenges by establishing new computer-assisted navigation techniques for MRI-guided interventions, including prediction of tissue motion due to respiration using fusion-based multi-rate Kalman filtering and deep learning-based needle localization methods.

Firstly, this work investigated image-based and surrogate-based motion tracking methods using real-time golden-angle radial MRI to achieve real-time MRI guidance for interventions in organs affected by respiration (e.g., liver). Images with different temporal footprints were reconstructed from the same golden-angle radial MRI data stream to simultaneously enable image-based and surrogate-based tracking at 10 Hz. Phantom experiments confirmed that the median online tracking error of image-based tracking was lower than surrogate-based methods, however, with higher median system latency. This work proposed a new fusion-based respiratory motion prediction framework to combine the lower tracking error of image-based tracking with the lower latency of surrogate-based tracking. The fusion-based method was evaluated in retrospective studies using *in vivo* real-time free-breathing liver MRI. The motion prediction accuracy of the proposed framework achieved low-latency feedback with improved accuracy compared with image-based and surrogate-based methods.

Next, to develop an automatic needle tracking algorithm for MRI-guided interventions, this work adapted the Mask Region Proposal-Based Convolutional Neural Network (R-CNN) to localize the passive needle features on MRI. Mask R-CNN was adapted and trained to segment the needle feature using intra-procedural images from MRI-guided prostate biopsy cases and real-time images from MRI-guided needle insertion in *ex vivo* tissue. The segmentation masks were passed into a needle feature localization algorithm to extract the needle feature tip location and axis orientation. The proposed algorithm was evaluated on MR images from *in vivo* intra-procedural prostate biopsy cases and *ex vivo* real-time MRI experiments with a range of different conditions. It achieved pixel-level tracking accuracy in real time and has the potential to assist MRI-guided percutaneous interventions.

Lastly, to overcome in-plane and through-plane discrepancies between the needle feature position on MRI and the underlying physical needle position, this work developed a deep learning-based framework to automatically localize the physical needle position using single-slice and 3-slice MRI. The proposed framework consists of two Mask R-CNN stages. Physics-based simulations were performed to generate single-slice and 3-slice images with needle features from a range of underlying needle positions and MRI parameters to form datasets for training the single-slice and 3-slice physical needle Mask R-CNN models. Using the single-slice model, the proposed physics-driven Mask R-CNN framework achieved sub-millimeter physical needle localization accuracy on single-slice images aligned with the needle. The 3-slice model further reduced the through-plane physical needle localization error in situations where the imaging plane may be misaligned with the needle. Both frameworks can achieve physical needle localization in real time for interventional MRI.

The dissertation of Xinzhou Li is approved.

David Lu

Kyunghyun Sung

Tsu-chin Tsao

Holden H. Wu, Committee Chair

University of California, Los Angeles

2021

*Dedicated to my parents:*

*Tieming Li & Wenjing Yang*

# TABLE OF CONTENTS

# LIST OF TABLES

# LIST OF FIGURES

# LIST OF EQUATIONS

# ACKNOWLEDGEMENTS

Foremost, I would like to express my sincere gratitude to my advisor, Dr. Holden Wu, who leads me to an amazing research field and provide endless support, patience, and guidance on my Ph.D. study and research. His technical and editorial advice was essential to the completion of this dissertation. Moreover, his insightful vision, enthusiasm for research, and immense knowledge keep motivating me to pursue the best version myself. It is fortunate to have Dr. Wu as my advisor.

I would like to thank the rest of my committee members Dr. David Lu, Dr. Kyung Sung and Dr. Tsu-chin Tsao and oral qualifying exam committee member Dr. Peng He. They helped me explore my research topic in different perspectives and clearly understand the motivations of the study. Their precious advice helped me refine my project and improve the technical developments.

I would like to thank my collaborators for helping my research or allow me to gain lots of knowledge from their interesting projects. I want to express my special gratitude to Dr. James Simonelli, Dr. Yu-Hsiu Lee, and Pengkang Yu from Mechatronics and Controls Laboratory. The mechanical system they built and their help to operate the system are essential for completing this dissertation. I also want to thank Dr. Adam Young for image annotation and precious advice as a clinical expert. Furthermore, I want to thank Dr. Steven Raman and Dr. David Lu for leading me to observe clinical procedures and provide guidance for my research from clinical perspectives. Moreover, I want to thank Siemens MRI scientists Dr. Xiaodong Zhong and Dr. Florian Maier for helpful discussions on my needle tracking project.

I felt grateful to join Magnetic Resonance Research Labs and have an incredible journey with all the past and current members. I would like to give special thanks to Dr. Tess Armstrong and Samantha Mikaiel. As senior lab members from Dr. Wu's lab, they helped me fit into the lab and get familiar with MRI research at the beginning. Their suggestions on both research and life benefit me throughout my graduate studies. I also want to thank the TRIC staff who organize the research scanner and all MRI technologists for helping me during the scans.

Last but not least, I would give my deep gratitude to my parents, Tieming Li and Wenjing Yang. They always show their unconditional love from their hearts and support me as much as they can.

# VITA

## Education

Ph.D. in Bioengineering, University of California Los Angeles (2015-2021)

B.S. in Biomedical Engineering and Mechanical Engineering, Pennsylvania State University, University Park (2010-2014)

## Honors & Awards

ISMRM Magna Cum Laude Award (2021)
ISMRM Summa Cum Laude Award (2019)
SCMR Travel Grant (2019)
ISMRM Educational Stipend (2017-2019)
ISMRM New Entrant Stipend (2015)
UCLA Bioengineering PhD fellowship (2015-2016)
Penn State College of Engineering Capstone Design Best Project Award 2nd place (2014)

## Peer Reviewed Publications

1. **Li X**, Young AS, Raman SS, Lu DS, Lee Y, Tsao TC, Wu HH. Automatic Needle Tracking using Mask R-CNN for MRI-Guided Percutaneous Interventions. International Journal of Computer Assisted Radiology and Surgery 2020; 15(10):1673-1684.

2. **Li X**[†], Perotti LE[†], Martinez JA, Duarte-Vogel, SA, Ennis DB, Wu HH. Real-Time 3T MRI-Guided Cardiovascular Catherization in a Porcine Model using a Glass-Fiber Epoxy-Based Guidewire. PLOS ONE 2020; 15(2): e0229711. ([†]equal contribution)

3. **Li X**, Lee Y, Mikaiel S, Simonelli J, Tsao TC, Wu HH. Respiratory Motion Prediction using Fusion-Based Multi-Rate Kalman Filtering and Real-Time Golden-Angle Radial MRI. IEEE Transactions on Biomedical Engineering 2020; 67(6): 1727-1738.

4. Lee Y, **Li X**, Simonelli J, Lu D, Wu HH, Tsao TC. Adaptive Tracking Control of One-Dimensional Respiration Induced Moving Targets by Real-Time Magnetic Resonance Imaging Feedback. IEEE/ASME Transactions on Mechatronics 2020; 25(4): 1894-1903.

5. Mikaiel S, Simonelli J, **Li X**, Lee Y, Lee YS, Sung K, Lu D, Tsao TC, Wu HH. MRI-Guided Targeted Needle Placement During Motion using Hydrostatic Actuators. The International Journal of Medical Robotics and Computer Assisted Surgery 2020; 16(2): e2041.

6. Simonelli J, Lee Y, Chen C, **Li X**, Mikaiel S, Lu D, Wu HH, Tsao TC. Hydrostatic Actuation for Remote Operations in MR Environment. IEEE/ASME Transactions on Mechatronics 2020; 25(2): 894-905.

7. Deng T, Zhang L, **Li X**, Jeffrey Z, Wu HH. Responsive Nanoparticles to Enable a Focused Ultrasound-Stimulated Magnetic Resonance Imaging Spotlight. ACS Nano 2021; in press.

8. Zhong X, Armstrong T, Gao C, Nickel MD, Han F, Dale BM, **Li X**, Kafali SG, Hu P, Wu HH, Deshpande V. Accelerated k-Space Shift Calibration for Free-Breathing Stack-of-Radial MRI Quantification of Liver Fat and $R_2$*. Magnetic Resonance in Medicine 2021; in press.

9. Martin T, Janzen C, **Li X**, Del Rosario I, Chanlaw T, Choi S, Armstrong T, Masamed R, Wu HH, Devaskar SU, Sung K. Characterization of Uterine Motion in Early Gestation using MRI-Based Motion Tracking. Diagnostics 2020; 10(10):840.

10. Zhong X, Hu HH, Armstrong T, **Li X**, Lee Y, Tsao TC, Nickel MD, Kannengiesser SAR, Dale BM, Deshpande V, Kiefer B, Wu HH. Free-Breathing Volumetric Liver $R_2$* and Proton-Density Fat Fraction Quantification in Pediatric Patients Using Stack-of-Radial MRI with Self-Gating Motion Compensation. Journal of Magnetic Resonance Imaging 2020; 53(1):118-129.

11. Zhang L, Armstrong T, **Li X**, Wu HH. A Variable Flip Angle Golden-Angle-Ordered 3D Stack-of-Radial MRI Technique for Simultaneous Proton Resonant Frequency Shift and $T_1$-Based Thermometry, Magnetic Resonance in Medicine 2019; 82(6): 2062-2076.

## Selected Conference Abstracts

1. **Li X**, Lee Y, Lu D, Tsao TC, Wu HH. Deep Learning-Driven Automatic Scan Plane Alignment for Needle Tracking in MRI-Guided Interventions. Proceedings of the ISMRM 29th Annual Meeting, 2021, p0861. (Magna Cum Laude)

2. **Li X**, Lee Y, Tsao TC, Wu HH. Physical Needle Localization using Mask R-CNN for MRI-Guided Percutaneous Interventions. Proceedings of the ISMRM 28th Annual Meeting, Paris, France, 2020, p4144.

3. **Li X**, Raman SS, Lu D, Lee Y, Tsao T, Wu HH. Real-Time Needle Detection and Segmentation using Mask R-CNN for MRI-Guided Interventions. Proceedings of the ISMRM 27th Annual Meeting, Montreal, Canada, 2019, p972. (Summa Cum Laude)

4. **Li X**, Perotti LE, Martinez JA, Ennis DB, Wu HH. Real-Time 3T MRI-Guided Cardiovascular Catherization in a Porcine Model using a Glass-Fiber Based MR Guidewire. Proceedings of the 22nd Annual SCMR Scientific Sessions, Bellevue, USA, 2019.

5. **Li X**, Mikaiel S, Wu HH. Motion Prediction using a Multi-Rate Kalman Filter with Golden Angle Radial Acquisition for Real-Time MRI-Guided Interventions. Proceedings of the ISMRM 26th Annual Meeting, Paris, France, 2018, p4151.

6. **Li X**, Mikaiel S, Simonelli J, Lee Y, Tsao TC, and Wu HH. Real-Time Motion Prediction for Feedback Control of MRI-Guided Interventions. Proceedings of the ISMRM 25th Annual Meeting, Honolulu, USA, 2017, p5540.

# Chapter 1 Introduction

## 1.1 Significance

Diagnostic and therapeutic image-guided minimally invasive percutaneous interventions are becoming routine in clinical cancer management[1,2]. Procedural accuracy for needle-based targeted biopsy and focal therapy is essential for safe and effective clinical outcomes of these interventions. Conventional imaging modalities such as computed tomography (CT) and US (ultrasound) lack the consistent lesion visualization required to precisely localize tumors[3,4]. Fortunately, magnetic resonance imaging (MRI) provides excellent soft tissue contrast, which enables proper identification of both target lesions and structures that are critical to avoid (i.e., blood vessels). In addition, MRI has no ionizing radiation exposure for both physicians and patients, which could support continuous image guidance[5].

However, performing continuous guidance using MRI during an interventional procedure is currently impractical because conventional closed-bore MRI scanners restrict physicians' access to patients. Existing clinical workflows leverage MRI for intra-procedural guidance with in-bore device manipulations using freehand or step-and-shoot workflows. The generalizability of freehand procedures is limited because a specialized MRI scanner choice (i.e., open bore or short bore) may be required[6]. In the meantime, step-and-shoot workflows are widely adopted at multiple clinical sites for different types of procedures in the conventional MRI scanner[7-9]. These approaches may often require prolonged procedural time with iterative needle adjustment to achieve adequate targeting accuracy since they lack continuous image guidance.

Remotely controlled systems for manipulating instruments inside the MRI scanner, such as MR-compatible needle actuators and robotic systems, are being developed to address this challenge[10-12]. With improved imaging sequences and reconstruction speed, real-time MRI enables continuous visualization of target lesions and needles to provide timely visual feedback[13,14]. However, tissue displacement due to physiological motion could increase manual needle operation error, undermining the overall accuracy and time efficiency of procedures. Therefore, with the development of computer-assisted navigation methods, key information regarding tissue and instrument positions can be acquired through real-time MRI feedback to achieve dynamic guidance and control of the instrument to treat moving targets, thus further expanding clinical applications of MRI-guided percutaneous interventions.

## 1.2 Image-Guided Percutaneous Interventions

Image-guided percutaneous interventions play key roles in cancer diagnosis and treatment. Under image guidance, physicians manipulate needles to access targets in suspected lesions for different purposes. These include well-established needle-based targeted biopsy approaches that allow for retrieval of tissue specimens for cancer diagnosis in multiple organs of the body such as brain, breast, liver, lungs, prostate, etc.[2]. In addition, image-guided focal therapies, including needle-directed procedures such as laser ablation and radiofrequency ablation, have gained popularity for cancer treatment[15]. Compared with other established treatment options like surgical resection, ablation can preserve tissue and treat localized cancer with low rates of morbidity[16].

Overall, medical imaging can help to precisely localize target lesions and device positions to guide targeting procedures for percutaneous interventions. However, for targets in the abdomen, there are extra procedural challenges caused by physiological motion. CT and US are the most commonly used intra-procedural image modalities to guide a variety of procedures[17,18]. However, the overall effectiveness of CT and US guidance is still limited for multiple reasons. US is an established modality for dynamic procedural guidance, however, low signal-to-noise ratio (SNR) and acoustic window restrictions limit visualization of deep and small tumors using US[4]. Noncontrast CT lacks direct visualization of small and artifact-obscured lesions, while enhancement of lesions from injected contrast materials is only temporary and cannot last over the whole procedure[3]. Although CT fluoroscopy (CTF) has the potential to provide dynamic visualization of interventional devices and moving targets to improve guidance and allow fast response to intraoperative complications[19], continuous image guidance using CTF is not widely accepted due to the concern about radiation exposure to both patients and physicians.

## 1.3 MRI-Guided Percutaneous Interventions

MRI has become an essential medical imaging technique to create qualitative and quantitative images that capture anatomical and physiological information of the human body. Conventional MRI has been performed as a non-invasive diagnostic test for different types of diseases. With excellent soft tissue contrast, MRI can visualize different types of cancerous lesions and critical structures to avoid during interventions[20]. These advantages position MRI as a powerful pre-procedural imaging modality to identify lesion targets and create a roadmap for procedures in the planning stage[21]. Image fusion methods have been developed to register rapid intra-procedural images such as from US or X-ray fluoroscopy (XRF) to the planning roadmap on MRI. However, the overall targeting accuracy may suffer from errors due to misregistration between different modalities[22].

MRI can also provide needle visualization based on the passive signal void feature on the MR images caused by needle-induced susceptibility effects to guide needle manipulation during procedures. For example, during intra-procedural or real-time MRI-guided interventions, needle-in scans are used to visualize both the needle feature and the target to assist needle position adjustment[7]. Thus, with additional advantages of MRI, including multiplanar volumetric imaging and no ionizing radiation exposure to both physicians and patients, it has emerged as a promising intra-procedural imaging modality.

One major limitation of MRI guidance is insufficient access of physicians to patients inside the scanner because of the long and narrow size of the conventional MRI bore (diameter ≤ 70 cm, length in the range of 125–160 cm). Open-configuration low-field MRI systems have been developed for certain patient groups with claustrophobia and extreme obesity or to dedicate to interventional purposes[23-25]. Freehand in-bore device manipulation with interactive MRI guidance can be performed. However, it has not become a clinical routine because this unique scanner type is rarely available at clinical sites, as open-configuration designs could lower signal-to-noise ratio (SNR) and amplify field inhomogeneity, further impairing the image quality. A variety of studies using the freehand approach were performed on short-bore MRI such as Siemens Espree 1.5T MRI system with a wide bore of 70 cm diameter and 125 cm length[5,26,27]. However, the advantages of clinical translation are unclear as short-bore scanners are not widely installed, so the general learning curve of the freehand approach is also not well understood. The freehand approach with step-and-shoot workflow in conventional high field scanners (e.g., 3T) has emerged in prostate biopsy, as the pelvis is relatively easier to access[28]. Though the proposed workflow is feasible, it may remain limited to regions of the body that are more accessible and experience less motion.

In the physical space of conventional MRI scanners, physicians have established the step-and-shoot workflow for multiple procedures in more clinical sites to adapt the MRI advantages for percutaneous interventions. A conceptualized diagram summarizes the workflow (**Figure 1-1**), which is consistent among several types of procedures in different organs using different MRI protocols and guidance systems. For example, MRI-guided in-bore prostate biopsy has become a clinical routine in prostate cancer diagnosis. Several cohort studies demonstrated higher prostate cancer detection rates than conventional biopsy by applying MRI-guided procedures[7,29,30]. In the UCLA medical center, the standard step-and-shoot workflow of in-bore prostate biopsy included several key steps: identify suspicious region(s) based on pre-procedural structural and diffusion MRI; initialize needle trajectory planning by localizing fiducial reference markers and target position(s); adjust alignment parameters of an MRI-compatible and visible needle guide based on the planned trajectory; advance the patient into the MRI bore to acquire intra-procedural images to confirm the needle position. If the needle is not on target, further adjustment is required for the needle guide. Such workflow is quite time-consuming because physicians need to repeatedly transfer patients into and out of the scanner bore to adjust the needle position between intermittent imaging. The cumbersome step-and-shoot steps mainly result from separate needle manipulation steps and image guidance steps, which may lead to inadequate targeting accuracy or prolonged procedure time because there is no instant feedback.

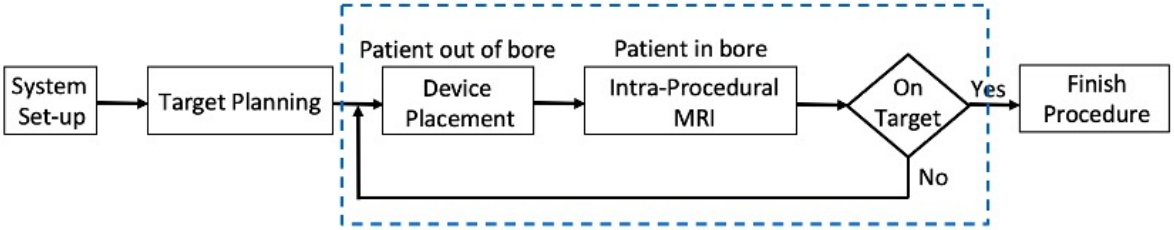

**Figure 1-1 Conceptual diagram of a standard step-and-shoot workflow. Blue dashed box indicates the most time-consuming part of iterative needle adjustment and confirmation.**

## 1.4 Emerging Technologies for MRI-Guided Interventions

### 1.4.1 Remote Controlled Robotic System

To address challenges of restricted space in the conventional close-bore MRI scanner, MRI compatible remote-controlled systems are being developed to achieve needle insertion and rotation inside the scanner controlled by operators outside the scanner. For example, a 2 degree of freedom (DOF) remotely actuated needle driver was developed on a body mounted robotic system. Remote needle actuation by human master could be performed with sufficient accuracy via a beaded chain transmission system[11,31]. A novel hydrostatic actuation and transmission network system was developed based on rolling diaphragm fluid actuators to create a needle manipulation module that allows remote needle actuation with collaborations between human and robot masters[12]. These types of systems can benefit from simultaneous MRI guidance, which enables the system to serve as an extended "arm" for freehand or robotic needle manipulation[32].

### 1.4.2 Real-Time MRI Pipeline

For both freehand and robotic-assisted needle manipulation during percutaneous interventions, continuous imaging guidance with real-time MRI provides essential dynamic motion information about the target tissue and needle[33]. The imaging frame rate of real-time MRI is a crucial factor for dynamic procedural guidance[34]. Compared with other established interventional modalities such as the US, XRF, and CTF, MRI has limitations of imaging acquisition and reconstruction speed, which lead to compromises in the image quality, spatial-temporal resolution, temporal footprint, and/or system latencies[14].

Recently, multiple technical developments are being pursued to improve real-time MRI. Steady-state sequences including $T_1$-weighted spoiled gradient echo (GRE) and $T_2$-like balanced steady-state free precession (bSSFP) with short repetition time (TR) can achieve fast image acquisition. However, using conventional Cartesian sampling trajectories for steady-state sequences could reduce the acquisition speed and be sensitive to artifacts caused by motion and undersampling[35-37]. A unique non-Cartesian golden-angle (GA) ordered radial acquisition scheme samples a new readout (radial spoke) every repetition time (TR) by continually rotating the sampling spoke by a golden-ratio angle increment of 111.25°. GA-ordered radial MRI has higher robustness to physiological motion and undersampling effects compared to Cartesian MRI, due to the radial k-space sampling pattern[35-37]. In addition to rapid MR image acquisition, rapid or real-time MR image reconstruction at the scanner is required to provide imaging feedback to the physician throughout a procedure. To implement fast online image reconstruction, an open-source reconstruction platform can be used for the non-Cartesian sequence with GPU acceleration to establish a customized imaging pipeline using GA radial MRI[38].

### 1.4.3 Real-Time Workflow with MRI-Guided Computer-Assisted Navigation

By combining a comprehensive real-time MRI pipeline and remote-controlled system for device manipulation, a new workflow can be established to achieve device placement under simultaneous MRI guidance, which has the potential to improve the overall procedural accuracy and efficiency (**Figure 1-2**). However, two challenges remain for this new workflow: for tissue targets experiencing motion, especially respiratory motion in the abdomen, target tissue displacement may cause mistargeting during interventional procedures[39]; Active device tracking (e.g., tracking coil[40] or fiber Bragg grating sensors[41]) used in existing interventional workflows can be adapted to a real-time workflow[14]. However, the specialized hardware requirements may increase the cost and additional instrument set-up time for the procedural workflow. Alternatively, MRI-guided computer-assisted navigation methods that extract target tissue motion information and needle position directly from the images can be used to provide the real-time feedback necessary to assist the needle manipulation[42-44]. These methods include various computer vision algorithms specific to MRI to automatically perform object detection, registration, segmentation by taking advantage of the tissue and passive device visualization on MRI[14,45,46].

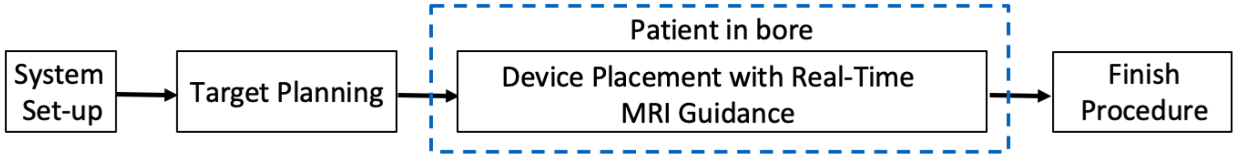

**Figure 1-2 Conceptual diagram of a new MRI-guided intervention workflow with real-time MRI guidance. Device placement can be achieved using manual control or by using a remote-controlled robotic system with real-time MRI feedback.**

## 1.5 Technical Challenges of MRI-Guided Computer-Assisted Navigation

MRI-guided computer-assisted navigation has potential to improve needle-based percutaneous interventions with a real-time workflow. However, computer-assisted navigation faces multiple challenges that may undermine the overall procedure accuracy and efficiency.

Image-based and surrogate-based tracking are two main categories of computer-assisted navigation methods to extract spatial coordinates of target tissue feature motion under respiration from real-time MRI for procedural guidance. Image-based tracking can obtain accurate results, but the motion feedback accuracy is negatively affected by the system latencies, including computational time for MRI reconstruction and image processing[47,48]. Surrogate-based tracking has lower latency but introduces additional tracking errors due to the lower-quality surrogate signal and discrepancies in the correlation motion model[49,50]. Temporal prediction techniques for tracking respiratory motion, such as Kalman filtering, are being developed to reduce the tracking error by considering and accounting for the latency[51]. However, the trade-off between tracking accuracy and system latency in the existing methods could limit the respiratory motion prediction accuracy and there is a lack of studies exploring new ways to overcome this trade-off.

Passive needle visualization based on the signal void feature on the MR images caused by needle-induced susceptibility effects can be applied to localize and track the needle for MRI-guided procedures without additional hardware[7]. The automatic tracking methods using hand-crafted pre-determined feature extraction are challenged by signal void feature variation and contrast difference between the needle feature and surrounding tissues based on different MRI sequence types and parameters, needle materials, and the needle's orientation relative to the main magnetic field ($B_0$) direction[52]. Supervised deep learning using convolutional neural networks (CNN) achieved better performance to overcome the challenges, but residual errors of existing pixel-based segmentation methods using CNNs degrade the instance level detection of the needle feature[53,54]. Additional ensemble methods were required to remove residuals errors that could introduce extra processing time that may lower the overall procedural efficiency[54].

Lastly, discrepancies between the MRI needle feature position and the underlying physical needle position could lead to additional needle tracking errors. This includes both in-plane discrepancies when the imaging plane is perfectly aligned with the needle and through-plane discrepancies. Theses discrepancies may induce errors on the order of 5-10 mm[55], which may lead to mistargeting during procedures (e.g., clinically relevant targets may have diameters of 5-10 mm[56]). Existing approaches to overcome these discrepancies include using special sequences that reduce needle-induced artifact sizes[57] and inverse reconstruction of the physical needle source from multiple images[58,59], but both require substantial increases in acquisition and/or reconstruction time, which is not suitable for interventional procedural guidance.

## 1.6 Specific Aims

The purpose of the dissertation is to develop and evaluate new computer-assisted navigation techniques for MRI-guided interventions by overcoming the existing challenges in respiratory motion prediction and needle tracking. In the long term, these technical breakthroughs will form the foundation for new interventional strategies, such as using an MRI-guided robotic system to achieve feedback-controlled dynamic needle-based procedures in mobile organs, including the liver and kidney, to realize and advance the clinical impact of MRI-guided interventions.

### 1.6.1 Aim 1: Respiratory Motion Prediction Using Fusion-Based Multi-Rate Kalman Filtering and Real-Time Golden-Angle Radial MRI

Chapter 2 presents a novel respiratory motion prediction method that can overcome system latencies of a real-time MRI pipeline to provide accurate feedback information for MRI-guided interventions. This study first investigated the respective advantages of surrogate-based tracking (lower latency) and image-based tracking (lower tracking error) using a custom software pipeline that implements real-time GA radial MRI with motion feedback. Next, a Kalman filter with an expectation-maximization algorithm for stochastic state-space model training was applied to adapt to temporal characteristics of respiratory motion that vary for different subjects and may change over time. Then, this work proposed a fusion-based framework that combines image-based tracking results as a delayed measurement with rapid surrogate-based tracking results in a multi-rate Kalman filter to achieve accurate motion prediction.

### 1.6.2 Aim 2: Automatic Needle Tracking Using Mask R-CNN for MRI-Guided Percutaneous Interventions

Chapter 3 presents an automatic real-time needle tracking technique using a deep learning method. Mask region-based convolution neural networks (Mask R-CNN) is a fast and accurate method for instance-level object detection and segmentation in natural images. This study adapted and trained Mask R-CNN for needle feature detection and segmentation on intra-procedural prostate MRI and *ex vivo* tissue real-time MRI including variations of needle signal void feature with different background tissue features, different MRI sequence types and parameters, needle materials, and the needle's orientation relative to the $B_0$ direction. In addition, a postprocessing needle feature localization algorithm was developed to directly use the segmentation mask from the Mask R-CNN model output without time-consuming ensemble methods to extract the needle feature tip location and axis orientation with real-time processing time.

### 1.6.3 Aim 3: Physics-Driven Mask R-CNN for Physical Needle Localization in MRI-Guided Percutaneous Interventions

Chapter 4 presents a physics-driven Mask R-CNN model to overcome the discrepancies between the needle feature on MRI and the underlying physical needle position. Physics-based simulated needle features that achieved a close agreement with actual MRI scans of the physical needle were generated to form a sufficiently large training dataset. First, this work proposed a single-slice physical needle Mask R-CNN model, in which the imaging plane is perfectly aligned with the needle. This model was combined with the needle feature Mask R-CNN in Chapter 3 to form a two-stage automatic physical needle localization framework that overcomes in-plane discrepancies between needle feature and physical needle. Furthermore, this work proposed a 3-slice physical needle Mask R-CNN to estimate the overall 3D physical needle position by directly estimating through-plane physical needle position in situations where the imaging plane is not perfectly aligned with the needle. Both models can directly estimate the physical needle position based on passive needle feature on MRI within real-time processing time.

# Chapter 2 Respiratory Motion Prediction Using Fusion-Based Multi-Rate Kalman Filtering and Real-Time Golden-Angle Radial MRI

## 2.1 Introduction

Magnetic resonance imaging (MRI) is a promising modality for intra-procedural and real-time guidance of minimally invasive interventions, due to its excellent soft tissue contrast and absence of ionizing radiation[14,34,60,61]. However, MRI-guided interventions still face multiple challenges, including limited access to patients inside the scanner, tissue displacement due to motion, user interface design for interactive real-time imaging, and workflow optimization. Remotely controlled systems for manipulating instruments inside the MRI scanner, such as MR-compatible needle actuators, are being developed to address the challenge of patient access[32,62-66]. To address the challenge of tissue motion, computer-assisted navigation methods can provide key information regarding instrument and tissue positions for MRI-guided percutaneous needle biopsy[67,68], thermal ablation[69,70], and radiotherapy[71-74]. However, respiratory motion still remains a main challenge, especially for procedures in abdominal organs[39]. The effectiveness of computer-assisted navigation is highly dependent on the accuracy of tissue target motion tracking. In this study, we will focus on addressing the challenge of respiratory motion.

Image-based and surrogate-based tracking are two main categories of methods to obtain spatial coordinates of target features from real-time MR imaging. The upper bound of the tracking performance is limited by the MRI spatial resolution. The desired tracking accuracy depends on the application. A representative scenario would be image-guided cancer biopsy or ablation, where clinicians may target tumors with a diameter of 5 mm[56], hence tracking error should be 2.5 mm or less. Image-based tracking methods can generate accurate spatial coordinates of the feature motion provided the images have sufficient geometric accuracy. Shi and Bjerre[75,76] illustrated a general strategy of applying the intensity-based raw feature matching algorithm for both 2D and 3D motion tracking. The initial implementation was computationally intensive (150 ms) but was further improved with enhanced computing power. Bourque[77] applied a particle filter to track the tumor contour with a processing time of around 20 ms. The Scale Invariant Feature Transform (SIFT) extracts internal features from MR images and localizes the features using template matching[47,49,50], but it requires additional acceleration using graphics processing units (GPU) to achieve real-time processing[78]. Optical flow algorithms provide pixel-level tracking, which have been applied to target monitoring and motion correction for MR thermometry[69,70,79]. The error of these types of image-based tracking methods is around the dimensions of a single pixel and specific target features can be directly selected and tracked. However, the processing time for MR image reconstruction and motion processing introduces latencies that degrade the accuracy of the motion feedback information.

Surrogate-based tracking methods take advantage of the relationship between more complex feature motion and rapid low-dimensional online surrogate measurements. Incoming surrogate signals are used as an input to a motion model to estimate the motion of specific features. Paganelli[49] used abdominal surface markers as the surrogate and tumor motion was estimated using a state-augmented quadratic model based on their correlation. This tracking method introduced additional tracking error on the scale of one pixel. Seregni[47] utilized the correlation model but acquired external abdominal motion measurements using the respiratory bellows of Siemens' Physiological Measurement Unit (PMU) and Varian's Real-Time Position Management (RPM) system. In general, surrogate-based tracking has less latency but requires a training phase and may introduce additional motion tracking errors due to model inconsistency.

The reported latency for intra-fraction motion management (i.e., gating) on the most recent MRI-guided radiotherapy systems ranges from 250 ms to 550 ms[72,80-82]. The latency varies depending on different techniques and different applications, which are active topics for research. An effective approach to overcome the tracking latency is to establish a temporal model of respiratory motion using prior knowledge of the motion characteristics[47,48,51]. For example, conventional Kalman filtering is robust to measurement noise and can be used to perform systematic estimation for respiratory motion prediction[83,84]. However, these prediction methods are still challenged by the irregularity and the quasi-periodicity of respiratory motion[77]. Since image-based and surrogate-based methods have respective advantages of higher tracking accuracy (lower error) and lower system latency, motion prediction can potentially be improved by formulating a sensor fusion problem where both methods are performed simultaneously and then combined[83,85]. Alexander[86] proposed a multi-rate fusion method to correct the state estimation errors by incorporating an updated Kalman gain and covariance based on delayed measurements. Larsen[87] introduced a parallel filter scheme to process sensor data simultaneously using Kalman filtering.

In this study, we propose a fusion-based framework that combines image-based tracking results as a delayed measurement with rapid surrogate-based tracking results in a multi-rate Kalman filter to achieve accurate (low error) motion prediction. In real-time MRI-guided interventions, simultaneous image-based and surrogate-based motion tracking can be accomplished by using flexible data acquisition strategies. In particular, this could be achieved by leveraging a unique golden-angle (GA) ordered radial acquisition scheme to simultaneously reconstruct images and extract surrogate signals from the same data stream[36]. GA radial acquisition samples a new readout (radial spoke) each repetition time (TR) by continually rotating the readouts by a golden-ratio angle of 111.25°, which provides almost equally spaced sampling in k- space over time. The same data stream can be flexibly reconstructed using sliding-window methods with different combinations of temporal footprints and temporal resolutions[37]. By sampling the center of k-space redundantly, GA radial MRI also has higher robustness to physiological motion and undersampling[35-37].Therefore, this scheme can potentially reduce system latency, improve tracking accuracy, and lead to more accurate motion prediction.

The aim of this study is two-fold. First, we evaluate the characteristics of online image-based and surrogate-based motion tracking using real-time GA radial MRI acquisition. The characterization results from a programmable MRI motion phantom are used as a reference to design and compare different motion prediction methods. Second, we propose and evaluate a new fusion-based motion prediction framework that integrates simultaneously acquired image-based and surrogate-based tracking results from GA radial MRI into a multi-rate Kalman filter. The prediction accuracy is evaluated in real-time free-breathing liver MRI datasets and compared with image-based and surrogate-based methods.

## 2.2 Methods

### 2.2.1 Motion Prediction Framework using Real-Time GA Radial MRI

We propose a motion prediction framework using real-time GA radial MRI, which combines image-based and surrogate-based tracking as fused measurements in a multi-rate Kalman filter (**Figure 2-1**). Parameters for the Kalman filter (F, H, Q, R) are determined using expectation maximization (EM) training[88]. The proposed framework overcomes system latency by using the Kalman filter to predict the motion at a future time relative to the measurement time.

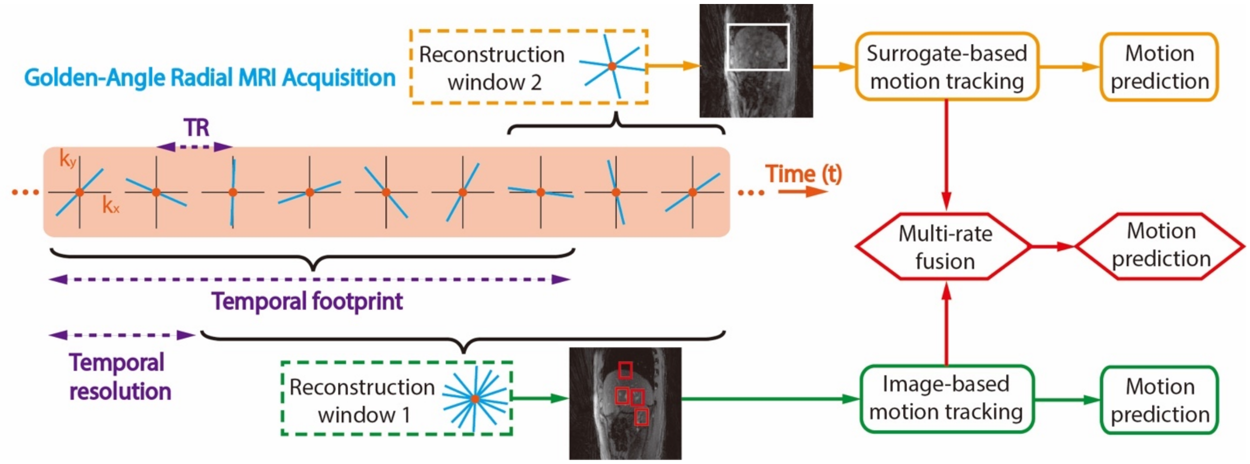

**Figure 2-1 Proposed motion prediction framework using golden-angle-ordered radial MRI. Radial MRI readouts (spokes) were acquired in the $k_x$-$k_y$ plane every repetition time (TR) and continually rotated by the golden angle. The same stream of golden-angle radial MRI data was reconstructed using sliding windows with different temporal footprints (e.g., reconstruction windows 1 and 2). The time difference between two adjacent reconstruction windows was defined as the temporal resolution. Motion prediction was performed using image-based and surrogate-based methods, or by using the proposed multi-rate fusion-based method to combine the respective advantages of image-based and surrogate-based approaches.**

(1) Image-Based Tracking: Images with higher signal-to-noise ratio (SNR) and image quality were reconstructed with a wider temporal footprint (e.g., reconstruction window 1 in **Figure 2-1**). The target feature motion was extracted directly from the images, but the motion feedback may be inaccurate because of the system latency $d\tau_1$ (**Figure 2-2a**). A template-matching algorithm was used to extract the 2D translational motion of the target features[89,90] (**Figure 2-2c**). A two-scale multi-resolution pyramid method was applied in the template-matching algorithm to interpolate the images by 4-fold using k-space zero-filling[91-93]. The two-scale approach improved the computational efficiency of the algorithm and the interpolation increased the sensitivity of motion tracking to sub-pixel.

(2) Surrogate-Based Tracking: At the same time, images with lower SNR and image quality were reconstructed with a narrower temporal footprint (e.g., reconstruction window 2 in **Figure 2-1**). The overall organ motion (e.g., liver) was extracted as a surrogate signal for tissue features

inside the organ and input to a pre-trained motion model to estimate target feature motion (**Figure 2-3a**). The motion model parameters were determined using training data, where GA radial readouts were retrospectively allocated into both the narrower reconstruction window for surrogate-based tracking and the wider reconstruction window for image-based tracking, with the centers of their temporal footprints aligned (**Figure 2-3b**). A quadratic motion model (Φ) was constructed based on the correlation between superior-inferior (SI) motion (y) of the target feature from the image-based tracking results and the surrogate (s) signals:

**Equation 2-1**

$$y_{SI} = \phi(s) = as^2 + bs + c + d\dot{s} + e\dot{s}^2$$

The surrogate result was noisy because of the lower SNR and increased streaking artifacts in the narrow temporal footprint images. To improve the consistency of the model, a denoising Kalman filter was applied to the surrogate signals.

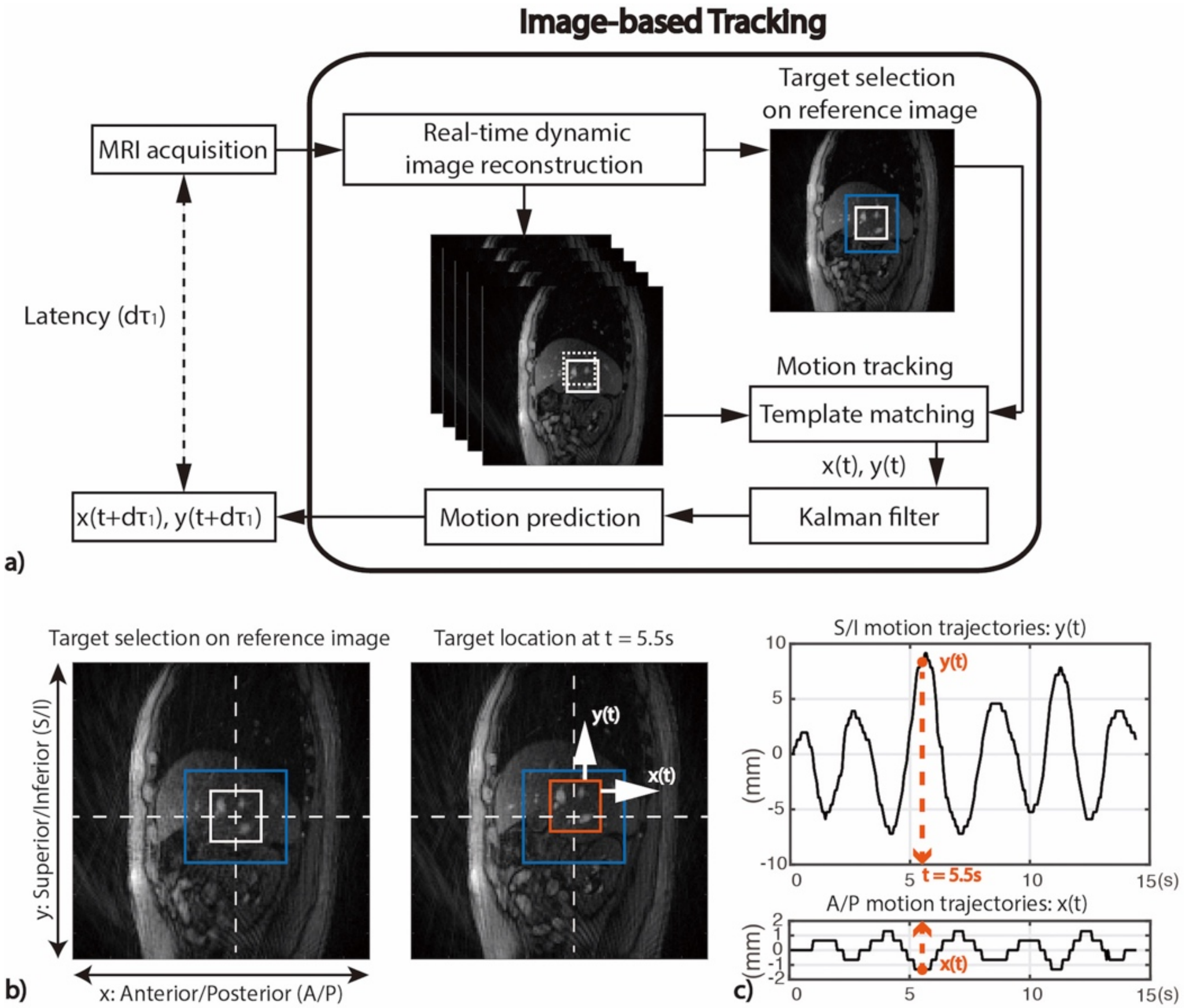

**Figure 2-2 (a) Motion prediction with image-based tracking using images reconstructed with a wide temporal footprint (e.g., reconstruction window 1 in Figure 2-1). (b) Reference features of the target tissue were identified by the user based on a reference anatomical image (white box) and the expected maximum range of motion was specified by the user (blue box). (c) Example superior/inferior (S/I) and anterior/posterior (A/P) image-based motion tracking results for the features in (b).**

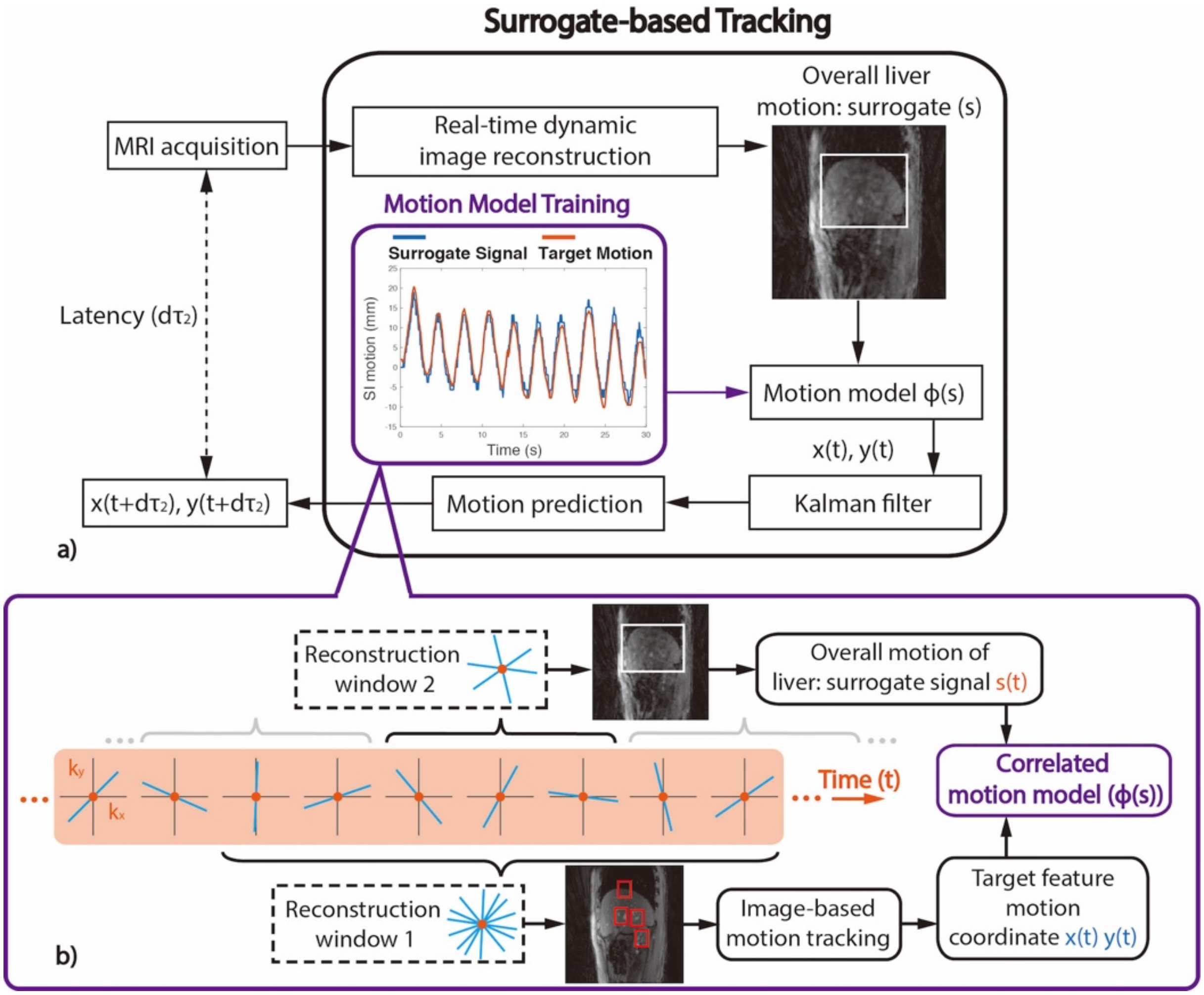

**Figure 2-3 (a) Motion prediction with surrogate-based tracking using images reconstructed with a narrow temporal footprint (e.g., reconstruction window 2 in Figure 2-1). The overall motion of the liver was tracked to provide a surrogate signal for tissue features inside the liver. (b) The motion model parameters were determined using training data, where the surrogate signal and target feature motion (measured by image-based tracking) were retrospectively obtained at the same time points by aligning the centers of reconstruction windows 2 and 1, respectively.**

*(3) Multi-Rate Fusion-Based Method:* To overcome system latency, the Kalman filter (see **Appendix**) was used to predict the motion state at a future time relative to the measurement time. Furthermore, the primary (surrogate-based) and delayed (image-based) tracking results were fused together in a multi-rate Kalman filter[85]. **Figure 2-4** illustrates the fusion-based method fusing the delayed measurement, where *z* denotes the motion tracking measurements. The surrogate-based tracking result was designated as the primary Kalman filter (PKF) agent, since it had lower latency

($d\tau_2$) for motion feedback due to its narrow temporal footprint. The state variables of the motion state estimated in the PKF agent are denoted as $x_P$ and $y_P$ in the state space model; $t_P$ denotes the discretized time step:

**Equation 2-2**

$$x_P(t_P) = F_P x_P(t_P - 1) + w_P(t_P) \sim \mathcal{N}(0, Q_P(t_P))$$

**Equation 2-3**

$$y_P(t_P) = H x_P(t_P) + v_P(t_P) \sim \mathcal{N}(0, R_P(t_P))$$

The initial filtered result might be suboptimal, because of increased noise in the surrogate-based tracking result due to model inconsistency:

**Equation 2-4**

$$\bar{x}_P(t_P|t_P) = \bar{x}_P(t_P|t_P - 1) + K_P(t_P)(z(t_P) - H\bar{x}_P(t_P|t_P - 1))$$

Alexander[86] and Larsen[87] proposed a one-step correction to optimize the filtered result by fusing the delayed measurement. This multi-rate fusion method decreases the state covariance so that the accuracy of the filtered surrogate-based tracking result can be improved by incorporating the image-based tracking result. The image-based tracking result was designated as the delayed KF (DKF) agent, since it has a higher latency ($d\tau_1$) for motion feedback due to its wider temporal footprint. The state variable of the motion state estimated in the DKF agent was denoted as $x_D$ and $t_D$ denotes the discretized time step in the DKF agent:

**Equation 2-5**

$$x_D(t_D) = F_D x_D(t_D - 1) + w_D(t_D) \sim \mathcal{N}(0, Q_D(t_D))$$

**Equation 2-6**

$$y(t_D) = H x(t_D) + v_D(t_D) \sim \mathcal{N}(0,\ R_D(t_D))$$

The filtered surrogate-based tracking result was corrected by an additional term based on the measurement and processing result in the DKF agent, where *N* denotes the number of time steps covering the time delay, based on the number of steps between the primary and delayed measurements. The corrected filtered result was denoted as $\bar{x}_{P+D}$:

**Equation 2-7**

$$\bar{x}_{P+D}(t_P|t_P) = \bar{x}_P(t_P|t_P) + M_{D\rightarrow P}K_D(z(t_D) - H\bar{x}_D(t_D|t_D - 1))$$

**Equation 2-8**

$$M_{D\rightarrow P} = \prod_{i=0}^{N-1}(I - K_{P-i}H)\,F_D, \quad N = t_P - t_D$$

In the computation of *M*, if the delayed time gap contains more than a single time step, intermediate tracking results are required for the multiplication steps. Either type of tracking can be used in the intermediate step if it is available in real time. The state space model parameters (*F, H, Q, R*) can be obtained based on maximum likelihood estimation of the system. The estimation problem is solved using previously acquired training motion data and the expectation maximization (EM) algorithm[88]. The model parameter selection for delayed and primary KF agents are trained separately.

*(4) Kalman Filter-Based Motion Prediction:* We overcome system latency dτ defined as the number of additional time steps beyond the current time (denoted as *t*) by using the Kalman filter (see **Appendix**) to calculate the expected motion state for a future time point *t* + dτ:

**Equation 2-9**

$$\bar{y}(t + d\tau|t) = HF^{d\tau}\bar{x}(t|t), \ \ \mathrm{d}\tau = \frac{latency}{temporal\ resolution}$$

The selection of the process state transition function *F* is essential to ensuring the performance of the prediction. In this study, we set the initial value of *F* as the first order linear approximation of the sinusoidal model proposed by Spincemaille[84]. Since respiratory motion may not be perfectly periodic, an adaptive adjustment of the model can improve the ability to predict future motion states. To this end, we used the EM algorithm on training data to determine $F$ and apply this for Kalman filter-based motion prediction.

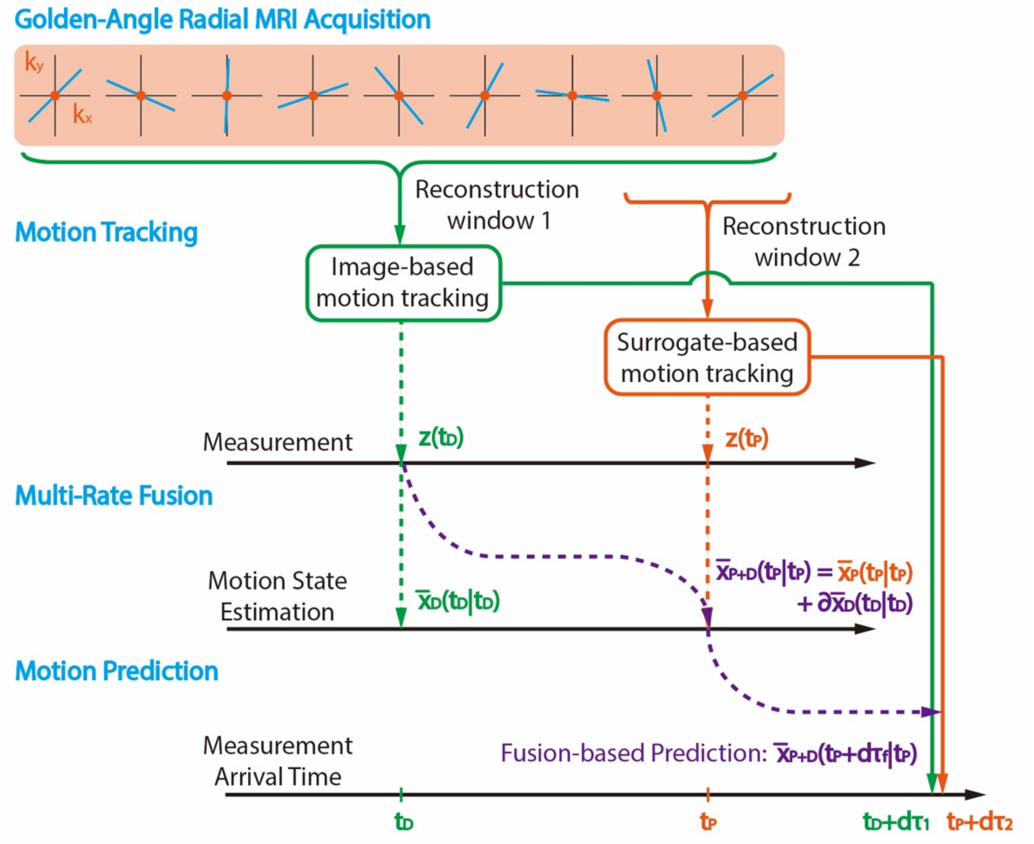

**Figure 2-4 The proposed multi-rate motion prediction method fuses the delayed measurements from image-based motion tracking with surrogate-based motion tracking results to achieve high spatial accuracy and low latency. The system latency of the multi-rate fusion-based method ($d\tau_f$) is determined based on system latencies of both the image-based and surrogate-based methods.**

### 2.2.2 Real-Time MRI Software Pipeline and Online Tracking Experiments

The proposed framework (section A) was established in a real-time software pipeline (**Figure 2-5**) on a 3 T MRI scanner (Prisma, Siemens Healthineers, Erlangen, Germany). Online tracking error and system latency for both image-based and surrogate-based tracking methods were evaluated with a programmable MRI-compatible motion phantom[94].

*(1) Real-Time GA Radial MRI Software Pipeline:* Real-time MRI data acquired using the

golden-angle (GA) radial trajectory were reconstructed online using an open source software package (Gadgetron[38]). The reconstruction server continuously accepted imaging data during scanning. Data buffers were used to accumulate data for different reconstruction windows (i.e., temporal footprint of images) and dynamically updated for sliding-window reconstruction. A graphics processing unit (GPU)-accelerated *k*-space gridding technique and iterative non-Cartesian sensitivity encoding (SENSE) algorithm were implemented on to reconstruct images from radial MRI data[38,95]. Imaging and reconstruction parameters for two different reconstruction windows (**Figure 2-1**) are presented in **Table 2-1**. The radial *k*-space trajectory was corrected by using a bulk gradient delay during sequence calibration. Geometric distortion due to gradient non-linear effects were corrected using a vendor provided method. The reconstructed images were transmitted to an external image processing program, where different motion tracking methods were applied based on the temporal footprint of the image received.

**Table 2-1 Image acquisition parameters for the real-time golden-angle-ordered radial spoiled gradient echo MRI Sequence at 3T and Parameters of radial MRI sliding-window dynamic reconstruction using non-Cartesian SENSE**

<table>
<tr><th colspan="4">Image Acquisition Parameters</th></tr>
<tr><td>TR</td><td>6.3 ms</td><td>TE</td><td>2.49 ms</td></tr>
<tr><td>FOV</td><td>300 x 300 mm²</td><td>Spatial Resolution</td><td>1.56 x 1.56 mm²</td></tr>
<tr><td>Flip Angle</td><td>12°</td><td>Slice Thickness</td><td>5 mm</td></tr>
<tr><td>Matrix Size</td><td>192 x 192</td><td>Readout Bandwidth</td><td>400 Hz/pixel</td></tr>
<tr><th colspan="4"><b>Dynamic Reconstruction Parameters</b> - Image-based motion tracking</th></tr>
<tr><td colspan="2">Temporal Footprint</td><td colspan="2">440 ms (70 spokes)</td></tr>
<tr><td colspan="2">Temporal Resolution</td><td colspan="2">100 ms (16 spokes)</td></tr>
<tr><th colspan="4"><b>Dynamic Reconstruction Parameters</b> – Surrogate-based motion tracking</th></tr>
<tr><td colspan="2">Temporal Footprint</td><td colspan="2">100 ms (16 spokes)</td></tr>
<tr><td colspan="2">Temporal Resolution</td><td colspan="2">100 ms (16 spokes)</td></tr>
<tr><th colspan="4">Non-Cartesian SENSE Parameters</th></tr>
<tr><td>Convolution Kernel Size</td><td>5.5</td><td>Convolution Oversampling</td><td>1.25</td></tr>
<tr><td>Reconstruction Time (ms)</td><td>60-80</td><td>Iterations</td><td>3</td></tr>
<tr><td>Regularization Weights</td><td>0.3</td><td>Calibration Frame</td><td>30</td></tr>
</table>

*(2) System Latency Measurement:* In our implementation, the real-time MRI acquisition and reconstruction modules and the motion tracking modules ran on separate workstations. To calibrate the time delay (latency) from image acquisition to motion tracking in this pipeline, a trigger signal converter (Siemens Healthineers, Erlangen, Germany) was added (**Figure 2-5**). The radial MRI sequence was programmed to periodically transmit a control signal through the trigger converter. The imaging time at the center of the acquisition window was recorded as the ground

truth timestamp. The timestamp for the final motion tracking result, which experienced time delays in the software pipeline, was also extracted. Therefore, the system latency for every individual tracking result can be measured as the difference between the ground truth timestamp and the timestamp of the delayed motion tracking result.

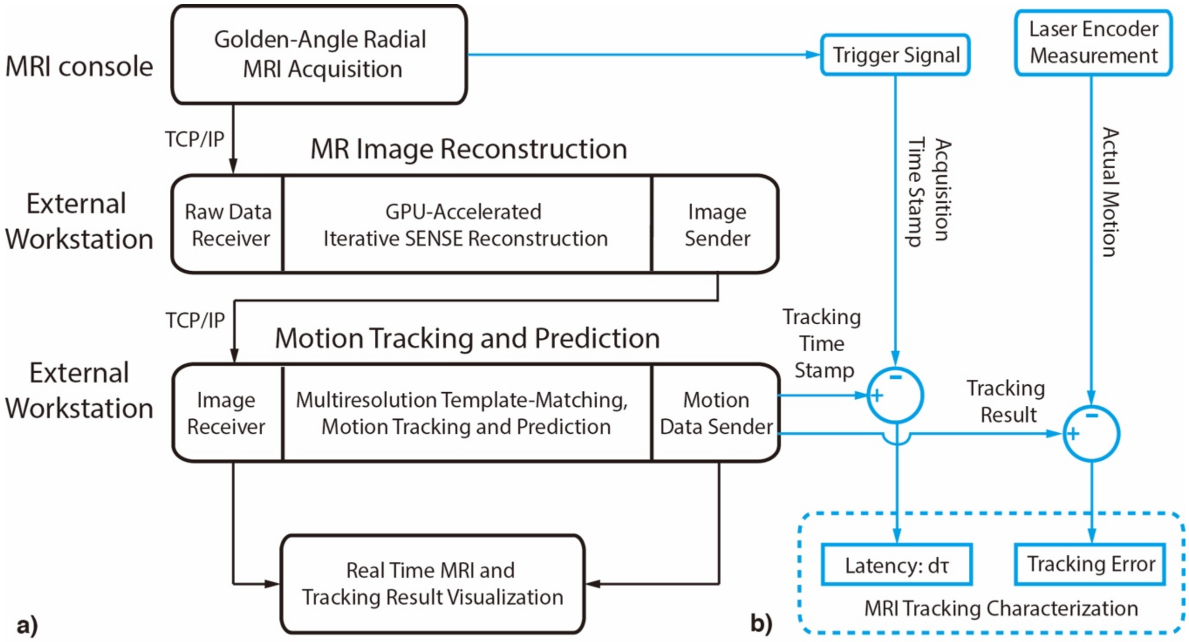

**Figure 2-5 (a) The online real-time MRI motion tracking pipeline was implemented using custom software modules for real-time image reconstruction, motion tracking and prediction, and visualization. GPU: graphics processing unit. SENSE: sensitivity encoding. (b) System latency for the online tracking pipeline was calibrated using a trigger signal from the acquisition sequence and comparing time stamps. MRI-based tracking error was calibrated against laser encoder measurements of a programmable MRI-compatible motion phantom.**

*(3) Motion Tracking Accuracy Assessment:* To calibrate the tracking accuracy of the software pipeline, we imaged a motion phantom with programmable motion. A gel-filled acrylic phantom with an array of 10-mm circular features (**Figure 2-6**) was secured on an MR-compatible hydrostatically-actuated motion platform, which had high reproducibility for motion waveforms (root mean squared error [RMSE] = 0.198 mm)[94]. Two respiratory motion waveforms pre-recorded from free-breathing human subject liver MRI scans with a 25-mm peak-to-peak range of motion were programmed into the computer-controlled motor and learned by the platform to emulate a

free-breathing subject with target features for interventional procedures. The phantom motion direction was along the main magnetic field of the scanner, which was the superior-inferior (SI) direction in the patient's coordinate system. To obtain the actual motion of the phantom, a retro-reflector was attached on the platform and a laser encoder was used to measure the displacement on a lab bench with a precision of 0.635 μm. The results were used to evaluate MRI motion tracking results.

### 2.2.3 Evaluation of Proposed Framework for Motion Prediction

Due to limitations in the software libraries[38] currently used for online implementation (2.1.2), the surrogate-based and image-based methods could be performed individually but not at the same time for online fusion-based prediction. To evaluate the proposed motion prediction framework, a retrospective study that closely emulated actual online operation was conducted where the image-based, surrogate-based and fusion-based tracking methods were all applied to *in vivo* real-time free-breathing liver GA radial MRI datasets and compared.

*(1) In vivo Liver MRI Datasets*: In an Institutional Review Board (IRB)-approved and Health Insurance Portability and Accountability Act (HIPPA)-compliant study, real-time 2D sagittal liver GA radial MRI scans were acquired in 8 healthy subjects (6 male, 2 female; 29±4.1 years of age) on another 3 T MRI scanner (same model: Prisma, Siemens Healthineers, Erlangen, Germany) with body and spine array receiver coils. Images were acquired using a radiofrequency (RF)-spoiled gradient echo (GRE) GA radial sequence during normal, deep, and shallow breathing under instruction for each subject and retrospectively reconstructed. On each series of real-time images, two to four different regions in the liver were selected as target features to be tracked, resulting in a total of 75 motion waveforms (33 normal, 16 deep, and 26 shallow breathing) for motion prediction. The same imaging and reconstruction parameters from the online

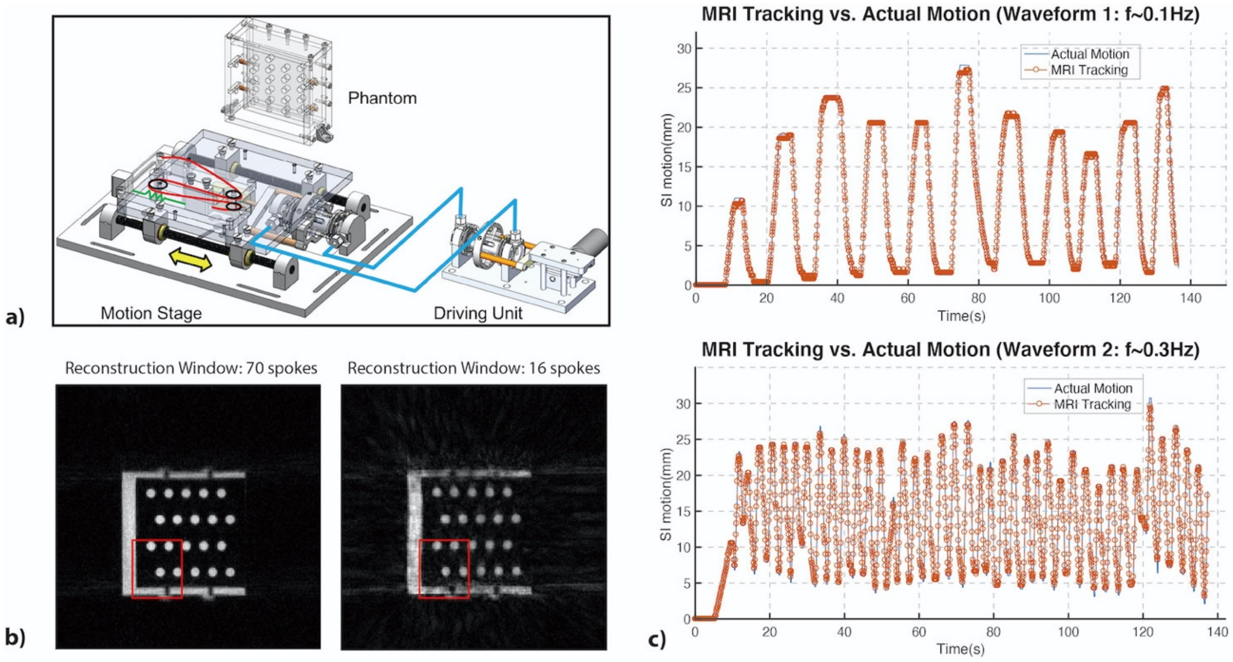

**Figure 2-6 (a) Design diagram of the MR compatible motion phantom. (b) Golden-angle-ordered radial MR images of the motion phantom reconstructed by the real-time pipeline with different reconstruction windows (i.e., temporal footprints). Online motion tracking was performed for the selected target region (red box) in the motion phantom. (c) Real-time MR image-based motion tracking achieves close agreement with actual motion measured by laser encoders for the motion phantom programmed with 2 pre-recorded respiratory motion waveforms (~0.1 Hz and ~0.3 Hz).**

real-time MRI experiments (**Table 2-1**) were used here. The online latency calibration method (**2.2.2**) was also applied on this scanner in one subject scan and the measured latencies were used to evaluate motion prediction.

*(2) Motion Prediction Evaluation:* In the retrospective studies, motion tracking and prediction were performed offline using MATLAB. The real-time MRI data was used to emulate an online input data stream for the motion prediction methods. The EM algorithm used 30 secs of training data right before the 60-sec section of testing data to estimate the state space model parameters for Kalman filtering. We used the actual measured latencies of both image-based and surrogate-based tracking from one subject scan to evaluate the motion prediction methods. The latencies varied over a small range throughout the scan due to variations in reconstruction time. The latencies for the multi-rate fusion-based method were determined by whenever processing

finished for both tracking methods in each time frame. This emulation of latencies recreates realistic online conditions for retrospective evaluation. The same imaging parameters from the online experiments were applied here. For the multi-rate KF algorithm (**Equation 2-7**), $N$ equals 2 and only one intermediate measurement (from surrogate-based tracking) was used in the fusion algorithm. Image-based tracking results from the retrospectively sampled image frames centered at each time point were used as the reference ($y_R$) to evaluate the motion prediction results. The reference was interpolated to extract values corresponding to the emulated latencies.

We compared the motion prediction results using the new fusion-based method versus the image-based and surrogate-based methods. The prediction error (mm) was defined as the absolute difference between the motion prediction result and the reference ($y_R$) during 60 secs of motion. RMSE and the percentage of prediction error greater than 2.5 mm ($\varepsilon_{2.5}$, %) were calculated for every waveform. The threshold of 2.5 mm was selected since physicians may target lesions with diameter ≥5 mm during interventions[55]. These two different error metrics assess the prediction performance in separate aspects. RMSE measures the average prediction accuracy, while $\varepsilon_{2.5}$ evaluates the ability to remove outliers. The difference in RMSE and $\varepsilon_{2.5}$ achieved by different prediction methods were evaluated using non-parametric statistical tests (two-sided Wilcox signed rank test) with $p < 0.05$ considered significant. The comparisons were performed for all respiratory motion waveforms and for sub-categories based on the type of breathing motion (normal, deep, shallow).

## 2.3 Results

### 2.3.1 Online Tracking Accuracy and System Latency

Example images for image-based motion tracking and surrogate-based motion tracking are shown in **Figure 2-6**. A reference template image and tracking region were selected before the motion started. Actual motion measured by laser encoders and results from online motion tracking with MRI were retrospectively aligned. Example image-based tracking results are shown in **Figure 2-6**. The error for image-based tracking (waveform 1: 0.3±0.2 mm, waveform 2: 0.3±0.3 mm) was significantly lower ($p < 0.05$) than surrogate-based tracking (waveform 1: 0.5±0.6 mm, waveform 2: 0.6±0.6 mm) for both waveforms. In this phantom, which had rigid body motion, both image-based and surrogate-based tracking had sub-pixel accuracy for features of interest. The system latency measured for online image-based tracking (waveform 1: 360±50 ms, waveform 2: 350±50 ms) was significantly higher ($p < 0.0001$) than surrogate-based tracking (waveform 1: 140±30 ms, waveform 2: 160±50 ms) in both waveforms. These results demonstrate the respective advantages of image-based tracking (higher spatial accuracy, i.e., lower error) and surrogate-based tracking (lower latency) using images acquired from golden-angle radial MRI. The image-based tracking results demonstrated sufficient accuracy for rigid-body translational motion. Therefore, we used retrospective image-based tracking as the reference to evaluate the prediction of translational motion of tissue regions of interest in the *in vivo* studies.

### 2.3.2 Motion Prediction Evaluation in Retrospective Studies

The latencies measured from the subject scan were 320ms±20ms for image-based tracking and 150ms±22ms for surrogate-based tracking; this resulted in latencies of 160±23ms for the fusion-based method. The image-based and surrogate-based tracking latencies were similar to the calibration results using the motion phantom, demonstrating the robustness of the software pipeline for different scanners. These measured latencies were used to evaluate the motion prediction methods. In **Figure 2-7**, examples of fusion-based motion prediction are shown for 60 secs from normal and shallow breathing waveforms. Compared with prediction results based on either image-based or surrogate-based tracking, the fusion-based results showed closer agreement with the reference waveform. The prediction results for all the breathing waveforms and three types of waveforms are summarized in **Figure 2-8**. Using the proposed fusion-based multi-rate method, the median RMSE of the prediction error was reduced from 1.18 mm and 1.3 mm to 0.97 mm and the median $\varepsilon_{2.5}$ was reduced from 3.5% and 6.2% to 2.5%, compared to the prediction error for surrogate-based and image-based methods for all 75 waveforms ($p = 1.61\times10^{-8}$ for RMSE and $p=1.53\times10^{-6}$ for $\varepsilon_{2.5}$ between the fusion-based multi-rate and surrogate-based methods; $p =1.34\times10^{-9}$ for RMSE and $p = 5.24\times10^{-10}$ for $\varepsilon_{2.5}$ between the fusion-based multi-rate and image-based methods). In addition, the interquartile range (IQR) of $\varepsilon_{2.5}$ was reduced from 8.5% for surrogate-based and 14.4% for image-based to 5.5% for fusion-based prediction. No significant differences were found between the motion prediction results for the surrogate-based and image-based methods based on RMSE ($p = 0.079$). Prediction results were slightly more accurate for the surrogate-based method than the image-based method based on $\varepsilon_{2.5}$ ($p = 0.012$).

For the three types of breathing waveforms, fusion-based prediction RMSE and $\varepsilon_{2.5}$ were significantly lower than the prediction results based on surrogate-based and image-based tracking ($p <0.05$). Meanwhile, there were no significant differences between the prediction results from the surrogate-based and image-based methods in any sub-categories of the waveforms based on RMSE. The surrogate-based method was slightly more accurate than the image-based method based on $\varepsilon_{2.5}$ for normal breathing waveforms. Results from the 16 deep-breathing waveforms showed noteworthy improvement for the fusion-based method compared with the surrogate-based method, where the median RMSE of the prediction error was reduced from 1.4 mm to 1.17 mm, the median $\varepsilon_{2.5}$ was reduced from 5.4% to 3.4%, and the IQR of $\varepsilon_{2.5}$ was reduced from 17.5% to 4.1%. Results from the 33 normal-breathing waveforms showed notable improvement for the fusion-based method compared with the image-based method, where the median RMSE of prediction error was reduced from 1.29 mm to 0.97 mm, the median $\varepsilon_{2.5}$ was reduced from 5.5% to 2.2%, and the IQR of $\varepsilon_{2.5}$ was reduced from 11.8% to 3.4%.

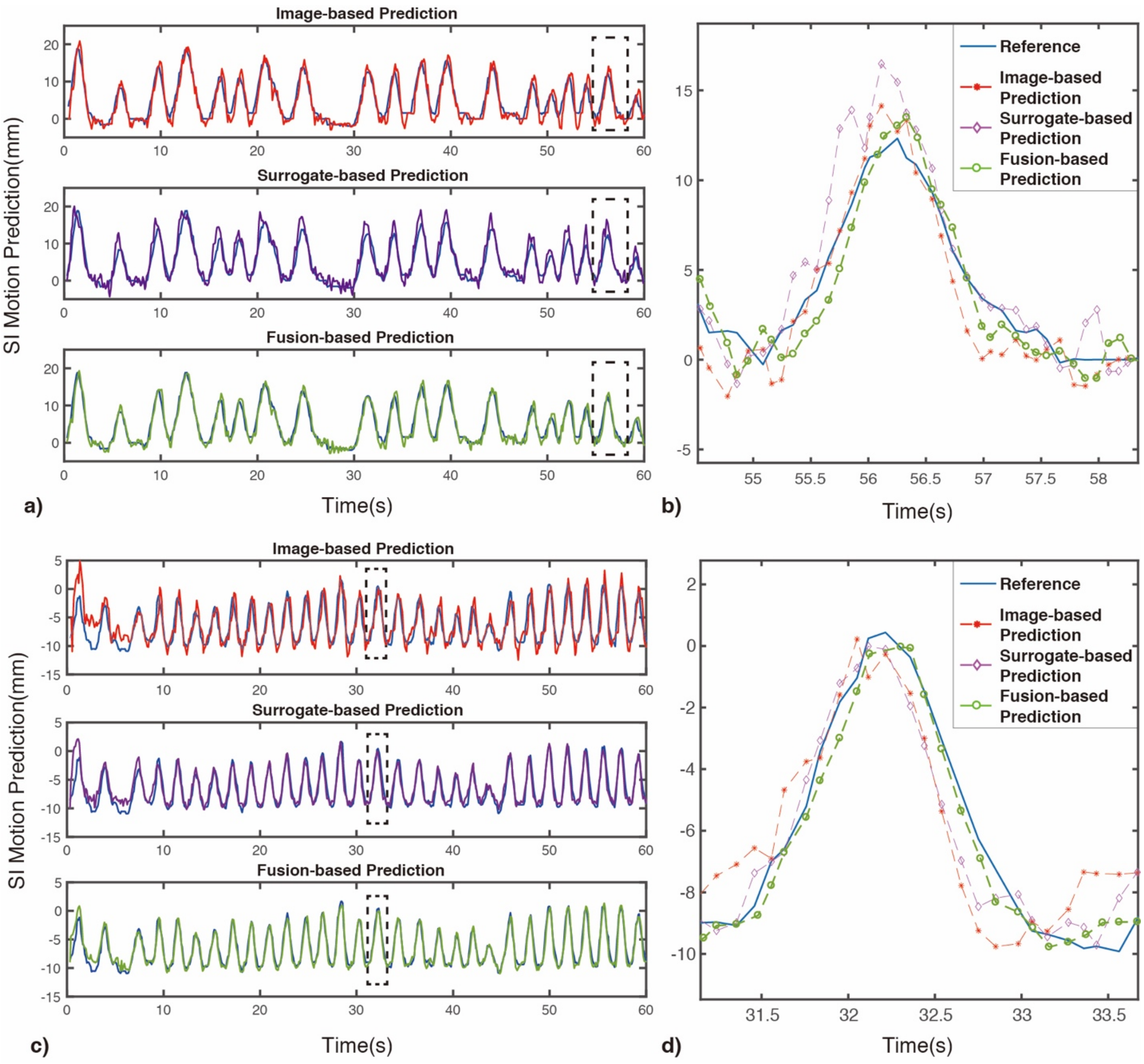

**Figure 2-7 Example motion prediction results using image-based, surrogate-based, and fusion-based methods compared to reference results obtained from retrospective image-based tracking. (a, b) A normal breathing waveform containing some irregular patterns and (c, d) a shallow breathing waveform. (b, d) Zoomed-in views of a single period of the waveforms (corresponding to dashed boxes in a and c, respectively) illustrate the improvement using fusion-based compared to image-based and surrogate-based prediction. SI: superior/inferior.**

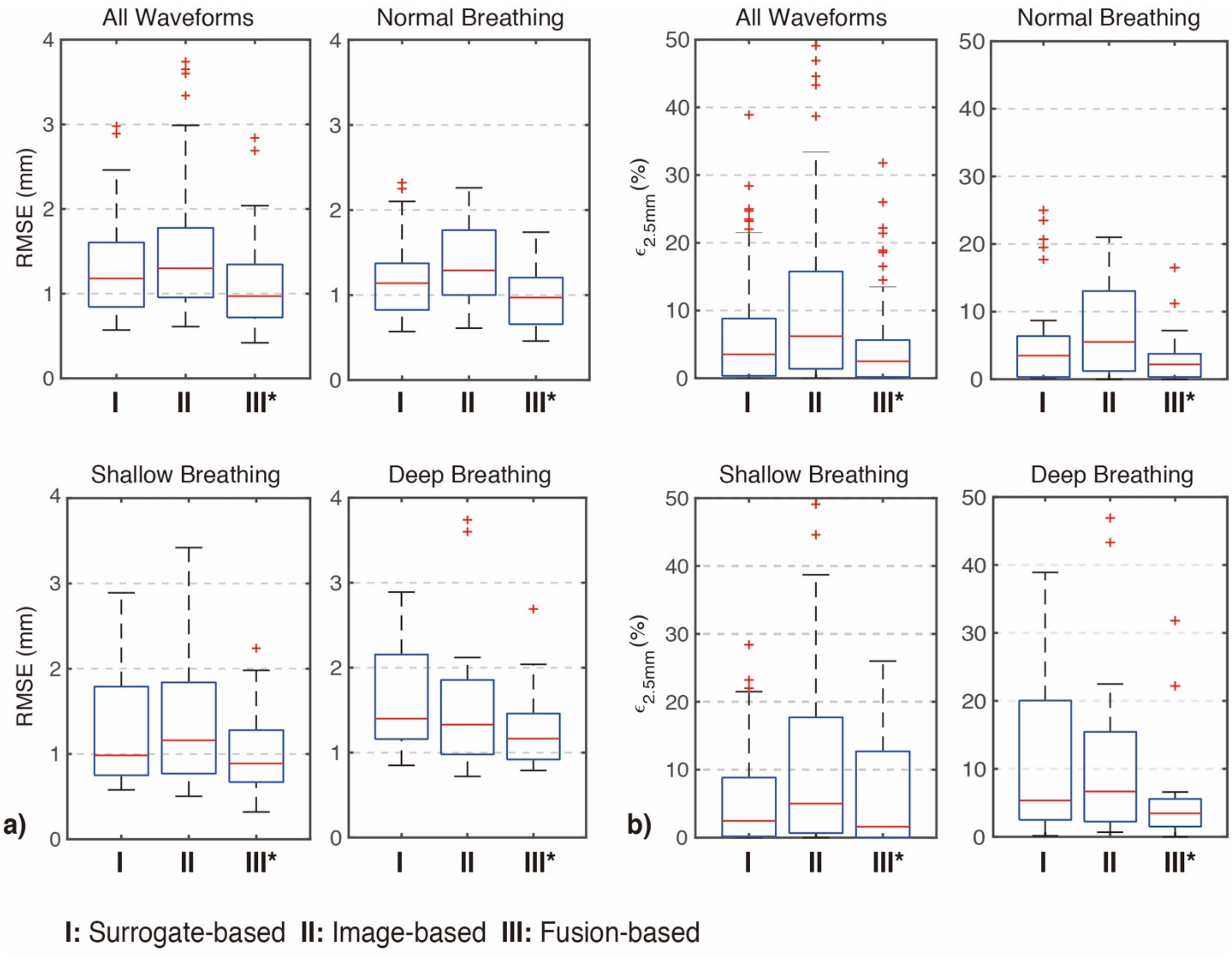

**Figure 2-8 (a) Comparison of respiratory motion prediction root mean squared error (RMSE) using different methods for 75 respiratory waveforms, including three different types of breathing (shallow breathing: 26 waveforms, deep breathing: 16 waveforms, normal breathing: 33 waveforms). (b) Comparison of respiratory motion prediction $\varepsilon_{2.5mm}$ (% of data with RMSE >2.5 mm) using different prediction methods for all of the waveforms and three different types of breathing. In all cases, the fusion-based method achieved significantly lower prediction RMSE and $\varepsilon_{2.5mm}$ compared to image-based and surrogate-based methods. The black dashed bars indicate maximum-minimum range, the blue boxes indicate 25th and 75th percentile range, the red lines indicate median value, and the red crosses indicate outliers. * indicates Wilcoxon signed rank test with $p < 0.05$ for fusion-based versus surrogate-based and fusion-based versus image-based prediction.**

## 2.4 Discussion

In this study, we characterized image-based and surrogate-based motion tracking performance in an online software pipeline using real-time GA radial MRI. In addition, we proposed and evaluated a new fusion-based respiratory motion prediction framework using multi-rate Kalman filtering and real-time GA radial MRI. We demonstrated that the prediction error of the new fusion-based framework is significantly reduced compared to image-based or surrogate-based methods in a set of *in vivo* respiratory waveforms.

RF-spoiled GRE and balanced steady-state free precession (bSSFP) are commonly used sequences for real-time MRI[34,96-98]. bSSFP enables short TR, high SNR, and good contrast with $T_2/T_1$ weighting. However, bSSFP has increased banding artifacts at 3 T compared to 1.5 T due to the greater B0 inhomogeneity, especially in the liver and abdomen. The bSSFP banding artifacts may impede visualization of devices and tissues of interest. In addition, bSSFP may lead to increased specific absorption rate and RF-induced device heating at 3 T[13]. Therefore, in this study at 3 T, we used an RF-spoiled GRE sequence for real-time MRI. For applications at 1.5 T or under acceptable conditions, bSSFP may be a desirable option for real-time MRI and would certainly be compatible with our proposed fusion-based framework for motion prediction.

Using the same stream of GA radial MRI data, reconstruction windows can be flexibly selected to reconstruct images for image-based and surrogate-based motion tracking (**Figure 2-1**). 70/16 and 16/16 radial spokes (reconstruction window-temporal footprint/sliding window-temporal resolution) were selected as two specific examples in this work, corresponding to radial undersampling factors of 4 and 20. Wide temporal footprint images achieved higher SNR with less radial streaking artifacts and good depiction of anatomical structures around the liver. On the other hand, narrow temporal footprint images have lower SNR with more streaking artifacts. Detailed tissue features are not well visualized in these images due to streaking and only the overall boundaries or gross features of the organs are visualized. Therefore, we tracked the overall motion of the liver to provide a surrogate signal for the motion of the target regions inside the liver. We used a temporal resolution of 16 spokes (corresponding to 100 ms) for the sliding-window reconstruction, which is comparable to the computation time for non-Cartesian SENSE reconstruction in the pipeline. In practice, the image temporal resolution (i.e., frame rate) should be similar to the reconstruction computation time to avoid congestion within the real-time MRI pipeline and improve the reliability of the pipeline in longer scans. The chosen temporal resolution of 100 ms (frame rate 10 Hz) in our experiments is able to resolve respiratory motion. During our selection of GA radial MRI parameters, we also tested an intermediate temporal footprint (i.e., 40 spokes) for either image-based or surrogate-based tracking, but this did not change the findings; the fusion-based prediction method still demonstrated clear improvements over image-based and surrogate-based methods.

To extend the current implementation of the software pipeline to provide realistic intra-procedural and real-time MRI guidance, multiple targets (e.g., tissue targets and interventional devices) should be tracked and visualized for decision support. The tracking of multiple targets and visualization should be performed in parallel to minimize latency. In an additional evaluation, we parallelized the tracking of multiple targets in the pipeline and found that additional targets would only introduce less than 10 ms of latency for image-based motion tracking, which is negligible compared with the overall system latency (300-400 ms). Therefore, the current real-time MRI pipeline and motion prediction framework can be extended to track multiple targets and provide motion information feedback for interventional applications.

For the retrospective study, the *in vivo* liver images were reconstructed using the same software pipeline in offline mode. The motion tracking and prediction methods were implemented using the entire stream of the images with different temporal footprints retrospectively. The framework was emulated to receive images as if they were acquired online, using actual measured latencies, and without additional information beyond the current measurement time. The actual measured latencies from two separate scanners with the same software pipeline were similar, demonstrating the stable performance of the pipeline. Using the actual latencies in the retrospective study provided prediction results that emulate actual online conditions. The motion coordinates retrospectively extracted from wide temporal footprint images using image-based template matching were used as the reference to evaluate the prediction of translation motion for tissue regions of interest. This choice was supported by the results from the online tracking experiments using the motion phantom, and also by the fact that non-rigid motion of organs due to breathing can be modeled as a set of local linear translations of smaller tissue regions[99]. The system and patient-induced geometric inaccuracies were minimized by choosing appropriate sequence parameters (e.g., readout bandwidth)[100], applying radial trajectory correction, and using vendor-provided gradient warping correction. The surrogate-based tracking error calibrated in the online tracking experiment was still underestimated due to the perfect rigid body motion of the designed phantom. Uncertainty of the correlation model due to non-rigid body motion for different regions of interest could introduce more tracking error. We extracted the surrogate signals of the target feature motion directly from the narrow temporal footprint GA radial MR images. No additional markers or system hardware components were required, which reduces the complexity of the online implementation. A denoising Kalman filter was applied to the surrogate signal to establish a robust correlation model. We also applied an EM training algorithm to the first 30-sec of the surrogate signals to obtain a state space model for the denoising Kalman filter. The initial covariance matrix $R$ was larger than the covariance matrix during the training step for motion prediction since the input surrogate signal was noisier.

Kalman filter-based motion prediction mainly relies on the state space model. The temporal characteristics of respiratory motion varies for different subjects and may change over time. Based on a previous study of Kalman filtering[89], EM training can significantly improve the prediction accuracy. Therefore, to adapt to motion characteristics, we used the EM training algorithm to estimate the model parameters (*A, H, Q, R*). This step required 1-5 sec of computation before real-time processing started. Therefore, the majority of the time required for training is still the acquisition time of the training data (30 sec). As a result, EM training is currently a feasible approach to improve Kalman filter-based respiratory motion prediction.

The retrospective *in vivo* results demonstrated that the proposed multi-rate fusion-based method is able to achieve significantly lower error than image-based and surrogate-based methods. The prediction performances using image-based and surrogate-based motion tracking were not significantly different based on RMSE. This was due to a trade-off between system latency (better for surrogate-based tracking) and motion tracking spatial accuracy (better for image-based tracking) for respiratory motion prediction under current imaging parameters. However, the surrogate-based method was slightly better than the image-based method based on $\varepsilon_{2.5}$, demonstrating its advantage for removing outliers. By using the fusion-based prediction method, we combined the advantages of low latency from surrogate-based tracking with higher spatial accuracy (lower error) from image-based tracking. The reduced error of the fusion-based method was demonstrated for all waveforms and specific types of breathing patterns (normal, shallow, deep), providing evidence for its robustness. In terms of RMSE, which evaluated the average performance, the relative improvements of the fusion-based method vs. the surrogate-based method and image-based method were around 18% (0.97 mm vs. 1.18 mm) and 25% (0.97 mm vs. 1.3 mm). In terms of $\varepsilon_{2.5}$, which evaluated the ability to remove outliers, the relative improvements of the median and IQR using the fusion-based method were about 30% (2.5% vs. 3.5%) and 35% (5.5% vs. 8.5%) vs. the surrogate-based method, and 60% (2.5% vs. 6.2%) and 62% (5.5% vs. 14.4%) vs. the image-based method, respectively. For shallow breathing and normal breathing, the breathing rate was relatively higher, and the image-based method suffered from latency issues. The fusion-based method incorporated rapid surrogate-based information to overcome latency and achieved notable improvement compared with the image-based method for shallow breathing. On the other hand, deep breathing typically has lower breathing rates which can be tolerable in the presence of longer latency for the image-based method. However, greater amplitude variations in the waveform during deep breathing leads to more model inconsistency related errors for surrogate-based tracking. The fusion process was able to reduce this error by incorporating delayed measurements from image-based tracking. Therefore, the fusion-based method achieved the most improvement compared with the surrogate-based method for deep breathing. Median RMSE and $\varepsilon_{2.5}$ of the prediction error had relative improvements of about 16% (1.4 mm vs. 1.17 mm) and 37% (5.4% vs. 3.4%), respectively. Importantly, the fusion-based method markedly improved the consistency of reducing outliers, as evidence by a 77% relative reduction of the IQR for $\varepsilon_{2.5}$ (17.5% vs. 4.1%).

Our current study has some limitations. First, the prediction methods were only evaluated in one dimension, the superior-inferior (SI) direction, which is the dominant direction of motion caused by breathing[39]. The proposed framework can be readily extended into all three dimensions by acquiring more imaging planes (or a 3D volume) and tracking the three-dimensional target tissue motion in the regions of interest. An interleaved orthogonal 2-slice approach (i.e., sagittal and coronal) with golden-angle radial MRI can still achieve a framerate of 5 Hz, which is adequate for visualizing organ motion during free breathing (typically 3-5 secs/period). Second, the 75 motion waveforms used for evaluation were obtained from 8 different subjects with 3 breathing patterns and may have some internal correlation because different regions were selected from the same image series. Third, the current implementation and experiments only consider two different components in the multi-rate framework (one surrogate-based agent and one image-based agent). The fusion-based method need not be limited to the specific parameters we used in this study. With improved reconstruction algorithms for higher radial undersampling factors, such as robust dynamic estimation[101], GPU acceleration[102], or deep learning[103,104], the performance could be further improved. Future developments could incorporate tracking results from a wider range of MRI acquisition and reconstruction techniques and external signals into the multi-rate prediction framework. In addition, even though all of the components in the fusion-based method (MRI acquisition and reconstruction, motion tracking, fusion, motion prediction) are designed for online real-time implementation without any hidden delays, the real-time performance of the fusion-based method still needs to be evaluated by fully implementing it in our online pipeline.

## 2.5 Conclusion

In summary, we presented a fusion-based respiratory motion tracking and prediction framework using multi-rate Kalman filtering and real-time GA radial MRI. This framework combines the respective advantages of surrogate-based tracking (lower latency) and image-based tracking (lower tracking error). Experiments demonstrate that the fusion-based method can achieve temporal resolution of 100 ms (10 Hz frame rate) and overcome system latencies (~300 ms) to provide sub-pixel prediction error (0.97±0.49 mm) of targets in the liver during respiratory motion. This framework has potential to improve the tracking accuracy of tissue targets for computer-assisted navigation, real-time MRI-guided interventions, and image-guided therapies.

*This work has been published as:* ***Li X****, Lee Y, Mikaiel S, Simonelli J, Tsao T, Wu HH. Respiratory Motion Prediction Using Fusion-Based Multi-Rate Kalman Filtering and Real-Time Golden-Angle Radial MRI. IEEE Trans Biomed Eng 2020;67(6):1727-1738.*

# Chapter 3 Automatic Needle Tracking using Mask R-CNN for MRI-Guided Percutaneous Interventions

## 3.1 Introduction

Image-guided percutaneous interventions play key roles in cancer diagnosis and treatment[1,2]. Under image guidance, physicians manipulate needles to access targets in suspected lesions for different purposes (e.g., needle biopsy, focal ablation). With the advantages of high soft tissue contrast and no ionizing radiation, magnetic resonance imaging (MRI) has emerged as a promising intra-procedural imaging modality[14,34]. MRI can provide needle visualization based on the passive signal void feature on the MR images caused by needle-induced susceptibility effects to guide needle manipulation during procedures[105-107]. For example, during intra-procedural or real-time MRI-guided interventions, needle-in scans are used to visualize both the needle feature and the target to assist needle position adjustment[7,65,66,108-110]. However, there are variations in the signal void feature and contrast between the needle feature and surrounding tissues depending on the MRI sequence type and parameters, the type of needle, and the needle's orientation relative to the $B_0$ field. These variations may lead to inaccurate interpretation of the needle position and result in several iterations of adjustments or even errors in the final placement.

Computer-assisted automatic needle feature localization and tracking could provide multiple benefits for image-guided procedures. For in-bore MRI-guided prostate biopsy, fast and accurate determination of the spatial relationship between the needle feature and the target has potential to improve the workflow for adjusting the needle guide position. Automatic needle tracking could provide closed loop confirmation of needle placement and improve the physicians' confidence in assessing procedural accuracy[7]. Furthermore, the information from needle tracking could be used to directly adjust the needle trajectory for future development of feedback-controlled robotics-assisted procedures, which is an emerging area of research[111-113]. The needle tracking algorithm could also be used as a postprocessing tool for needle path analysis using procedural images; this would provide more information about the needle trajectory and placement accuracy to improve procedure planning[114]. Therefore, developing algorithms that automatically and reliably track the needle feature on MR images has potential to improve intra-procedural guidance and postprocedural analysis of MRI-guided percutaneous interventions.

The common computer-aided algorithms to locate or track the needle on images require detection and segmentation of the needle feature, which has a long tubular structure. Strategies for needle tracking have been presented in the literature for different imaging modalities (e.g., MRI, ultrasound), but these methods are less robust when the needle insertion length was not enough or confounding long tubular features were present in the image background[107,115,116]. Supervised deep learning using convolutional neural networks (CNN) is a powerful approach for image classification and segmentation[117]. Recent work in ultrasound has shown that compared with hand-crafted pre-determined feature extraction methods, supervised deep learning-based methods have superior ability to overcome these challenges[118]. CNNs have also been applied to pixel-based segmentation of the needle feature on MRI. For example, a 3D fully convolutional network (FCN) was proposed to segment the cross-sectional needle feature in a set of 3D image planes for in-bore MRI-guided prostate biopsy[54]. Another study adapted the U-Net for dynamic in-plane needle feature segmentation on real-time 2D MRI[53]. However, the residual errors after pixel-based segmentation using CNNs degraded the instance detection of the needle feature[53,54]. Ensemble algorithms to accumulate detection candidates reduced residual errors, but increased the number of parameters for tuning and the processing time[54]. The region proposal based CNN (R-CNN)[119], which automatically integrates region of interest (ROI) localization within the network, may direct the strong classification power of CNNs to the proposed regions instead of each pixel and enable the formation of an end-to-end learning framework for improved instance segmentation of the needle feature. Recent developments of Mask R-CNN[119] further include an additional mask branch to precisely determine the region containing the object feature[119] while improving the robustness of the object feature segmentation task.

Mask R-CNN is fast and accurate for instance-level object detection and segmentation in natural images[119]. The variations of the target objects' features in natural images are similar to the challenges of passive needle tracking on MRI. Therefore, our objective in this study was to adapt and train Mask R-CNN for needle feature detection and segmentation on interventional MR images. We also developed an algorithm to automatically track the needle tip location and axis orientation based on the Mask R-CNN output. We evaluated the performance of the proposed automatic needle tracking algorithm using datasets from intra-procedural MRI-guided prostate biopsy and real-time MRI-guided needle insertion in *ex vivo* tissue.

## 3.2 Methods

### 3.2.1 Network Structure

We implemented Mask R-CNN using Keras and Tensorfow[119] (**Figure 3-1**). The input grayscale 2D MR images were stacked into 3 color channels, and the needle signal void feature on 2D MR images was defined as the only non-background class. In the output, the bounding box indicates the ROI corresponding to needle feature detection, while the predicted mask (within the bounding box) corresponds to needle feature segmentation.

### 3.2.2 Datasets

*(1) Gel phantom dataset:* A gel phantom (gelatin concentration 70 g/L) was imaged using a 2D real-time golden-angle (GA) ordered radial spoiled gradient echo (GRE) sequence (**Table 3-1**, second column)[120,121]. The images were reconstructed using a non-Cartesian conjugate gradient sensitivity encoding (cgSENSE) algorithm[38,95]. Dynamic needle (10 cm, 18 gauge, Invivo) insertion and retraction was performed using manually controlled MRI-compatible master–slave hydrostatic actuators during the scan[66]. One degree of freedom (1-DOF) needle manipulation in 11 different angles relative to the $B_0$ field was performed during the scan. 145 images were randomly selected from all scans to form a pretraining dataset.

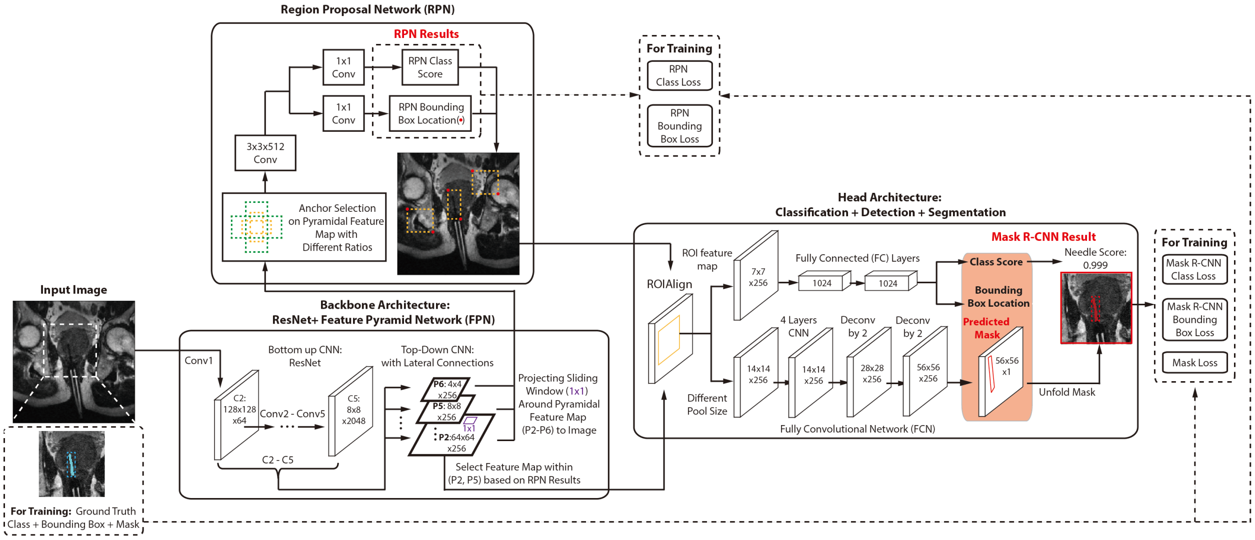

**Figure 3-1 Structure of Mask R-CNN for Needle Detection and Segmentation. In the backbone, a Residual Network (ResNet) and Feature Pyramid Network (FPN) extract features from the entire input image. The feature maps are shared with a Region Proposal Network (RPN) to generate an initial Region of Interest (ROI), indicated by a bounding box. In the head architecture, the proposed ROI and corresponding feature map are processed by the ROIAlign layer. The fixed-size ROI feature map is exported for ROI refinement to obtain the final class score, ROI bounding box location, and predicted mask. Based on the bounding box location, the mask will be transformed back into the original image size. The components outlined in dashed lines were used for training. Conv: convolution.**

*(2) Prostate dataset:* In an IRB-approved and HIPAA-compliant retrospective study, intra-procedural $T_2$-weighted prostate MRI using a turbo spin echo (TSE) sequence (Table 1, first column) was collected from 125 in-bore MRI-guided transrectal prostate biopsy cases, which were performed according to previous work[7]. A 17.5-cm 18-gauge MR-compatible biopsy needle (TSK Laboratory) was inserted through the needle guide, and intra-procedural TSE scans were acquired to confirm the needle location. Multiple parallel 2D image slices were acquired in oblique sagittal, coronal, or transversal plane orientations. A trained researcher selected intra-procedural images containing the needle signal void feature in oblique transversal and sagittal orientations and divided them into separate training (85 cases/250 images) and testing datasets (40 cases/208 images).

*(3) Tissue dataset:* Firstly, *ex vivo* tissue samples were imaged using a 2D real-time GA ordered radial spoiled GRE sequence for training (Table 1, third column). Two different echo times (TE=1.9 ms and 3 ms) were used to generate images with different contrasts. The images were acquired in the coronal plane and reconstructed in the same manner as the gel phantom dataset. 1-DOF needle (15 cm, 20 gauge, Cook Medical) manipulation in 9 different angles relative to the $B_0$ field was performed using actuators during the scan. One hundred eighty images of a pork shoulder were randomly selected to form a training dataset. Next, different tissue samples (beef steak) were used to repeat the scan with free-hand 2-DOF (translation and rotation) needle manipulation within a 2D plane. Different contrasts (i.e., TE), slice orientations, and needle types (needle 1: 15 cm, 20 gauge, Cook Medical; needle 2: 10 cm, 18 gauge, Invivo) were used to acquire three different real-time MRI datasets. Each dataset contained 300 image frames, and 30 images were randomly selected from each dataset to form a testing dataset to evaluate Mask R-CNN needle feature segmentation (total of 90 images).

### 3.2.3 Mask R-CNN Training and Testing

A researcher, trained and supervised by a clinical interventional radiology fellow and experienced interventional radiologist, manually segmented the needle signal void features on the MR images. All images in the training datasets underwent 16-fold image augmentation by random rotation (0°–360°), flipping, translation, and rescaling to mitigate overfitting. We pretrained the network using the common object in context (COCO)[122] and gel phantom datasets to improve convergence during training[123] for the prostate and ex vivo tissue datasets. Losses from the head architecture and residual proposal network (RPN) were equally weighted (**Figure 3-1**)[119,124]. The specific training hyperparameters are in **Table 3-2**.

To evaluate needle detection and segmentation using Mask R-CNN, we studied separate testing datasets of intra-procedural prostate MRI (208 images) and ex vivo tissue real-time MRI (90 images). For images with successful needle detection, the intersection over union (IoU, 0 to 1) and center of mass shift (COMs, in mm) of the segmentation mask were calculated with respect to the reference human annotation for each individual image.

**Table 3-1 MRI Datasets and Imaging Parameters. Intra-procedural prostate $T_2$-weighted MRI from in-bore MRI-guided biopsy, real-time MRI of a gel phantom, and real-time MRI of *ex vivo* tissue were used to train and test the proposed algorithms. TR: repetition time. TE: echo time. N/A: not applicable.**

| | **Prostate $T_2$-Weighted MRI** | **Real-Time MRI of Gel Phantom** | **Real-Time MRI of *Ex vivo* Tissue** |
|---|---|---|---|
| **TR / TE** | 3700 ms / 92 ms | 6.0 ms / 2.47 ms | 4.16 ms / 1.9 ms;<br>5.26 ms / 3 ms |
| **Field of View** | 220 mm x 220 mm | 300 mm x 300 mm | 300 mm x 300 mm |
| **Matrix Size** | 256 x 256 | 256 x 256 | 256 x 256 |
| **In-Plane Resolution** | 0.86 mm x 0.86 mm | 1.2 mm x 1.2 mm | 1.2 mm x 1.2 mm |
| **Slice Thickness** | 4 mm | 5 mm | 5 mm |
| **Flip angle** | 150° | 12° | 12° |
| **Acquisition Time (Number of Dynamic Frames)** | 34.3 sec<br>(N/A) | 28.8 sec<br>(300 frames) | 20.1 - 25.2 sec<br>(300 frames) |
| **Dynamic Temporal Resolution/ Footprint** | N/A | 96 ms / 330 ms | 67 - 84 ms /<br>228.8 - 261.8 ms |
| **Orientation** | Oblique Transversal and Sagittal | Coronal | Coronal and Sagittal |

**Table 3-2 Mask R-CNN Training Parameters. A fixed size of 56x56 pixels was used in the mask branch. Training was performed using Adam with Nesterov momentum on two Nvidia 1080Ti GPU cards with 12 GB of memory each.**

| | |
|---|---|
| **Batch Size** | 4 |
| **Epoch Steps** | 100 |
| **Weight decay regularization** | 0.004 |
| **$\beta_1$** | 0.9 |
| **$\beta_2$** | 0.9999 |
| **Learning Rate** | 0.0002 |
| **Epoch Number** | 60 |
| **Training Time** | ~2 hours |

### 3.2.4 Automatic Needle Feature Localization Algorithm and Evaluation for Prostate Dataset

To automatically localize the needle feature tip location and axis orientation based on Mask R-CNN outputs, we developed a postprocessing algorithm (**Figure 3-2**). For images with a positive detection of the needle feature, orthogonal distance regression (ODR)[125] was applied to the needle segmentation mask to extract the needle tip position and needle axis orientation angle in image coordinates (**Figure 3-2**). The Mask R-CNN performs instance-level segmentation and always detected the contiguous needle feature as one instance. In some cases, other dark features in the anatomical background mimicked needle features and were detected by the Mask R-CNN, albeit with a lower class score. We set a class score threshold of 0.99 to remove these false positive detection instances. This simple instance-level threshold approach had much less computational overhead than the test-time augmentation step used for a previous semantic segmentation method[54]. Since only one needle was used during biopsy procedures, if multiple positive ROIs were still detected after applying the threshold, the ROI with highest class score was considered to be positive detection of the needle.

A clinical interventional radiology fellow with experience performing in-bore MRI-guided prostate biopsy[7] annotated the needle feature tip location and axis orientation on the images of the intra-procedural prostate MRI testing dataset. There were only two cases in the testing dataset with visible needle shaft, but without visible needle tip feature due to marked obliqueness of the needle axis with respect to the image plane. When the expert labeled these two cases, he used the needle feature on the adjacent slice to estimate the needle tip position on the slice of interest. Absolute needle axis orientation difference ($d\theta$, in degrees) and Euclidean distance of needle tip position ($dxy$, in mm) between the algorithm results and the human reference were calculated for evaluation.

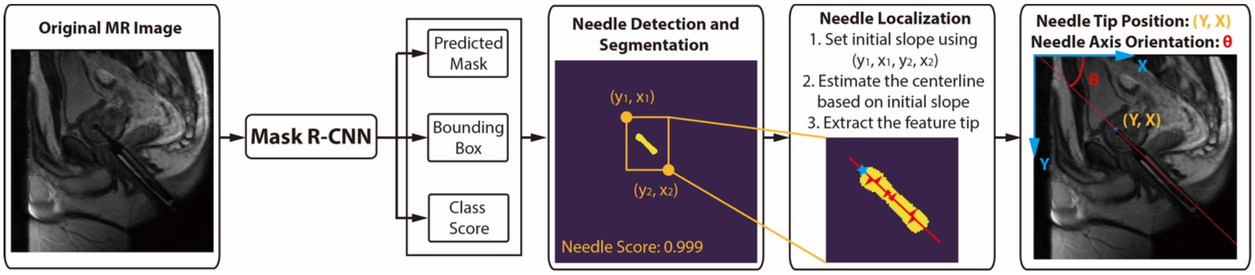

**Figure 3-2 Automatic Needle Tracking Algorithm. The MRI needle signal void feature caused by susceptibility is nearly symmetric, thus the needle axis should be along the centerline of the segmentation mask generated from Mask R-CNN. The location of the centerline was estimated with orthogonal distance regression using the entire needle segmentation mask. The signal drop along the detected axis was used to identify the needle feature tip (blue star)**

### 3.2.5 Dynamic Needle Feature Tracking and Evaluation for *Ex Vivo* Tissue Dataset

We evaluated the needle feature localization algorithm for dynamic needle feature tracking in 3 *ex vivo* tissue real-time MRI datasets with 2-DOF needle motion. If multiple positive needle detection results from Mask R-CNN were reported for a frame, only the bounding box closest to the positively detected needle feature in the previous frame was designated as the positive needle detection result. The needle feature tracking results in X and Y directions in image coordinates were calculated by subtracting the localized needle position in the initial frame from the needle localization results in each subsequent dynamic frame. The image coordinate system can be transformed to the patient coordinate system based on slice position. A small ball-shaped needle feature without a well-delineated shaft may appear on the images when the needle was aligned with the $B_0$ field. In this case, ODR may produce an incorrect estimation of the needle axis. Therefore, since the needle manipulation speed was relatively stable, axis localization results in a frame were replaced by the results of the previous image frame if the change in axis orientation was over a threshold of 8°. For evaluation, tracking references were manually annotated by a researcher, trained and supervised by the interventional radiology fellow. The absolute differences between the algorithm tracking results and the human references were calculated.

## 3.3 Results

### 3.3.1 Mask R-CNN Evaluation for Prostate and *Ex Vivo* Tissue Datasets

Representative needle feature detection and segmentation results from Mask R-CNN for one prostate image in oblique transversal orientation and another one in oblique sagittal orientation are shown in **Figure 3-3a**. For the prostate MRI testing dataset, needle detection was 99% successful; only two needle detection cases failed out of 208 images because the needle axis was markedly oblique in the through-plane direction (**Figure 3-7**). Median [interquartile range; IQR] of IoU was 0.737 [0.153] and median [IQR] of CoM shift was 1.25 [1.19] mm, which was about 1.5 [1.4] pixels. Next, representative needle detection and segmentation results for ex vivo tissue real-time MRI with 2-DOF needle motion are shown in **Figure 3-3b**. Needle detection was 100% successful for the 90 images in the testing dataset. Median [IQR] of IoU was 0.719 [0.143] and median [IQR] of CoM shift was 1.65 [1.27] mm, which was about 1.4 [1.1] pixels. The inference time of the network was in the range of 60–68 ms per image.

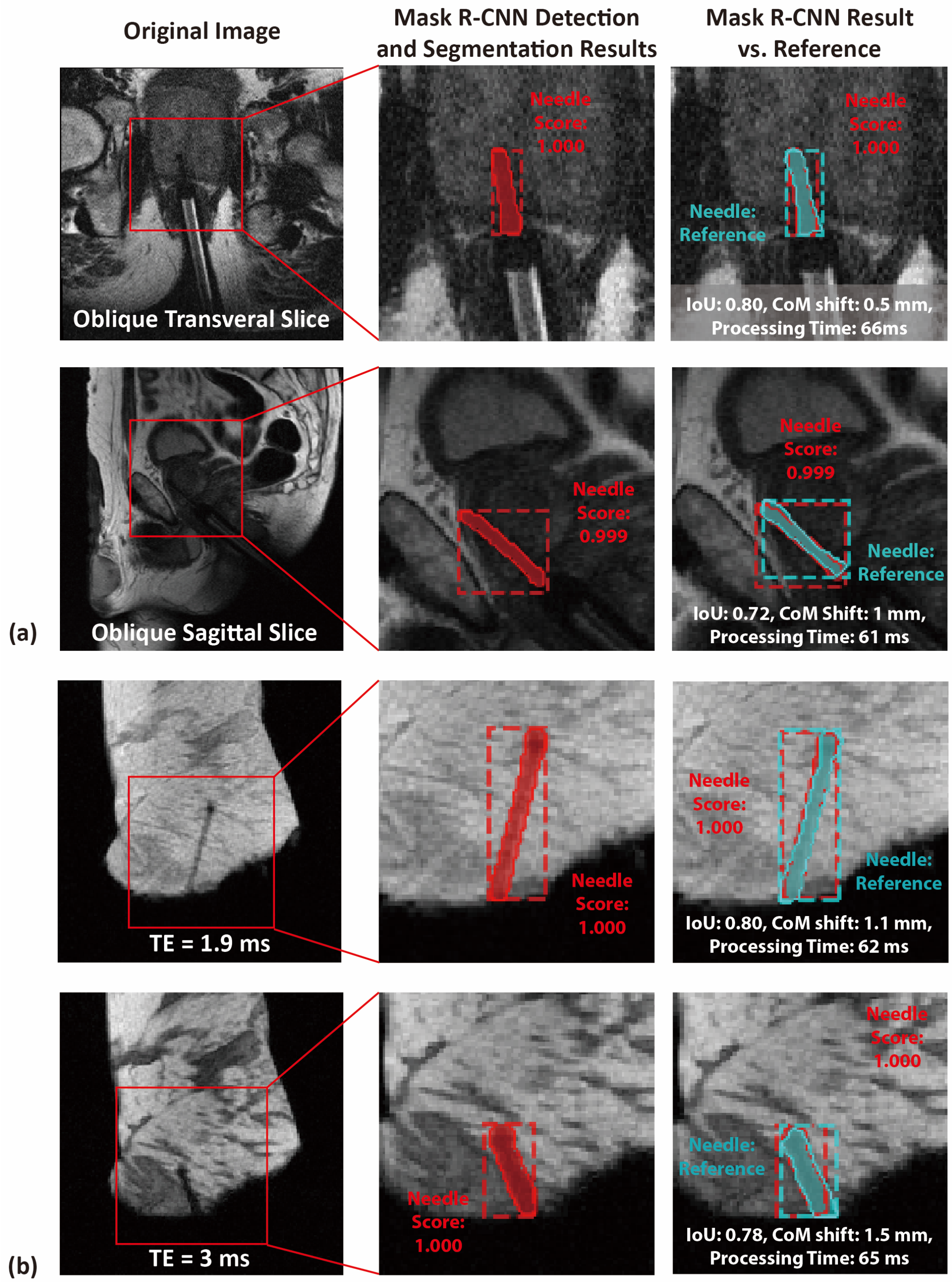

**Figure 3-3 Example Needle Detection and Segmentation Results for Intra-Procedural Prostate MRI and *Ex Vivo* Tissue Real-Time MRI. Mask R-CNN results are shown for (a) intra-procedural prostate MRI in different slice orientations and (b) *ex vivo* tissue real-time MRI with different contrasts (i.e., echo time, TE). The needle detection scores are reported in the middle and right columns. The prediction results vs. the references are reported in the right column. The processing time is also reported. IoU: intersection over union. CoM: center of mass.**

### 3.3.2 Needle Feature Localization Evaluation for Prostate Dataset

In the prostate MRI testing dataset, there were only 8 Mask R-CNN results that contained more than one positive detected ROI. With a class score threshold of 0.99, 6 of them were removed. Needle detection in the remaining 2 cases were successfully accomplished by selecting the ROIs with the highest class scores. Example human reference and algorithm localization results for intra-procedural prostate MRI are shown in **Figure 3-4**. Median, IQR, mean, standard deviation (SD), and root mean square error (RMSE) of dxy and dθ between algorithm results and the human reference are reported in **Table 3-3**. Histograms of dxy and dθ are shown in **Figure 3-5**. The majority (>80%) of dxy were <2 mm and dθ were <3°. The median value of dxy for needle tip tracking was 0.71 mm (~0.82 pixels), while the median value of dθ for axis tracking was 1.28°.

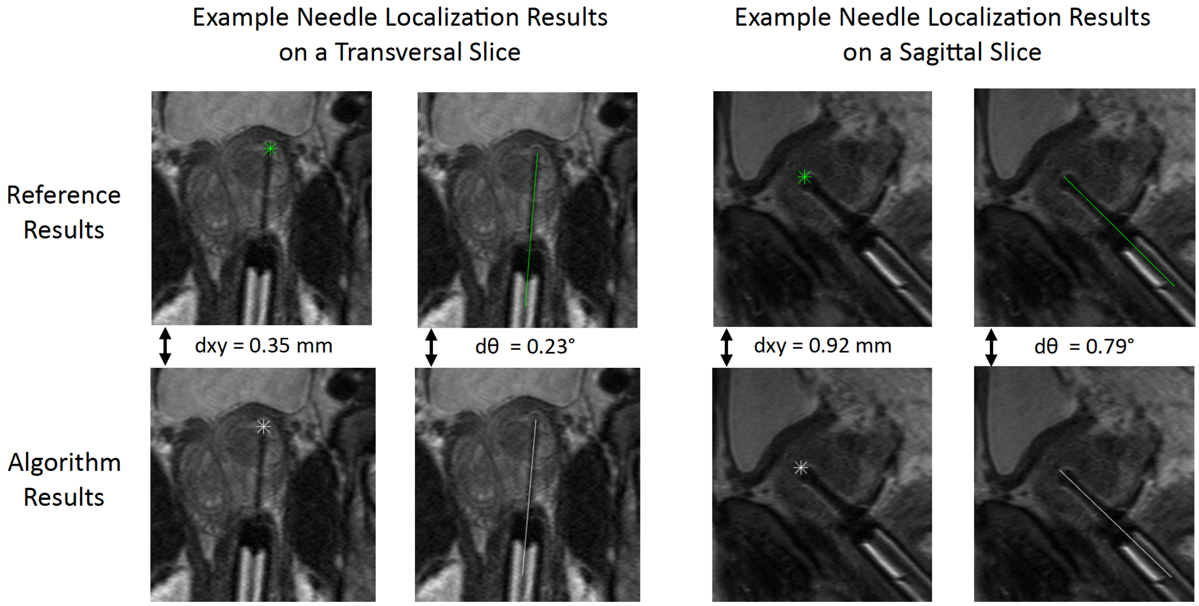

**Figure 3-4 Example Automatic Needle Localization Results for Intra-Procedural Prostate MRI. Needle tip location (*) and needle axis orientation (line) were computed based on the predicted mask from Mask R-CNN. Example comparisons between reference results (green) and algorithm results (white) are shown. The Euclidean distance between the needle tip locations (dxy) and the absolute difference between the needle axis orientations (dθ) are reported.**

**Table 3-3 Automatic Needle Localization Results for Intra-Procedural Prostate MRI. In a testing set of 40 patients and 208 images, the algorithm results were evaluated with respect to a human reference in terms of the Euclidean distance between the needle tip locations (dxy) and the absolute difference between the needle axis orientations (dθ). The median and interquartile range (IQR), mean and standard deviation (SD), and root mean squared error (RMSE) are reported.**

| | **Algorithm vs. Human Reference** | |
|---|---|---|
| | **dxy (mm)** | **dθ (°)** |
| Median | 0.71 | 1.28 |
| IQR | 1.01 | 1.91 |
| Mean | 1.28 | 1.73 |
| SD | 1.39 | 1.49 |
| RMSE | 1.8 | 2.28 |

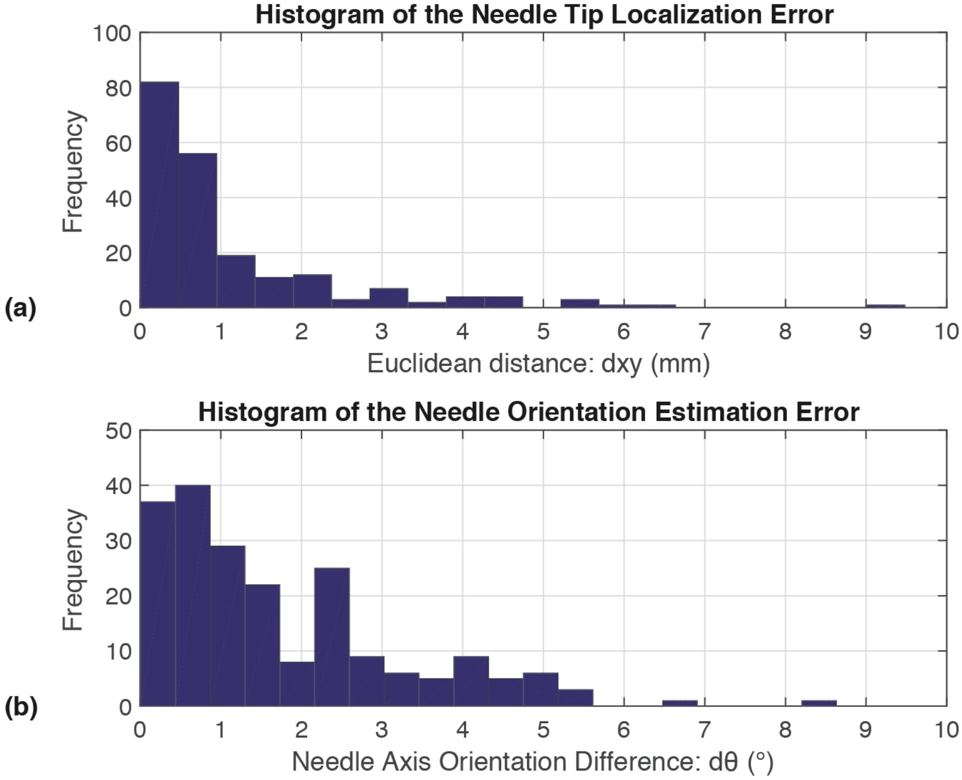

**Figure 3-5 Histogram of Needle Localization Results for Intra-Procedural Prostate MRI. The histograms show (a) needle tip localization differences (dxy) and (b) axis orientation absolute differences (dθ) between the automatic needle localization algorithm and a human reference.**

### 3.3.3 Dynamic Needle Feature Tracking Evaluation for *Ex Vivo* Tissue Dataset

For *ex vivo* tissue real-time MRI datasets, the needle feature tracking results for images with different contrasts, needle type, and imaging plane orientations are shown in **Figure 3-6**. The range of the needle tip displacement during free-hand 2-DOF manipulation was 42.6 mm, 38.1 mm, and 32.1 mm in Y, and 11.7 mm, 19.5 mm, and 24.3 mm in X, for the three experiments. The range of the needle axis orientation angle was 15.4°, 26.4°, and 11.2° for the three experiments. These ranges are representative of actual needle motion during procedures[126]. The overall tracking results (dxy and dθ) for all real-time MRI datasets are shown in **Table 3-4**. The median values of dxy for the three datasets were 0.90 mm (~0.77 pixels), 1.31 mm (~1.12 pixels), and 1.09 mm (~0.93 pixels). The median values of dθ for the three datasets were 1.53°, 1.9° and 0.97°. This was consistent with the dxy (in terms of pixels) and dθ results in the prostate MRI testing dataset. The processing time of the whole algorithm for each image was around 75 ms.

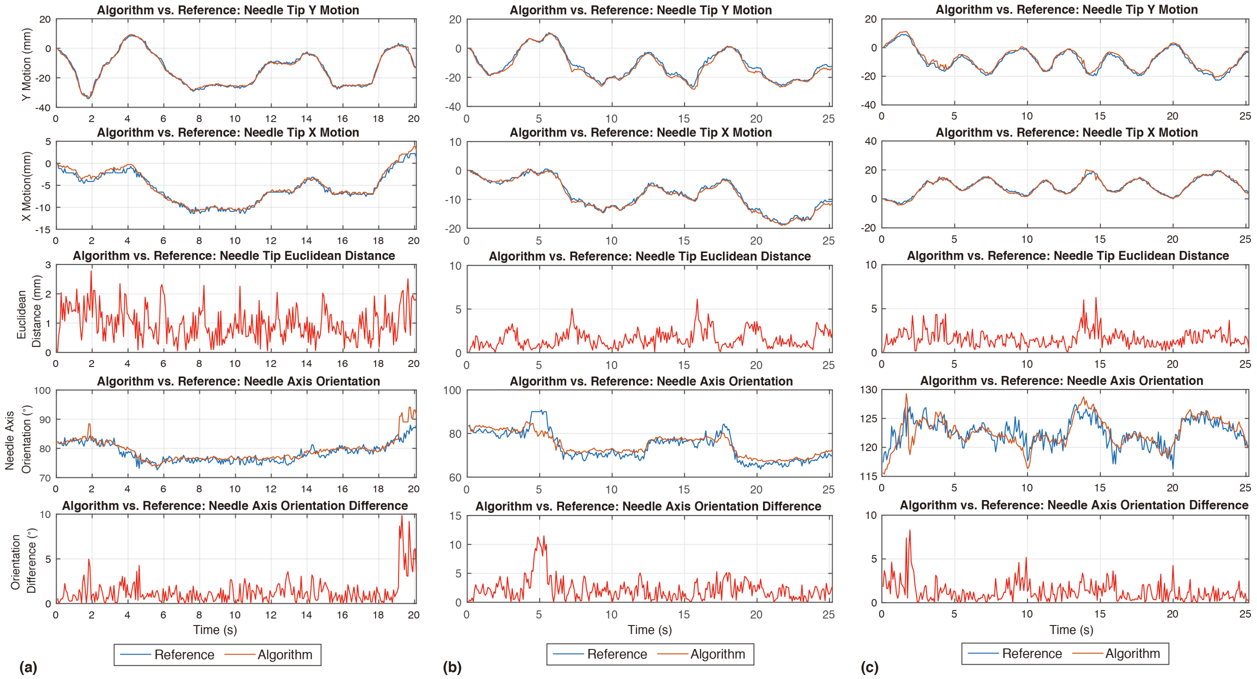

**Figure 3-6 Example Automatic Needle Tracking Results for Real-Time *Ex Vivo* Tissue MRI. The needle tip motion and change in axis orientation over time were compared between the algorithm and a human reference in 3 real-time MRI datasets (parameters in Table 1, third column). (a) Coronal slice, echo time (TE) of 1.9 ms, with needle 1 (15 cm, 20 gauge, Cook Medical). (b) Coronal slice, TE of 3 ms, with needle 1. (c) Sagittal slice, TE of 3 ms, with needle 2 (10 cm, 18 gauge, Invivo). Y and X were defined in terms of the image coordinates. Overall needle tracking performance for each dataset is reported in Table 4.**

**Table 3-4 Automatic Needle Tracking Results for Real-Time *Ex Vivo* Tissue MRI. 3 real-time MRI testing datasets were obtained with different imaging contrasts (echo time, TE) and needle types (Needle 1: 15 cm, 20 gauge, Cook Medical; Needle 2: 10 cm, 18 gauge, Invivo). The algorithm results were evaluated with respect to a human reference in terms of the Euclidean distance between the needle tip locations (dxy) and the absolute difference between the needle axis orientations (dθ). The median, interquartile range (IQR), mean, standard deviation (SD), and root mean squared error (RMSE) are reported. The characteristics of needle motion are also reported: total time, total number of frames, and range of motion in the Y and X directions in the image coordinate.**

| | **(a) *Ex vivo* Tissue: TE = 1.9 ms, Needle 1** | | **(b) *Ex vivo* Tissue: TE = 3 ms, Needle 1** | | **(c) *Ex vivo* Tissue: TE = 3 ms, Needle 2** | |
|---|---|---|---|---|---|---|
| | **dxy (mm)** | **dθ (°)** | **dxy (mm)** | **dθ (°)** | **dxy (mm)** | **dθ (°)** |
| Median | 0.90 | 1.53 | 1.31 | 1.90 | 1.09 | 0.97 |
| IQR | 0.53 | 1.51 | 0.98 | 2.15 | 0.76 | 1.22 |
| Mean | 0.99 | 1.70 | 1.56 | 2.20 | 1.26 | 1.28 |
| SD | 0.55 | 1.26 | 0.98 | 1.97 | 0.82 | 1.17 |
| RMSE | 1.13 | 2.10 | 1.84 | 3.00 | 1.5 | 1.71 |
| Total time | 20.8 sec | | 25.2 sec | | 25.2 sec | |
| Total frames | 300 | | 300 | | 300 | |
| Slice Orientation | Coronal | | Coronal | | Sagittal | |
| Range (Y) | 42.6 mm | | 38.1 mm | | 32.1 mm | |
| Range (X) | 11.7 mm | | 19.5 mm | | 24.3 mm | |
| Range (θ) | 15.4° | | 26.4° | | 11.2° | |

## 3.4 Discussion

In this study, we adapted and trained Mask R-CNN for needle feature detection and segmentation on intra-procedural and real-time MR images. Pixel-level spatial accuracy was consistently achieved for both needle feature tip localization in the prostate dataset (median dxy: 0.82 pixels) and needle feature tracking in the tissue dataset (median dxy: 0.7–1.1 pixels) based on the Mask R-CNN results. These results were achieved by fine-tuning with relatively small training datasets (prostate dataset: 250 images, ex vivo tissue dataset: 180 images) using the same training hyperparameters. A previous study using a 2D pixel-based deep learning method for MRI-based in-plane needle feature segmentation and localization had on average 3 falsely detected needle contours per image and error of ~4 pixels for needle tip localization[53]. In contrast, the detection errors at the instance level using Mask R-CNN were negligible and needle tip localization errors were substantially lower (~1 pixel) in our results. Compared with a previous study[54] that used a 3D CNN for pixel-level semantic segmentation, our study used the high in-plane resolution of 2D images and Mask R-CNN for instance segmentation; both methods achieved comparable needle localization errors. No ensemble step or test time augmentation was required for our technique, which enabled rapid overall processing times (75 ms per image). Therefore, our results demonstrate that Mask R-CNN is a deep learning framework with important advantages for real-time needle detection and segmentation on MR images

For the intra-procedural prostate MRI dataset, we assumed a rigid linear needle profile. This was supported by the fact that the transrectal approach utilizes a needle guide and has minimal needle bending[54]. 86.5% of the absolute needle tip localization error (dxy) was <2.5 mm, demonstrating the potential for our algorithm to support interventions in clinically relevant tissue targets, which typically have diameters of 5–10 mm or greater[56,127]. The needle position information provided by our algorithm has potential to improve the physician's assessment of procedural accuracy during MRI-guided biopsy, or to automatically adjust the needle trajectory for robotics-assisted procedures[54,128]. In addition, our method can be adapted for needle detection on intra-procedural MRI of transperineal prostate biopsy, and the existing network structure could be extended to consider 3D prostate MRI. For the *ex vivo* tissue real-time MRI dataset, since the operator carefully maintained a straight path for needle insertion during the experiments, the assumption of a rigid linear needle profile achieved accurate tracking of dynamic needle motion (median dxy: 0.7–1.1 pixels). These results indicate that our proposed real-time algorithm has potential to provide accurate feedback information for automatic needle control.

We investigated the robustness of the Mask R-CNN for needle detection and segmentation on MRI with respect to different characteristics: different anatomical backgrounds from different subjects, different image plane orientations, different needle lengths, different needle orientations, and different needle feature widths and image quality due to the selection of two types of bandwidth for the scans. Among these characteristics, marked obliqueness of the needle axis with respect to the image plane is a factor that may lead to detection failure (<1%: 2 out of 208 images). In the prostate MRI testing dataset, we quantified the obliqueness by comparing the centerline of the needle feature with the cross section line of the orthogonal plane from a back-to-back scan (**Figure 3-7**). One hundred thirty-three images (out of 208) in the testing dataset had corresponding orthogonal plane scans acquired during the biopsy procedure for this evaluation. We found orientation differences to have median [IQR] of 2.6° [3.3°]. This shows that the images in our testing dataset have a certain range of needle axis obliqueness, and more training data with a wider range could be included in future work. For real-time MRI, the model trained with 9 needle orientations was tested in real-time MRI datasets with an expanded range of needle orientations (10°–30° with respect to $B_0$). This model was trained with a single needle type, tissue type, and slice orientation (coronal) and tested for two different needle types, different tissue types, and two slice orientations (coronal and sagittal). The successful and consistent tracking results for the different real-time MRI datasets (**Table 3-4**) indicate that robust real-time tracking performance across multiple experimental conditions can be achieved by using a relatively limited training dataset. Our results show that the proposed algorithm has accurate performance in a range of different situations, and further work is needed to investigate the generalization of our algorithm to more situations.

There are limitations to this study. First, obliqueness of the needle axis with respect to the image plane could cause failure of the needle feature detection on intraprocedural prostate MRI or lead to tracking outliers on real-time *ex vivo* tissue MRI. Strategies to improve the proposed algorithm include training Mask R-CNN using images with a wider range of needle axis obliqueness, considering a stack of images encompassing the needle axis as the input to the needle detection algorithm, and to use orthogonal planes, in combination with our proposed algorithm, to systematically align image planes with the needle axis and improve the needle detection performance[65,66]. Second, the discrepancy between the needle feature on MRI and the physical needle position[55,106] was not addressed in this study. Future work will focus on extending the current algorithm with an additional step of estimating the physical needle position based on the needle feature. Third, there was a lack of pre-clinical or clinical *in vivo* real-time MRI datasets in our study, since *in vivo* real-time MRI-guided interventions are not currently performed at our institution. The needle localization or tracking performance using our proposed algorithm would need to be studied for in vivo real-time MRI with different variations of the needle feature in the future.

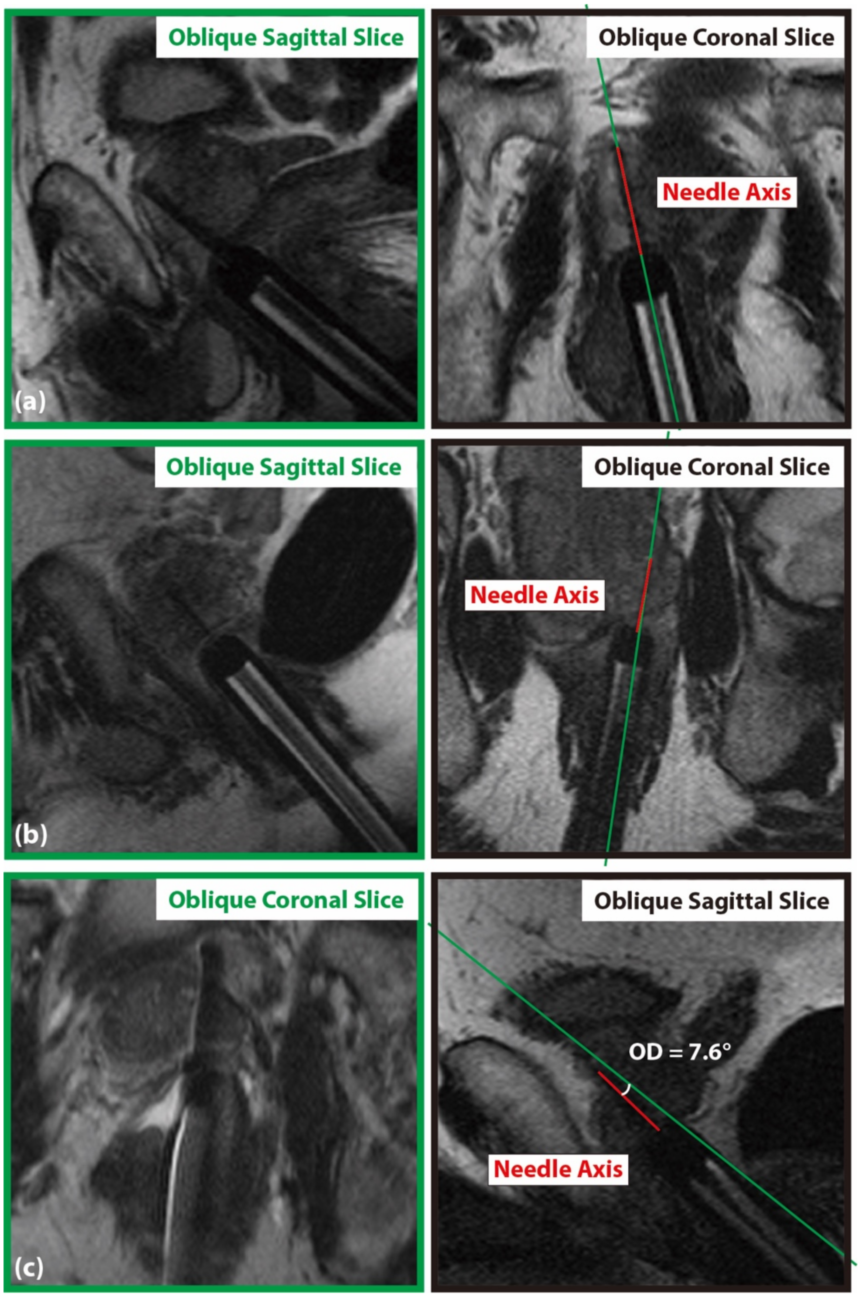

**Figure 3-7 (a) An example oblique sagittal slice (left image and green line in the right image) in the prostate MRI testing dataset, which was perfectly aligned with the center line of the needle feature (needle axis) in the corresponding orthogonal oblique coronal slice (right image). The needle feature in the left image was successfully detected by the proposed algorithm. (b) An example oblique sagittal slice in the testing dataset (left image), which was mildly oblique with respect to the needle axis in the orthogonal oblique coronal slice (right image). The orientation difference (OD) was 3.5°. The needle feature was successfully detected in the left image. (c) An example oblique coronal slice (left image) in the testing dataset, which was not only oblique but also shifted with respect to the needle axis in the orthogonal oblique sagittal slice (right image). The OD was 7.6°, which was the maximum value in the testing dataset. The proposed algorithm failed to detect the needle feature in the left image**

## 3.5 Conclusion

In summary, we have developed an automatic needle tracking algorithm based on the Mask R-CNN for MRI-guided interventions. Testing results from intra-procedural prostate MRI and *ex vivo* tissue real-time MRI datasets demonstrated real-time needle tracking (processing time ~ 75 ms/frame) with close agreement to human references (needle feature tip median dxy: 0.7–1.1 pixels). The proposed algorithm addressed a range of feature variations in MR image-based passive needle tracking and has the potential to improve intra-procedural and real-time MRI-guided interventions.

*This work has been published as:* ***Li X****, Young AS, Raman SS, Lu DS, Lee Y-H, Tsao T-C, Wu HH. Automatic Needle Tracking using Mask R-CNN for MRI-Guided Percutaneous Interventions. Int J Comput Assist Radiol Surg 2020;15(10):1673-1684.*

# Chapter 4 Physics-Driven Mask R-CNN for Physical Needle Localization in MRI-Guided Percutaneous Interventions

## 4.1 Introduction

The success of minimally invasive image-guided percutaneous procedures, such as targeted biopsy and focal ablation, depends on intra-procedural imaging to visualize tissues and devices (i.e., needles) simultaneously for guidance and confirmation [1,2]. Automatic, accurate, and rapid needle localization will be required for needle adjustment under both intra-procedural and real-time MRI guidance. Automatic needle localization based on the passive needle feature is challenged by variations of the needle susceptibility-induced signal void feature due to different situations[52,110]. Deep learning-based techniques show promise for accurate detection and segmentation of the needle feature on MRI[53,54,119,129], however a major limitation is that the discrepancy between the needle feature and the underlying physical needle position has not been addressed.

The susceptibility difference between the needle and surrounding tissue causes magnetic field perturbation and MR signal dephasing [110]. With MR-compatible needle materials, such as titanium alloys, the needle susceptibility and geometry usually lead to a long tubular signal void feature on MR images. This needle signal void feature can have an irregular shape at the tip and the axis can be shifted from the physical needle axis. Therefore, even if the image plane is perfectly aligned with needle, there may be discrepancies between the needle feature and physical needle. Previous studies [55,130] have reported that this discrepancy can reach 5-10 mm and depends on the MRI sequence type and parameters, the needle material, and the needle's orientation relative to the $B_0$ field. For reference, clinically relevant tumors for image-guided interventions may have a diameter of 5-10 mm[56]. Therefore, only localizing the needle feature to monitor the physical needle position during the procedure may cause substantial errors in needle targeting.

There are some approaches that have potential to overcome this limitation. One approach is to reduce or correct the distortion of the signal void feature vs. the physical object with multispectral MR imaging. For example, slice-encoding metal artifact correction (SEMAC) can minimize the average needle tip error (~0.4 mm) with improved time efficiency using compressed sensing (CS) reconstruction[57]. However, the combined acquisition and reconstruction time of CS-SEMAC (~30 sec) is still not appropriate for immediate updates of the needle position for feedback during procedures[131]. Another approach is to reconstruct the precise physical object shape by forming an inverse problem based on a set of acquired MRI signals. The forward modeling of the needle susceptibility-induced signal void has been reported for different sequence parameters and needle geometry[52,132]. However, due to the ill-posed nature of the inversion problem, multi-orientation sampling and iterative computation similar to strategies for quantitative susceptibility mapping may be required, which are not practical for time-sensitive interventional procedures[133].

Supervised deep learning using convolutional neural networks (CNNs)is a potential approach to rapidly and accurately calculate solutions to ill-posed inversion problems involving magnetic susceptibility. For example, DeepQSM [58] and QSMNet [59] both use pixel-level semantic models to solve ill-posed field-to-source inversion problems and reconstruct quantitative tissue susceptibility maps from single-orientation MRI phase data with rapid inference time. Hence physical needle localization based on the needle feature may potentially be achieved using a deep learning-based approach. However, pixel-level semantic methods could be sensitive to false detection of small objects (e.g., a needle segment in a full field-of-view image). Therefore, a deep learning-based framework using an instance-level method such as Mask R-CNN can have advantages for physical needle localization.

In MRI-guided interventions, single-slice and multi-slice imaging are used to inform different aspects of the procedure. Imaging plane orientation selection for intra-procedural single-slice and multi-slice imaging is typically performed using information from a multi-slice planning scan in order to ensure that the needle feature is aligned with the slices with minimal through-plane deviation. Single-slice MRI is usually performed to achieve dynamic needle guidance with fast imaging speed [5,34]. However, through-plane misalignment between the image plane and needle could lower physical needle localization accuracy using single-slice MRI. Sequential multi-slice and orthogonal plane acquisitions have the potential to assist intuitive interpretation of this misalignment by physicians [6,7]. In particular, 3-parallel-slice imaging is a recommended choice from previous studies[6,134] and our clinical interventional radiologist colleagues.

The main objective of this study was to develop and test a deep learning framework using Mask R-CNN to automatically and rapidly localize the physical needle position from the passive needle features on MRI. This study first established a single-slice physical needle localization network based on Mask R-CNN by assuming the physical needle was perfectly aligned with the MRI scan plane and focused on addressing in-plane discrepancies between the needle feature and the physical needle. In addition, this study established a 3-slice physical needle localization network based on Mask R-CNN to estimate the physical needle position in the in-plane and through-plane dimensions for 3D localization.

## 4.2 Methods

### 4.2.1 Overview of the Physical Needle Localization Framework

We developed a new needle localization framework consisting of two Mask R-CNN stages (**Figure 4-1**), with the software implementation based on Keras and Tensorflow [124]. For the first stage, we used a "needle feature" Mask R-CNN that we previously trained to detect and segment the needle feature on the input MR image (Chapter 3) [129]. Based on the results of the first stage, the image was automatically cropped to a patch centered on the needle feature. For the second stage, we trained two separate "physical needle" Mask R-CNN models: 1. A single-slice physical needle Mask R-CNN that takes a needle feature patch from a single slice as input to localize the in-plane 2D physical needle tip and axis (**Figure 4-1b**), and 2. A 3-slice physical needle Mask R-CNN to localize 3D physical needle position (in-plane and through-plane) on three adjacent and parallel slices (**Figure 4-1c**). Single-slice and multi-slice MRI simulations and experiments were performed to train, validate, and test the proposed framework for physical needle localization. *Ex vivo* tissue phantom data were acquired for testing, since the tissue features resemble features on *in vivo* MRI and the phantom setup allowed us to measure the physical needle position under controlled conditions to serve as the reference.

### 4.2.2 MRI-Guided Needle Insertion Experiments

We used a golden-angle (GA) ordered radial spoiled gradient-echo (GRE) sequence [121] for real-time 3T MRI-guided needle (20 gauge, 15 cm, Cook Medical) insertion in phantoms. Different imaging parameters (echo time [TE] = 1.9 ms, readout bandwidth [BW] = 888 Hz/pixel; TE = 3 ms, BW = 888 Hz/pixel; TE = 2.8 ms, BW = 300 Hz/pixel) and needle orientations were used to create variations in the passive needle feature on MRI. To achieve sufficient image quality and signal-to-noise ratio (SNR) for needle visualization, a temporal resolution of around 1 sec/frame was used for real-time MRI. The imaging parameters are listed in **Table 4-1**. Images were reconstructed using non-Cartesian conjugate gradient sensitivity encoding (SENSE) with reconstruction window size of 200 radial spokes[95,121].

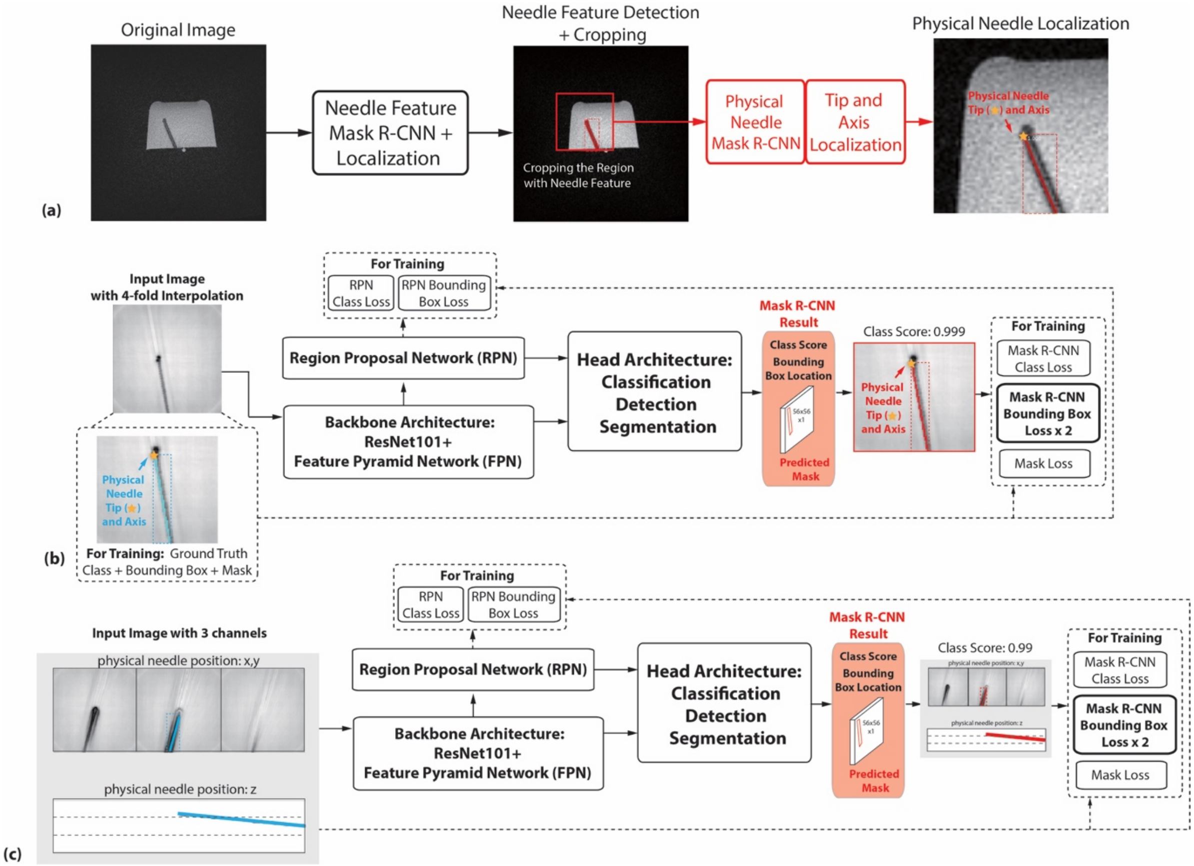

**Figure 4-1 (a) The overall physical needle localization framework consisted of two stages of Mask R-CNN. The first "needle feature" Mask R-CNN detected and segmented the needle feature on an MR image with field-of-view (FOV) of 300x300 mm$^2$. Next, the single-slice image or 3-slice images with needle features were automatically cropped to a FOV of 75x75 mm$^2$ centered at the detected needle feature tip and used as the input to the second "physical needle" Mask R-CNN, with options (b) and (c), which detected the 2D or 3D physical needle tip and axis. (b) The single-slice physical needle Mask R-CNN was trained using physics-based simulated data of single slice MRI. Ground truth labels for training were structured as a 2D bounding box with corners that defined the physical needle tip location and axis orientation. Dashed lines indicate data labels and computation steps for training. (c) The 3-slice physical needle Mask R-CNN was trained using physics-based simulated data of 3 adjacent parallel slices of MRI. Ground truth labels for training were structured as a 3D bounding box with corners that defined the physical needle tip location and axis orientation.**

**Table** 4-1 **Imaging parameters for real-time radial gradient-echo (GRE) MRI of the gel phantom and *ex vivo* tissue phantom at 3T. Three combinations of repetition time (TR), echo time (TE), and bandwidth (BW) were used to acquire images with different tissue contrast and needle signal void feature. Similar imaging parameters were used to generate simulated images that form the network training dataset. 3-parallel-slice inputs used the same imaging parameters, but with temporal resolution of 2.4-3.6 sec/image to accommodate the interleaved acquisition of 3 slices.**

| **Real-Time Radial GRE 3T MRI of the Gel and *Ex vivo* Tissue Phantoms** | | | |
|---|---|---|---|
| **TR, TE, BW** | 4.16 ms, 1.9 ms,<br>888 Hz/pixel | 5.26 ms, 3 ms,<br>888 Hz/pixel | 6.3 ms, 2.8 ms,<br>300 Hz/pixel |
| **Field of view** | 300 mm x 300 mm | **Flip angle** | 12° |
| **Matrix size** | 256 x 256 | **Dynamic temporal resolution (reconstruction window length)** | 0.8-1.2 sec / image<br>(200 radial spokes) |
| **Slice thickness** | 5 mm | **Orientation** | Oblique coronal |

We performed needle insertion experiments in gel phantoms and *ex vivo* tissue phantoms. The *ex vivo* tissue (pork shoulder or beef chuck steak) was submerged underneath gelatin to create a flat surface on the top (**Figure 4-2a**). In gel and *ex vivo* tissue phantoms, an MRI-visible fiducial marker (MR-SPOT, Beekley Medical, Connecticut, USA) was affixed to the surface to define the needle entry point. To directly control and confirm the physical needle orientation and insertion depth during experiments, we used an MRI-compatible master-slave needle actuator system (**Figure 4-2b**) [12]. We defined the orientation of the needle in terms of its rotation angle (θ) in one plane and tilting angle (α) in the orthogonal plane (**Figure 4-2c**). A linear guide on the actuator ensured a straight needle insertion path and a fixed length of the needle (50 mm) was inserted so that the physical needle tip can be in 2D image coordinates based on the position of the fiducial marker. These measurements were taken as the references of the physical needle tip position and axis orientation (**Figure 4-2e-f**) for single-slice physical needle Mask R-CNN. The range of needle axis orientation is reported in **Table 4-2**.

**Table 4-2 Physics-based simulated datasets used for training and validation of single-slice physical needle Mask R-CNN for (top). Datasets used for fine-tuning and testing of the overall physical needle localization framework with two Mask R-CNN stages (bottom). θ: needle rotation angle. α: needle tilting angle. N/A: not applicable. *Data augmentation included rescaling, translation, and additive Gaussian noise.**

| **Simulated Datasets for Training and Validation of the Single-Slice Physical Needle Localization Mask R-CNN Model** | | | | | | | |
|---|---|---|---|---|---|---|---|
| | Data size (images) | | Key imaging parameters | | Needle orientation | | |
| | Original | After 5-fold augmentation* | TE | Bandwidth | θ | α | Step |
| **Training dataset** | 741 | 3705 | 1.9 ms<br>3 ms<br>2.8 ms | 888 Hz/pixel<br>888 Hz/pixel<br>300 Hz/pixel | -30° to 30° | -90° to 0° | 5° |
| **Validation dataset 1** | 4068 | 20340 | 1.9 ms<br>3 ms<br>2.8 ms | 888 Hz/pixel<br>888 Hz/pixel<br>300 Hz/pixel | -30° to 30° | -90° to 0° | 2° |
| **Validation dataset 2** | 2852 | 14260 | 2.5 ms<br>3.7 ms | 888 Hz/pixel<br>300 Hz/pixel | -30° to 30° | -90° to 0° | 2° |
| **Datasets for Fine-Tuning and Testing of the Two-Stage Framework using Single-Slice Physical Needle Mask R-CNN** | | | | | | | |
| | Data size (images) | | Key imaging parameters | | Needle orientation | | |
| | Original | After 5-fold augmentation* | TE | Bandwidth | θ | α | Step |
| **Fine-tuning dataset** | 741 | 3705 | 1.9 ms<br>3 ms<br>2.8 ms | 888 Hz/pixel<br>888 Hz/pixel<br>300 Hz/pixel | -30° to 30° | -90° to 0° | 5° |
| **Gel phantom testing dataset** | 58 | N/A | 1.9 ms<br>3 ms<br>2.8 ms | 888 Hz/pixel<br>888 Hz/pixel<br>300 Hz/pixel | -36° to 29° | -31° to -2° | N/A |
| ***Ex vivo* tissue phantom testing dataset** | 186 | N/A | 1.9 ms<br>3 ms<br>2.8 ms | 888 Hz/pixel<br>888 Hz/pixel<br>300 Hz/pixel | -34° to 41° | -92° to -7° | N/A |

In addition, a similar set-up was applied to acquire the reference physical needle position for 3-slice physical needle Mask R-CNN. One smaller MRI-visible fiducial marker was affixed on the surface to mark the needle entry point and another longer fiducial marker was attached on the needle shaft. 3D high-resolution $T_1$-weighted gradient echo images with isotropic voxel size of 0.6 mm were acquired to measure the physical needle position based on the pre-determined position of the entry point relative to the small fiducials and a fixed needle insertion length (60 mm) (**Figure 4-3b-d**). The reference physical needle tip positions were measured in the RAS (right/left, anterior/posterior, superior/inferior) coordinate system using open-source software (3D Slicer)[42], The range of needle axis orientation is reported in **Table 4-3**.

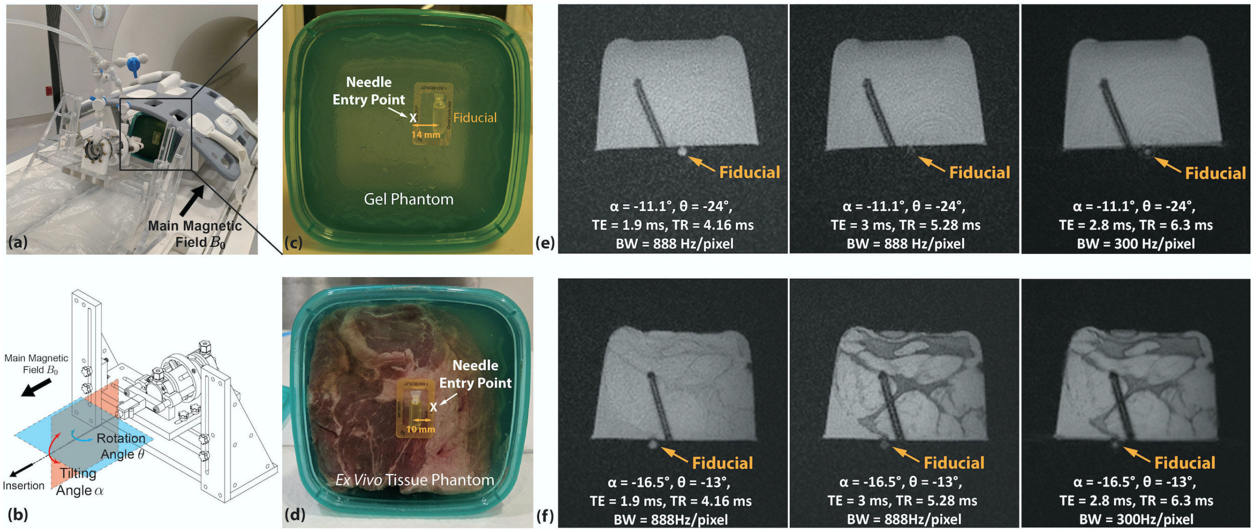

**Figure 4-2 (a) In phantom MRI experiments, the needle orientation was varied in terms of its rotation (θ) and tilting angle (α) relative to $B_0$. A needle actuator system was used to insert the needle into a gel phantom by 50 mm without bending. The ranges of α and θ are reported in Table 2. (b) Experimental setup in the 3T MRI scanner. (c)-(d) An MRI-visible fiducial marker was affixed to the phantom to measure the physical needle position in the gel and *ex vivo* tissue phantoms. (e) Example gel phantom MR images (α=-11.1° and θ=-24°) with three different sets of imaging parameters and (f) example *ex vivo* tissue phantom MR images (α=-16.5° and θ=-13°) with three different sets of imaging parameters. All phantom MR images were reconstructed using conjugate gradient SENSE. TE: echo time. TR: repetition time. BW: readout bandwidth.**

**Table 4-3 Physics-based simulation dataset for training of 3-slice physical needle Mask R-CNN and *ex vivo* tissue datasets used for testing the overall physical needle localization framework. θ: needle rotation angle. $\alpha_1$: needle tilting angle relative to $B_0$ field. $\alpha_2$: inner tilting angle of needle relative to the center image slice. h: pivot point. N/A: not applicable. *Data augmentation included rescaling, translation, and additive Gaussian noise.**

| | Data size (images) | | Key imaging parameters | | Needle orientation | | | | |
|---|---|---|---|---|---|---|---|---|---|
| | Original | After 5-fold augmentation* | TE | Bandwidth | θ | $\alpha_1$ | $\alpha_2$ | h | Step |
| **Training dataset** | 2160 | 10800 | 1.9 ms<br>3 ms<br>2.8 ms | 888 Hz/pixel<br>888 Hz/pixel<br>300 Hz/pixel | -30° to 30° | -90° to 0° | 6° to -6° | -5 mm to 5 mm | 5° |
| **Testing dataset** | 150 | N/A | 1.9 ms<br>3 ms<br>2.8 ms | 888 Hz/pixel<br>888 Hz/pixel<br>300 Hz/pixel | -22° to 32° | -72° to -15° | 7° to -5.5° | -3.8 mm to 5 mm | N/A |

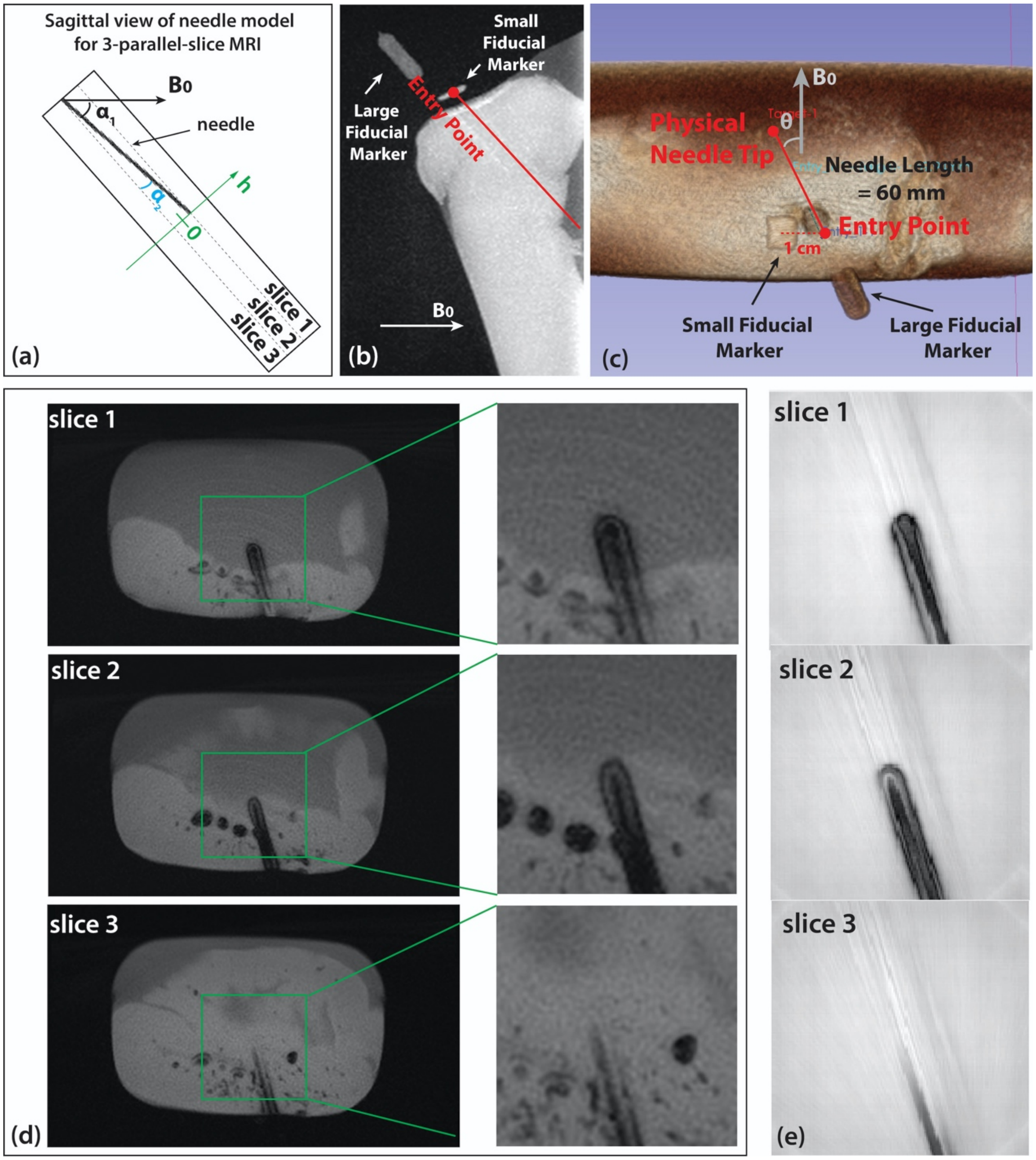

**Figure 4-3 (a) An example diagram of sagittal view of an inserted needle misaligned with 3 parallel oblique coronal imaging planes. Needle tilting angle ($\alpha_1$) is -49.1°, inner tilting angle ($\alpha_2$) is 5.5° and pivot point (h) is 2.5 mm. (b) maximum intensity projection of high-resolution 3D MRI in sagittal view displayed the fiducial markers used to locate the needle tilting angle relative to the main magnetic field $B_0$ and entry point. (c) 3D rendered model of the phantom and the fiducial markers in a 3D environment. Physical needle tip is determined based on fixed needle insertion length (6 cm) and entry point that was marked at the centerline of the small fiducial marker, which was 1 cm from its center point. Needle rotation angle (θ) is -17.9°. (d) Corresponding 3-parallel-slice MR images in the actual needle insertion experiment. (e) Simulated passive needle features showed similar feature pattern and distribution on different imaging planes.**

### 4.2.3 Needle Susceptibility Simulations and Calibration

Training the physical needle Mask R-CNN requires a substantial amount of data with reliable reference needle position information. However, collecting data from the MRI experiments described in the previous section is expensive, time-consuming, and subject to experimental uncertainties. Therefore, we performed MRI physics-based simulations of the needle susceptibility effects to generate a large set of training images that accurately depict the needle feature with respect to actual intra-procedural MRI.

We implemented the Fourier-based off-resonance artifact simulation in the steady state (FORECAST) method to calculate the susceptibility effects in steady-state GRE MRI[52]. The field inhomogeneity or field shift $\Delta B_0(x, y, z)$ was calculated as a function of different needle orientations and needle materials with different magnetic resonance properties using a first order perturbation approach to Maxwell's equations, combined with the Fourier transformation technique[135]. In the original FORECAST method, a thin slice with the desired field of view (FOV) and slice thickness was modeled in 3D space, with the third dimension of $\Delta B_0$ set to be parallel to $B_0$, which does not capture the tilting angle of the needle. To simulate the needle with a tilting angle, which is a more realistic scenario in interventional procedures, we created an expanded 3D model (**Figure 4-4**). Specifically, $\Delta B_0(x, y, z)$ was calculated and re-sliced to an oblique volume parallel to the needle with certain excitation slice or slab thickness. A linear interpolation step was performed to assign the $\Delta B_0$ to each pixel of the model with the original pixel dimensions. In addition, a non-uniform fast Fourier transform (NUFFT) was applied for the GA ordered radial sampling trajectory during the simulations[136]. The overall k-space signal model of the needle susceptibility-induced effects on the discrete isochromatic grid with proton density $\rho'(x,\ y,\ z)$ was:

**Equation 4-1**

$$s(k_x, k_y, k_z) = \sum_x \sum_y \sum_z \rho'(x,\ y,\ z) e^{-i2\pi\gamma \Delta B_0(x,y,z)t' - k_z t'}\ e^{-\frac{t'}{T_2}} e^{-i2\pi(k_x x + k_y y)}$$

where $\gamma$ is the gyromagnetic ratio and t’ is the time after RF excitation. Note that the $T_2$* of the signal was decomposed into $T_2$ (e.g., 50 ms for muscle) and the field inhomogeneity caused by the needle susceptibility effects. Finally, an inverse NUFFT was applied to the simulated k-space data to reconstruct the image, which contains the needle signal void feature.

For these simulations, we assumed that the needle material is stiff enough[137] and there was no deflection close to the tip. Therefore, we modeled the needle as a cylindrical rod with diameter of 0.9 mm (20 gauge) at different rotation (θ) and tilting (α) angles in 3D space similar to the actual experimental setup (see previous section). The range of θ (-30° to 30°) and α (0° to -90°) of the needle was set according to actual reports of needle placement in abdominal percutaneous interventions by other groups[138-140] and our clinical colleagues.

To ensure that the simulations matched the conditions of the needle used in experiments, we used actual experimental data with different needle orientations and imaging parameters to calibrate the susceptibility value of the needle material. The Euclidean distance between the physical needle tip and the needle feature tip (dxy in mm, **Figure 4-5**) was calculated for simulated data and gel phantom experimental data. The susceptibility value that achieved the minimum average dxy was identified and used in simulations to generate training data.

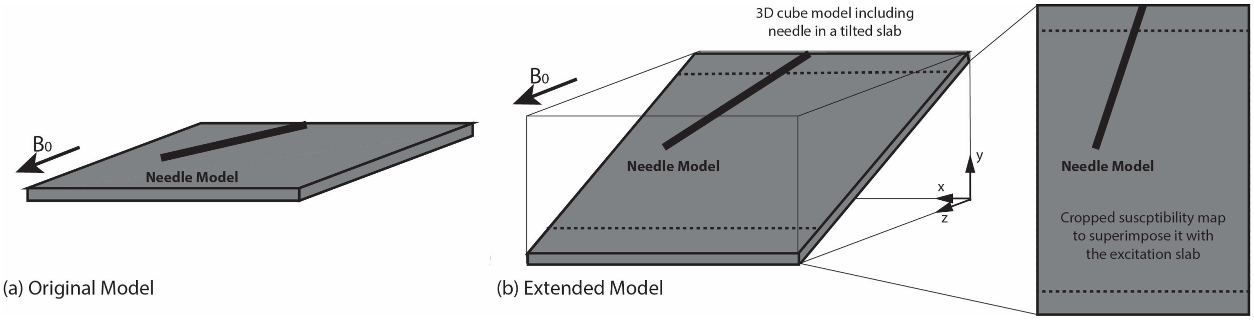

**Figure 4-4 (a) In the original FORECAST method, the susceptibility map can only be calculated for an imaging slice/slab that has one direction aligned with the main magnetic field $B_0$. (b) To calculate the susceptibility map for a needle model that is tilted with respect to $B_0$, we created an expanded 3D model. The susceptibility map in this 3D model was interpolated to the coordinates and model elements in the excited imaging slice/slab, which contained the needle with a certain tilting angle. The gray plan represents an excitation model with single slice or a thin slab of multiple slices. At the end, the susceptibility map was cropped to match the size of the imaging slice/slab.**

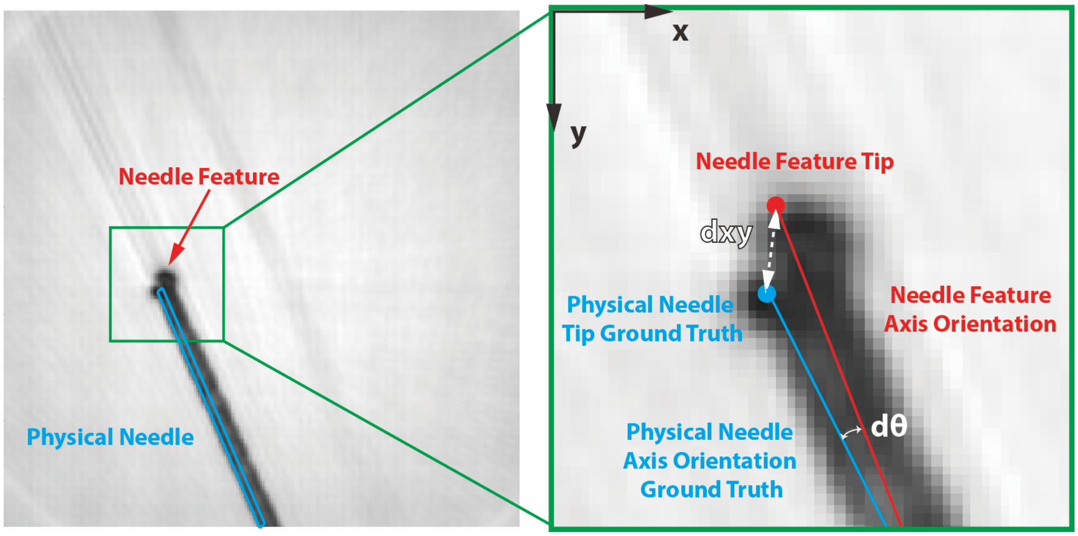

**Figure 4-5 The discrepancy between the needle feature position and the actual physical needle position was quantified in terms of the Euclidean distance between the feature tip and the physical needle tip (dxy), and the absolute difference between the feature axis and the physical needle axis orientation (dθ), both in image coordinates at 2D space. The accuracy of physical needle localization using the first proposed framework with single-slice MRI was also quantified in terms of dxy and dθ.**

### 4.2.4 Single-Slice Physical Needle Mask R-CNN Training and Validation

The input to the single-slice physical needle Mask R-CNN is an image patch centered on the needle feature and surrounding tissue, obtained from the needle feature Mask R-CNN output. The training dataset for the single-slice physical needle Mask R-CNN consisted of simulated images with the same size as the expected input patches (75x75 $mm^2$ field of view with 256x256 matrix size) and the needle feature tip in the center of the patch (**Figure 4-1**). The input 2D gray-scale image patches were normalized and stacked into 3 color channels. We used the output bounding box corners to define the physical needle tip (e.g., at the top left corner) and axis (e.g., the line connecting the top left and bottom right corners) since the diameter of the true needle is less than the pixel size. Since the needle tip location and axis orientation were more important than the needle segmentation mask in the physical needle Mask R-CNN stage, we weighted the bounding box loss to twice that of the losses in other branches during training.

We first trained and validated the single-slice physical needle Mask R-CNN for needle localization using simulated data. A set of 741 simulated images with the same parameters as phantom experiments (θ from -30° to 30°, and α from 0° to -90°) was created for training. Five-fold data augmentation was performed by rescaling, translation, and adding Gaussian noise to form a training dataset with 3705 images. The training hyperparameters were based on our previous work on needle feature segmentation [129] and the number of epochs (480 epochs) was increased to accommodate the larger data size. Next, we simulated 4068 images with the same imaging parameters, but different θ and α within the same range as the training data to validate the network performance for different needle orientations. Finally, we simulated 2852 images with different imaging parameters (TE = 2.5 ms, BW = 888 Hz/pixel; TE = 3.7 ms, BW = 300 Hz/pixel) and different needle orientations to investigate the performance of the model for new imaging parameters. Similar data augmentation as training was adopted to form two validation datasets (v1: 20340 images, v2: 14260 images). The Euclidean distance between the estimated physical needle tip position and the ground truth (dxy in mm) was calculated based on image coordinates (**Figure 4-5**). The absolute difference between the needle axis orientations (dθ in degrees) was also computed to evaluate the localization accuracy. Characteristics of the various datasets for training and validation of the physical needle Mask R-CNN are reported in **Table 4-2.**

### 4.2.5 Single-Slice Physical Needle Mask R-CNN Testing with Gel Phantom Data

After validation using simulated images, we combined the trained single-slice physical needle Mask R-CNN model with the needle feature Mask R-CNN to form a two-stage framework (**Figure 4-1**) and tested the performance in actual experimental phantom images. The physical needle tip and axis orientation estimation results from the two-stage framework were compared to the measured reference physical needle position to evaluate the accuracy in terms of dxy and dθ. The testing dataset included 58 actual gel phantom MR images containing the needle feature (**Table 4-2**).

### 4.2.6 Single-Slice Physical Needle Mask R-CNN Fine-Tuning

Interventional MR images acquired during actual procedural guidance have more complex backgrounds compared to the simulated images. In addition, certain types of tissue with off-resonance effects (e.g., fat) may also generate signal voids (e.g., fat-water signal cancellation) that occlude the needle feature. These effects might degrade the accuracy of our framework. Therefore, after training with simulated data as previously described, we performed fine-tuning of the physical needle Mask R-CNN by using an additional training dataset with enriched variations of the background. To do this, we acquired MR images of *ex vivo* tissue in different slices without a needle. Patches were randomly cropped from these *ex vivo* tissue images and superimposed with the simulated needle images (741 images) (**Figure 4-6**), followed by similar data augmentation to increase the size of the fine-tuning dataset (3705 images) (**Table 4-2**).

### 4.2.7 Single-Slice Physical Needle Mask R-CNN Testing with *Ex Vivo* Tissue Phantom Data

We tested the needle localization accuracy of the proposed first two-stage framework using *ex vivo* tissue phantoms, which have realistic image characteristics that are representative of interventional MRI. 186 images were collected from experiments to form a testing dataset with 62 different needle orientations. This dataset had a larger range of needle tilting angles (α from -92° to -7°) than the gel phantom dataset (-31° to -2°) to enable a more thorough test of the framework. We compared the accuracy of physical needle localization using the physical needle Mask R-CNN models without and with fine-tuning. The same error metrics were used (dxy and dθ).

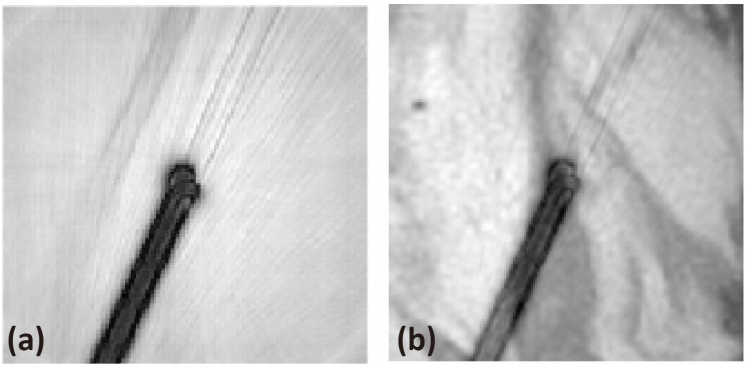

**Figure 4-6 (a) Two example training images generated from MR physics simulation. (b) Two example images for physical needle Mask R-CNN model fine-tuning, which were created by superimposing the simulated needle on a patch of tissue background from *ex vivo* MRI.**

### 4.2.8 Three-Slice Physical Needle Mask R-CNN Training

In addition to the single-slice strategy, we also developed a Mask R-CNN model for 3-slice physical needle localization. The bounding box output was increased from 4 dimensions to 6 dimensions to capture the 3D coordinates of the physical needle's two ends (tip and entry point). The input to the new network was acquired in the same approach as the single-slice network, except that it contains three image patches, including needle features from three adjacent parallel slices. The three patches were normalized and stacked into three color channels of the network input. Then we applied the same simulation method to generate the training dataset. The thickness of the slab in the 3D model was expanded from 5 mm to 15 mm to emulate three parallel imaging slices without any gap. Misalignment between the needle model and 3D acquisition slab was characterized by two additional geometric parameters: inner tilting angle ($\alpha_2$) and pivot point (h) within the slab (**Figure 4-3a**).

To quantify the range of the additional parameters in the simulation step, similar needle obliqueness analysis as in Chapter 3 were performed by using clinical MRI-guided prostate biopsy datasets (326 images from 125 cases)[129]. We found that the misalignment of the image plane with the needle feature based on orthogonal images had a median of 3.1° with IQR of 2.6°[7]. Around 92% of the cases had misalignment between needle feature and imaging plane of <6°. The passive needle features were contained within 1 to 3 slices for each imaging dataset based on the relative position between the imaging plane and needle feature axis. Based on these typical ranges of needle angles, we can assume that the tilted needle feature would be contained within 3 parallel slices. Therefore, we considered 35 representative parameter combinations of $\alpha_2$ = [-6°, -4°, -2°, 0°, 2°, 4°, 6°] and h = [5, 2.5, 0, -2.5, -5] mm. The physical needle reference was defined with a 3D bounding box and the third dimension coordinate can be visualized from the side view of the 3D acquisition slab.

We trained the 3-slice physical needle Mask R-CNN for needle localization using a set of 2160 simulated images with the same parameters as phantom experiments ($\theta$ from -30° to 30°, and $\alpha_1$ from 0° to -90°). 10 random choices of different combinations of $\alpha_2$ and h ware selected for each imaging plane orientation. *Ex vivo* tissue images superimposed with these simulation images and 5-fold data augmentation was performed to form a training dataset with 10800 images. The epoch number was increased to 480 to accommodate the larger training dataset. The network parameters were initialized with random weights instead of using any pretrained single-slice physical needle Mask R-CNN model because of the structural differences of the 3-slice network and different feature encoding of channel-wise information from input images.

### 4.2.9 Three-Slice Physical Needle Mask R-CNN Testing

We tested the needle localization accuracy of the proposed two-stage framework in *ex vivo* tissue phantoms using 3-parallel-slice MRI. 150 images were collected from experiments to form a testing dataset with 25 different needle orientations (**Table 4-3**). At each needle position, three sets of imaging parameters with two different $\alpha_2$ were used to acquire the imaging dataset for testing. We compared the accuracy of physical needle localization using the single-slice physical needle Mask R-CNN and 3-slice physical needle Mask R-CNN. One of the 3-parallel-slice images with the complete needle feature was selected as the input for the single-slice physical needle Mask R-CNN. The error metrics were all measured in 3D environment (tip localization error: dxyz; 3D orientation difference: dϕ). dxyz was calculated as the Euclidean distance between the estimated and reference physical needle tip positions. dϕ was calculated as the orientation difference (angular separation) between the estimated and reference physical needle axes in 3D space.

### 4.2.10 Physical Needle Localization Error Analysis

For tip localization error (dxy or dxyz), we considered a 2.5-mm threshold since clinically relevant tumors for interventions may have diameters of 5-10 mm[56]. In addition, the needle tip and axis orientation discrepancy between the needle feature and physical needle were manually measured by a trained researcher to serve as a baseline to assess the improvement using the proposed Mask R-CNN framework. The physical needle localization results using different models and the error from the needle feature discrepancy were first compared using a non-parametric analysis of variance (ANOVA) (i.e., Kruskal-Wallis test). If significant differences were detected by the Kruskal-Wallis test, the medians of the results were compared in a pair-wise fashion using the non-parametric Wilcox signed rank test. In addition, the variances of the results were compared using the Brown-Forsythe test. We considered differences with $p < 0.05$ to be significant.

## 4.3 Results

### 4.3.1 Needle Susceptibility Calibration

Simulated MR images that contained the needle feature with different rotation and tilting angles were compared with the MR images from actual MRI-guided needle insertion experiments (**Figure. 4-7**). The characteristics of the needle feature from simulations closely matched the needle feature on experimental images, with one difference being the additional noise seen on experimental images. The physical needle position in the coordinates of the experimental MR images were determined based on the fiducial marker position. The spatial relationship (discrepancy) between the physical needle and the needle feature were almost identical for simulated and experimental images. During the calibration process, we found that a needle susceptibility value of 190 ppm (corresponding to titanium) achieved close agreement between the simulations and experiments for 7 different rotation angles (**Figure 4-7**). Therefore, we used this calibrated susceptibility value for subsequent simulations. Example 3-parallel-slice simulation images using this susceptibility value also generated needle features that are in close agreement with the MR images from actual experiments (**Figure 4-3d-e**).

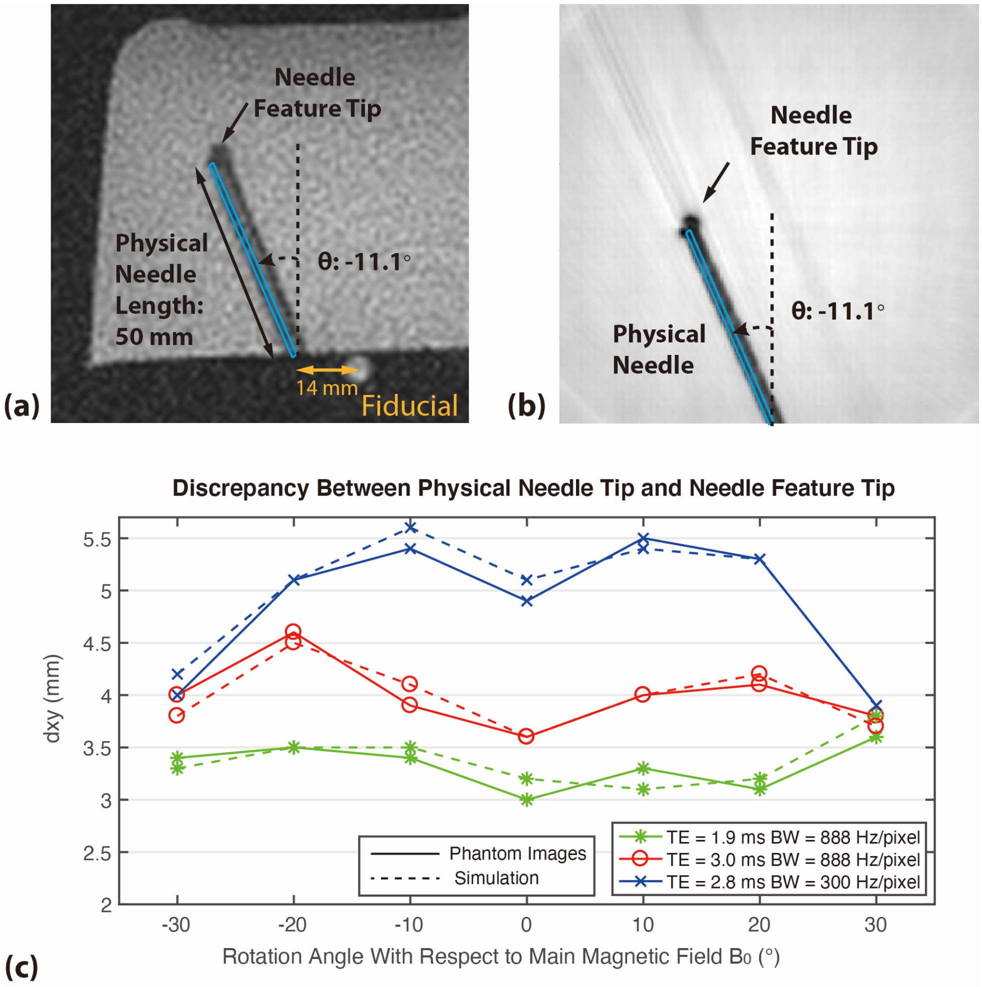

**Figure 4-7 (a) An example real-time 3T single slice MR image with needle tilting angle (α) of 11.1° and rotation angle (θ) of -24° with respect to $B_0$, TE = 1.9 ms, and bandwidth (BW) = 888 Hz/pixel. (b) Example simulated image using a 300x300x5 $mm^3$ field-of-view (FOV) with 1024x1024x17 model elements, 256 radial readout points, and a 20-gauge needle with the same orientation in (a). The images were reconstructed using non-uniform fast Fourier transform (NUFFT) and then cropped to a FOV of 75x75 $mm^2$ with image matrix size of 64x64. (c) Calibration results of needle susceptibility (190 ppm) showing dxy for seven different needle rotation angles.**

### 4.3.2 Single-Slice Physical Needle Mask R-CNN Training and Validation

We trained the single-slice physical needle Mask R-CNN using a batch size of 8 on two graphics cards (NVIDIA GTX 1080Ti). Generation of the simulated data for training took 10 hours. Training with simulated data took about 12 hours and the fine-tuning step (simulated needle features combined with tissue image patches) took another 12 hours. Validation was performed with additional simulated data for the network model without fine-tuning. Example results of physical needle localization for simulated images in both validation datasets are shown in **Figure 4-8**. Results for augmented images with different needle orientations and noise levels showed that the physical needle Mask R-CNN achieved needle localization close to the references. Overall, the physical needle Mask R-CNN achieved median dxy of 0.29 mm and 0.29 mm, and dθ of 0.34° and 0.35°, for validation datasets 1 and 2, respectively (**Table 4-4**). In addition, 68.3% and 81.5% of dxy were lower than the simulation model element resolution (0.3 mm), and 94.8% and 92.8% of dθ were lower than 1°, for validation datasets 1 and 2, respectively. Mask R-CNN achieved 100% physical needle detection rate in both validation datasets.

### 4.3.3 Single-Slice Physical Needle Mask R-CNN Testing with Gel Phantom Data

Representative results of physical needle localization using the Mask R-CNN model without fine-tuning for gel phantom data are shown in **Figure 4-9a-b**. The processing time of the whole framework was about 200 ms per image, which is suitable for real-time interventional MRI applications. The overall results from the gel phantom testing dataset are shown in **Table 4-4**. Our proposed framework successfully localized the physical needle position on the images with different sequence parameters, achieving median dxy and dθ of 0.79 mm and 0.76°, respectively. Around 80% of the physical needle tip error and 65% of the physical needle axis orientation error were less than the pixel size (1.17 mm) and 1°, respectively.

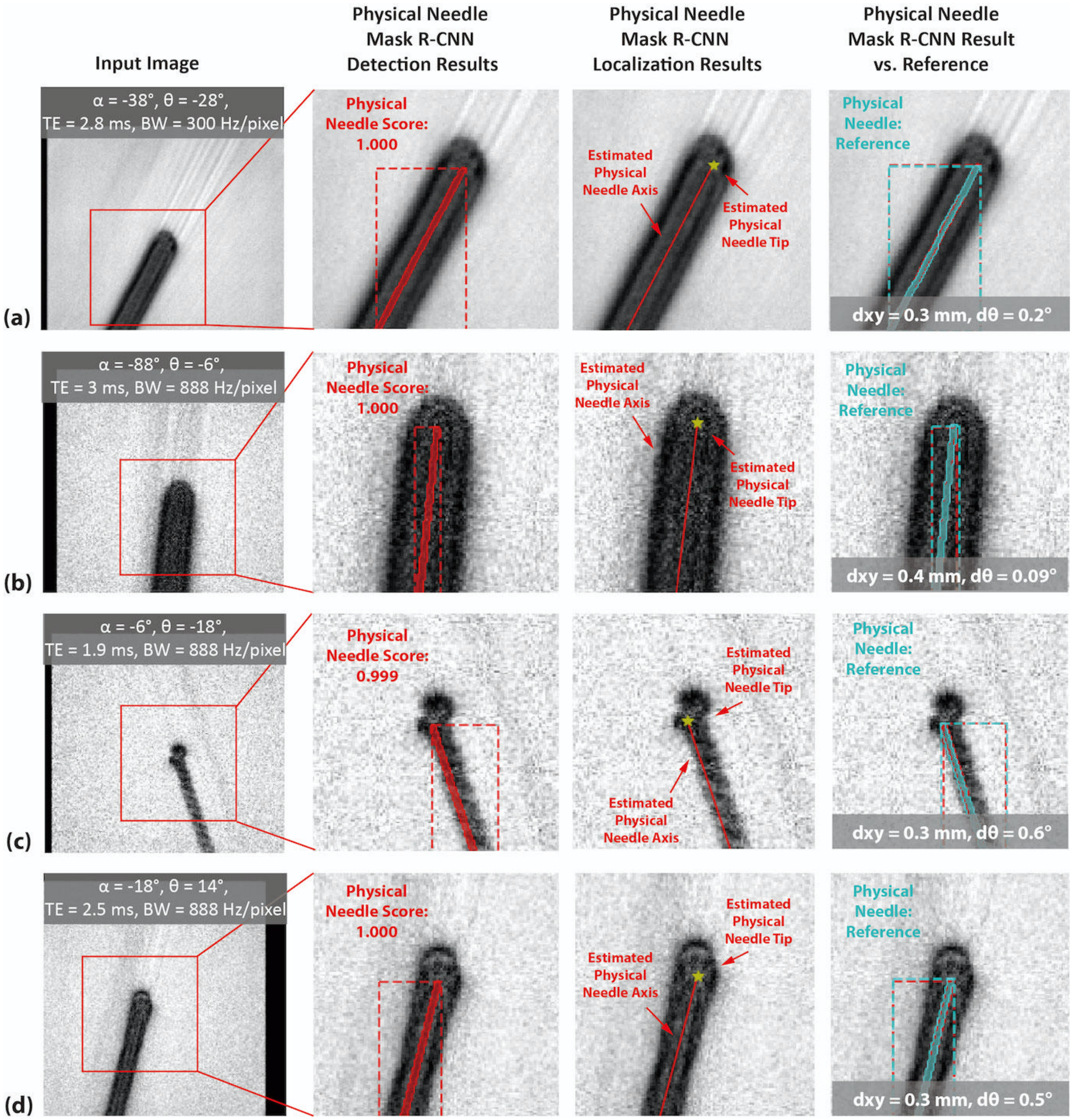

**Figure 4-8 (a-c) Example single-slice physical needle Mask R-CNN localization results in an augmented input image from validation dataset 1 with needle tilting (α) and rotation (θ) angles that were not in the training dataset. (d) Example single-slice physical needle Mask R-CNN localization results in an augmented input image from validation dataset 2 with needle α and θ that were not in the training dataset. Mask R-CNN results are shown in red and the references (cross-section of the needle models used in the simulations) are in blue. TE: echo time. BW: readout bandwidth.**

### 4.3.4 Single-Slice Physical Needle Mask R-CNN Testing with *Ex Vivo* Tissue Phantom Data

Representative results for physical needle localization in *ex vivo* tissue testing data using the fine-tuned single-slice Mask R-CNN model are shown in **Figure 4-9c-e**. These examples showed not only the needle localization accuracy of the framework, but also the improvement of the fine-tuned single-slice physical needle Mask R-CNN model compared to the non-fine-tuned model. **Figure 4-9c** shows an example where the fine-tuned model successfully detected the physical needle, but the model without fine-tuning failed to detect the needle (**Figure 4-10**). **Figure 4-9b** shows an example with accurate physical needle tip localization and axis orientation estimation using the fine-tuned model. In contrast, the tip localization results for this case had large errors (dxy = 5.76 mm) using the model without fine-tuning (**Figure 4-10**).

The overall testing results for the two-stage framework using the single-slice physical needle Mask R-CNN models without and with fine-tuning are shown in **Table 4-4**. The framework using the non-fine-tuned model achieved median dxy and dθ of 0.94 mm and 0.64°, respectively, while the framework using the fine-tuned model reduced the median dxy and dθ to 0.81 mm and 0.63°, respectively. In addition, the distributions of these results are summarized and compared using violin plots (**Figure 4-11**). **Figure 4-11a** and **Figure 4-11b** show dxyz and dθ using the proposed framework (without and with fine-tuning) and the discrepancy between the needle feature tip/axis orientation and physical needle tip location/axis orientation. There were differences in dxy ($p = 8x10^{-78}$) and dθ ($p = 2.7x10^{-11}$) among these three sets of results based on a Kruskal-Wallis test. The pair-wise comparison among 3 sets of results indicated that median and variance of dxy are both significantly lower by using the fine-tuned model. There were significant differences in the median and variance of dθ between the non-fine-tuned and fine-tuned models compared to the discrepancy between needle feature and physical needle axis orientation, but there were no significant differences between the non-fine-tuned and fine-tuned models. More details about significance and p value were shown in **Figure 4-11**.

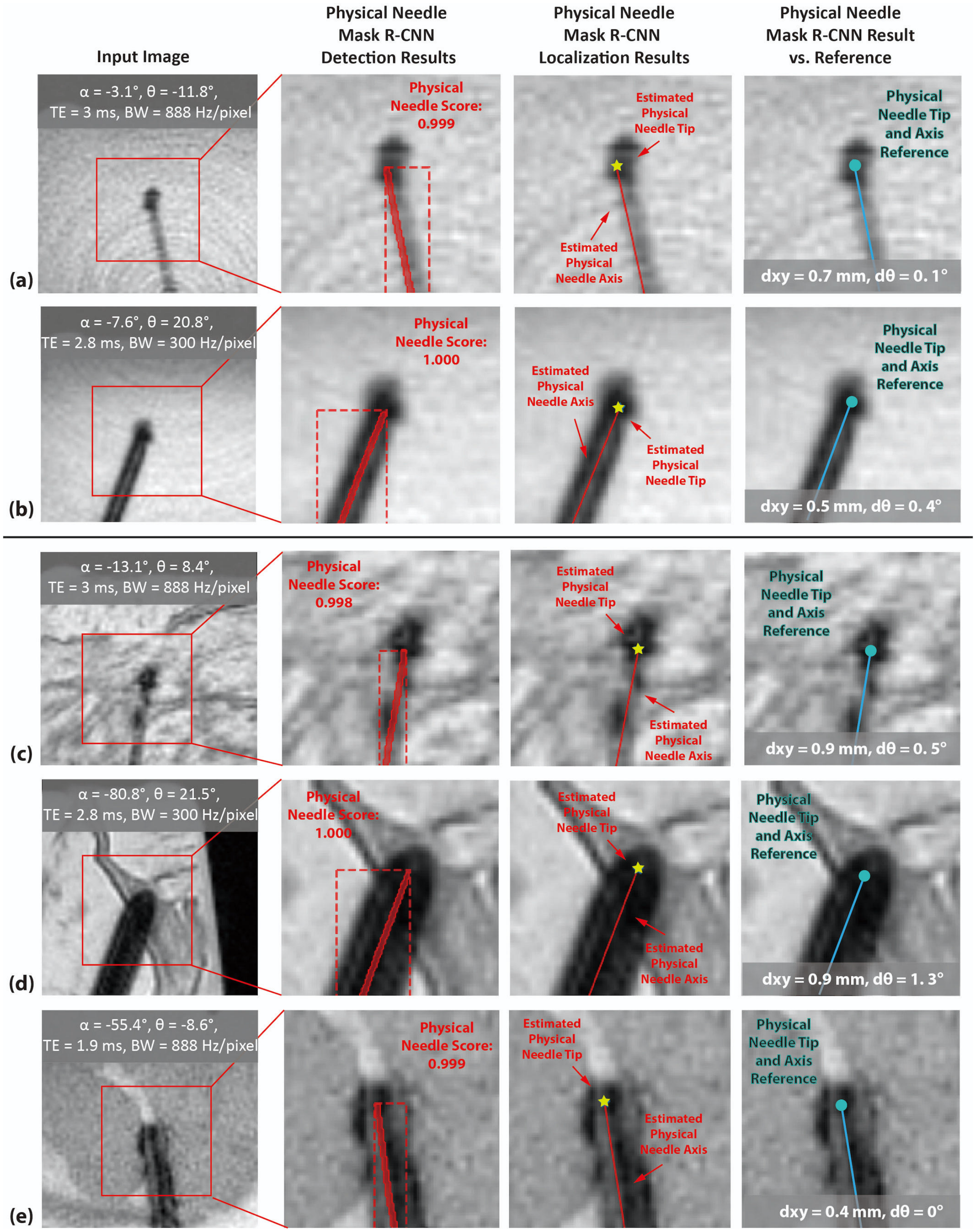

**Figure 4-9 (a-b) Example single-slice physical needle Mask R-CNN localization results in two gel phantom testing images with different imaging parameters and different needle tilting (α) and rotation (θ) angles. (c-e) Example single-slice physical needle Mask R-CNN localization results in three *ex vivo* tissue phantom testing images with different imaging parameters and different needle α and θ. The needle tip location (dxy) and axis orientation (dθ) differences compared to the reference (measurement during experiments) are reported in each example.**

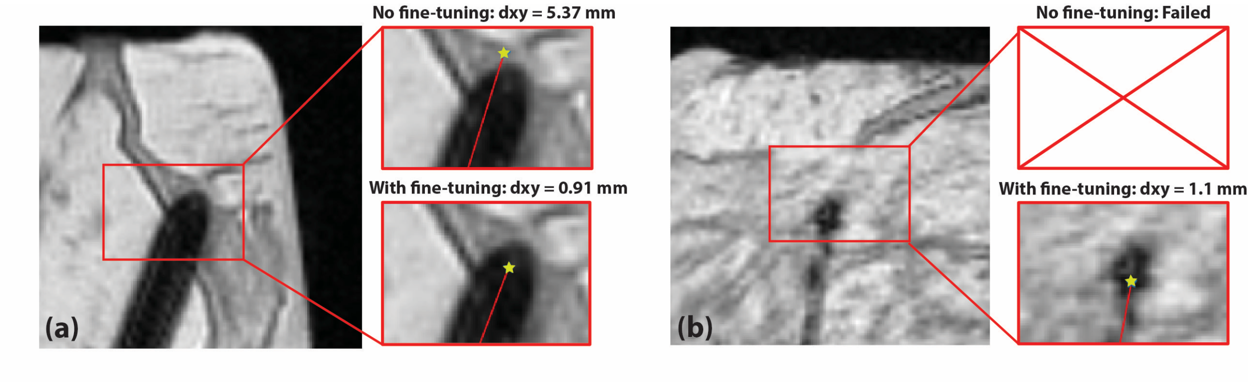

**Figure 4-10 Comparison of physical needle localization results using the single-slice physical needle Mask R-CNN models without and with fine-tuning. (a) Example of much larger physical needle localization error using the model without fine-tuning compared to the model with fine-tuning. (b) Example of needle detection failure using the model without fine-tuning and success using the model with fine-tuning.**

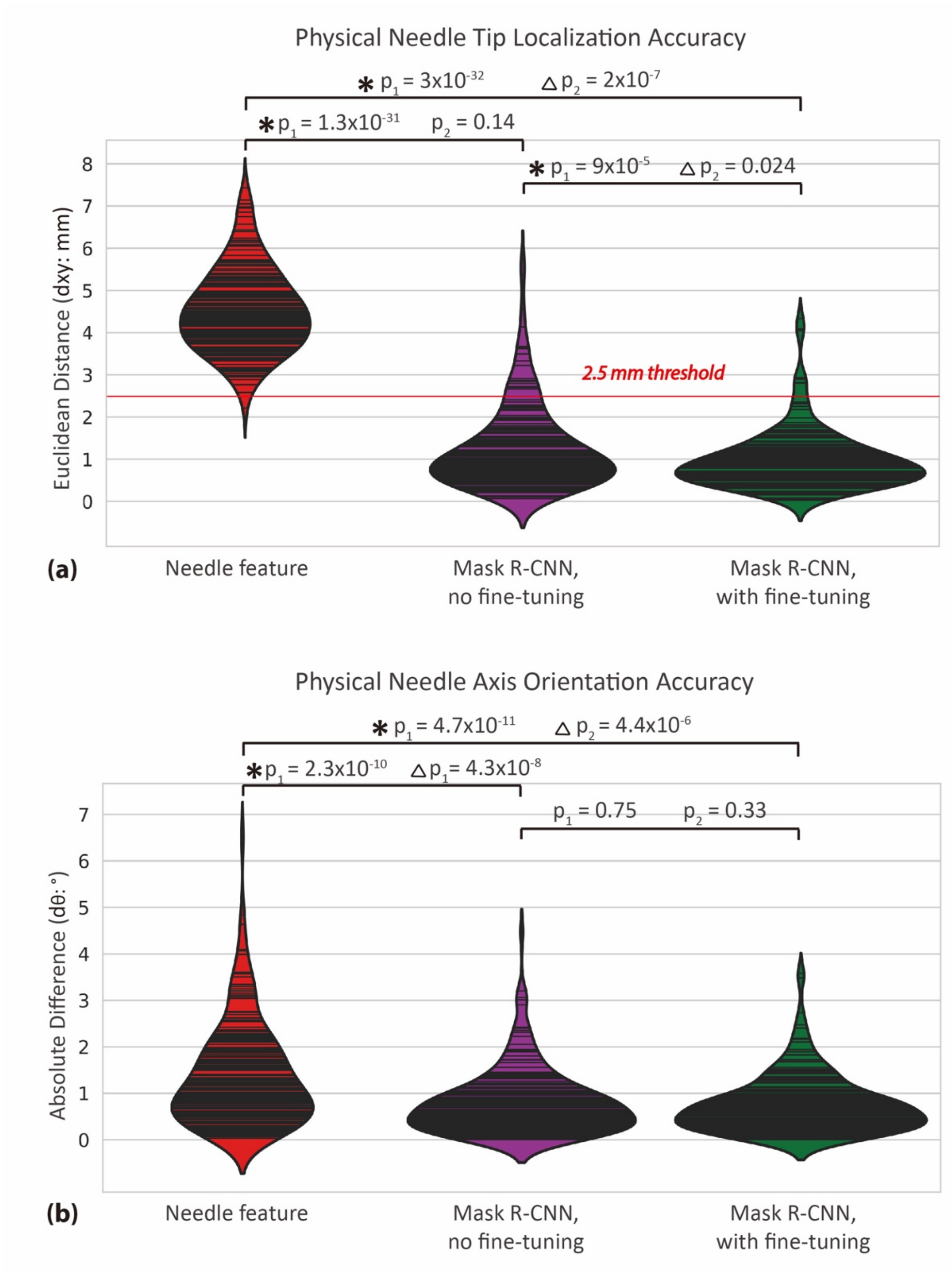

**Figure 4-11 Violin plots of single-slice physical needle (a) tip localization and (b) axis orientation results for the *ex vivo* tissue phantom testing dataset using needle feature localization and the physics-driven Mask R-CNN model without and with the fine-tuning step. In (a), The red line represents the 2.5 mm threshold considering clinically relevant tumor sizes of ≥5 mm diameter. In the pair-wise comparison, $p_1$ value of Wilcoxon signed rank test is on the left and $p_2$ value of Brown–Forsythe test is on the right. * indicates Wilcoxon signed rank test with $p_1 < 0.01$. Δ indicates Brown–Forsythe test with $p_2 < 0.05$.**

### 4.3.5 Three- Slice Physical Needle Mask R-CNN Testing with *Ex Vivo* Tissue Phantom Data

Overall training time for the 3-slice network was 48 hours. Representative results of 3D physical needle localization projected on 2D image slices and an orthogonal side view of the estimated physical needle using the single-slice and the 3-slice physical needle Mask R-CNN models are shown in **Figure 4-11**. These results showed accurate physical needle localization in 3D using the 3-slice model, compared with the reference. Physical needle axis orientation difference was reduced in the through-plane direction using the 3-slice model compared with the single-slice model. The processing time of the whole framework was about 200 ms per set of 3-parallel-slice images, which is suitable for real-time interventional MRI applications. The overall results are summarized in **Table 4-4**. The framework using the single-slice model achieved median dxyz and dϕ of 2.9 mm and 2.5°, respectively, while the framework using the 3-slice model reduced the median dxyz and dϕ to 2.2 mm and 1.2°, respectively.

The distributions of the results from all testing datasets are summarized and compared using violin plots (**Figure 4-12**). **Figure 4-12** show dxyz and dϕ using the proposed framework with single-slice and 3-slice models and the discrepancy between the needle feature tip/axis orientation and physical needle tip location/axis orientation. There were differences in both dxyz ($p = 1.1x10^{-59}$) and dϕ ($2.8x10^{-28}$) among these three sets of results based on a Kruskal-Wallis test. The pair-wise comparison among three sets of results indicated that dxyz and dϕ were significantly lower using the 3-slice model. No significant differences of variance in dxyz were observed from any of these pairs. On the other hand, the variance of dϕ was significantly lower by using the 3-slice model. More details about significance and p values are shown in **Figure 4-13**.

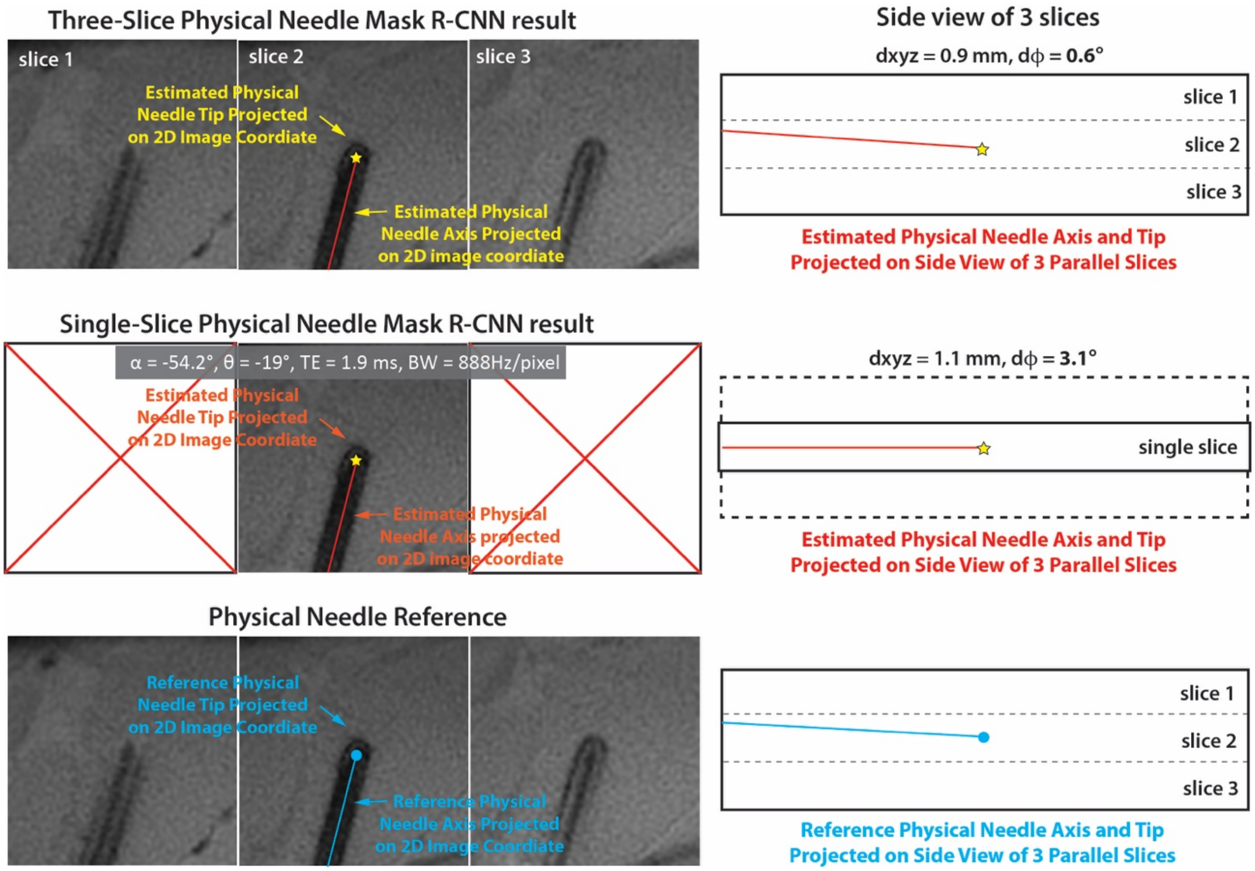

**Figure 4-12 Example 3-slice physical needle Mask R-CNN localization results and single-slice physical needle Mask R-CNN localization results projected on 2D image coordinate and side view.**

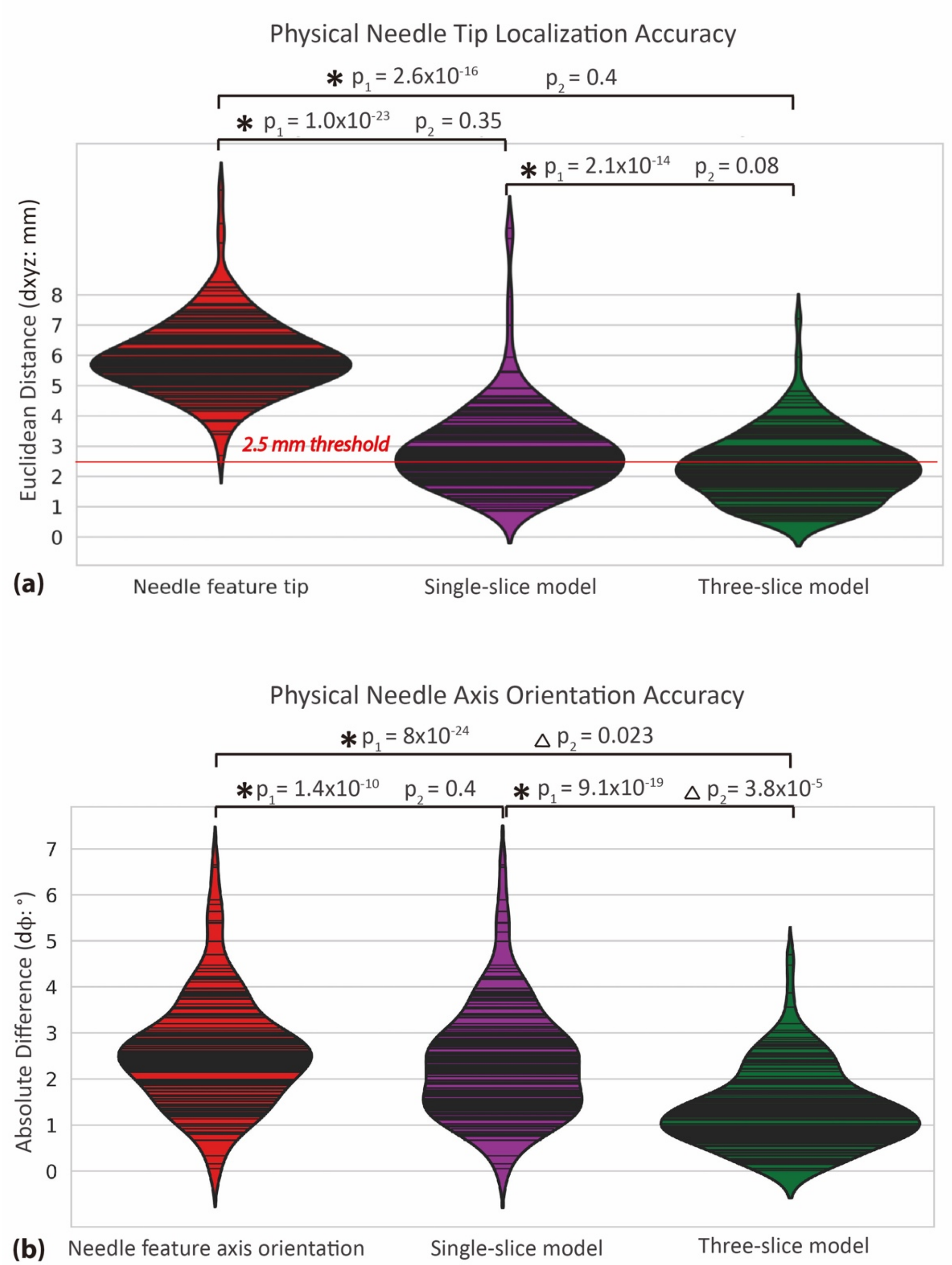

**Figure 4-13 Violin plots of physical needle (a) tip localization and (b) axis orientation results for the *ex vivo* tissue phantom testing dataset with certain range of misalignment between the needle axis and image plane orientation (shown in Table 4-3) using needle feature localization and the physics-driven single-slice and 3-slice Mask R-CNN models. In (a), The red line represents the 2.5 mm threshold considering clinically relevant tumor sizes of ≥5 mm diameter. In the pair-wise comparison, $p_1$ value of Wilcoxon signed rank test is on the left and $p_2$ value of Brown–Forsythe test is on the right. * indicates Wilcoxon signed rank test with $p_1 < 0.01$. Δ indicates Brown–Forsythe test with $p_2 < 0.05$.**

**Table 4-4 Physical needle localization accuracy using the proposed algorithm in the validation and testing datasets (see Table 4-2). Needle tip position errors (dxy or dxyz) and absolute needle axis orientation differences ($d\theta$ or $d\phi$) are reported. SD: standard deviation. IQR: interquartile range. Success: the physical needle Mask R-CNN detected the physical needle in the image. *Pixel size of the simulation model element or the acquired image.**

| | | | Mean | SD | Median | IQR | Max | dxy < 0.3 mm* or $d\theta < 1°$ (% of images) | Success rate |
|---|---|---|---|---|---|---|---|---|---|
| **Validation dataset 1 (20340 images)** | | dxy | 0.29 mm | 0.21 mm | 0.29 mm | 0.12 mm | 2.4 mm | 68.3% | 20340/20340 (100%) |
| | | $d\theta$ | 0.41° | 0.33° | 0.34° | 0.42° | 3.2° | 94.8% | |
| **Validation dataset 2 (14260 images)** | | dxy | 0.23 mm | 0.21 mm | 0.29 mm | 0.66 mm | 2.1 mm | 81.5% | 14260/14260 (100%) |
| | | $d\theta$ | 0.42° | 0.35° | 0.35° | 0.43° | 3.2° | 92.8% | |
| | | | Mean | SD | Median | IQR | Max | dxy < 1.17 mm* or $d\theta < 1°$ (% of images) | Success rate |
| **Gel phantom testing dataset (58 images)** | | dxy | 0.79 mm | 0.54 mm | 0.66 mm | 0.57 mm | 2.4 mm | 79.3% | 58/58 (100%) |
| | | $d\theta$ | 0.76° | 0.72° | 0.72° | 1.1° | 3.0° | 65.5% | |
| ***Ex vivo* tissue phantom single-slice testing dataset (186 images)** | **No fine-tuning** | dxy | 1.24 mm | 0.97 mm | 0.94 mm | 1 mm | 5.7 mm | 62.4% | 185/186 (99.5%) |
| | | $d\theta$ | 0.79° | 0.7° | 0.64° | 0.7° | 4.47° | 73.6% | |
| | **With fine-tuning** | dxy | 0.96 mm | 0.69 mm | 0.81 mm | 0.65 mm | 4.3 mm | 74.7% | 186/186 (100%) |
| | | $d\theta$ | 0.75° | 0.7° | 0.63° | 0.63° | 3.58° | 76.4% | |
| | | | Mean | SD | Median | IQR | Max | dxyz < 2.5 mm* or $d\phi < 1°$ (% of images) | Success rate |
| ***Ex vivo* tissue phantom 3-slice testing dataset (150 images)** | **Single slice** | dxyz | 3.1 mm | 1.4 mm | 2.9 mm | 1.5 mm | 10.2 mm | 35.3% | 150/150 (100%) |
| | | $d\phi$ | 2.4° | 1.2° | 2.5° | 1.2° | 6.7° | 12% | |
| | **Three slice** | dxyz | 2.3 mm | 1.1 mm | 2.2 mm | 1.2 mm | 7.2 mm | 57.3% | 150/150 (100%) |
| | | $d\phi$ | 1.4° | 0.85° | 1.2° | 1° | 4.7° | 52% | |

## 4.4 Discussion

In this study, we developed a new automatic physical needle localization framework for MRI-guided percutaneous interventions. The framework included two Mask R-CNN stages. First, the needle feature Mask R-CNN provided an initial estimate for the needle position. Next, the cropped image patch(es) containing the needle feature was sent to a single-slice or 3-slice physical needle Mask R-CNN. Firstly, we established a single-slice model taking a single-slice image as input, assuming the imaging plane is closely aligned with the physical needle. Secondly, we established a 3-slice model taking 3 parallel and adjacent slices as input, in which the imaging plane orientation could be misaligned with the physical needle axis. Both models were trained by a substantial set of physics-based simulation images that included realistic needle-induced susceptibility features. The cropped image patch helped to avoid false detection results and maintained the assumption of a rigid needle segment for the input to the physical needle Mask R-CNN models. The reference physical needle position was measured using a fiducial marker and needle actuator, which achieved stable and repeatable needle placement during the experiments [12]. Our validation and testing results demonstrated that the proposed framework with single-slice model accurately and rapidly estimates the physical needle position using single-slice MRI. The 3-slice model further reduced the through-plane needle localization error due to misaligned imaging plane with physical needle and rapidly estimated the overall 3D physical needle position.

As part of our framework, we developed an image-based needle susceptibility calibration method that compares the discrepancies between the physical needle and needle feature from experimental MRI data with the physics-based simulations in different situations. This calibration step can improve the understanding of the needle feature characteristics under specific conditions and on specific types of MR images. It showed that the discrepancies between needle feature and physical needle varied with different needle orientations and imaging parameters; proper selection of the needle susceptibility minimized the differences of the discrepancies (<0.4 mm) across these situations and ensured the fidelity of the simulated images for training. By adding noise during data augmentation, the simulated images formed a sufficient dataset to train the physical needle Mask R-CNN while avoiding the need for expensive MRI experiments and manual annotations.

The inverse problem of reconstructing a source object (e.g., device) based on its corresponding susceptibility map is an ill-posed problem, which may have indeterminate or incorrect solutions without additional constraints. Acquiring multiple scans with different imaging parameters, image orientations and larger computational resources may be required to obtain a reliable solution. Therefore, to determine the source object from its susceptibility-induced image features within the stringent time constraint of interventional procedures, we developed a supervised deep learning-based approach. Approaches (i.e., DeepQSM, QSMNet) to solve the field-to-source inversion problem for tissue susceptibility mapping adapted the CNN structure for semantic segmentation (e.g., U-Net). These previous U-Net-based methods aimed to solve for the tissue susceptibility map over the entire FOV based on the phase map, but this may not be suitable for the physical needle localization problem, which requires local information about the device. The instance segmentation network (Mask R-CNN) successfully learned the physical needle feature by integrating the bounding box and binary mask.

Our extended FORECAST method for single-slice physics-based simulation took about 10 hours and less than 100 Mbytes storage space to generate training data. This strategy was much more time-efficient than performing phantom MRI experiments. For model validation, the majority (60%-80%) of the physical needle tip localization error (dxy) was less than the simulation model element size (0.3 mm) and almost all (>90%) of the axis orientation estimation error (dθ) was lower than 1°. This close agreement with the ground truth corroborates the capability of the physics-based model to predict the in-plane physical needle location in different situations. In addition, our results showed that there is no need to retrain the model by combining the validation dataset into the training dataset, which significantly reduced the training time.

For gel phantom testing of the single-slice model, the proposed technique was applied to dynamic images with moderate temporal resolution around 1 sec, which maintained clear depiction of the needle feature. This temporal resolution is a reasonable choice since the physical needle position is mainly required during the final confirmation phase of the interventional procedure [66], when the needle insertion becomes slower and steps are taken to limit physiological motion (e.g., during a breath hold). Our gel phantom testing results achieved median dxy (0.66 mm) that was close to half of the pixel size (1.17 mm) and median dθ less than 1°. This demonstrates that the single-slice model trained by only simulation images can accurately localize the physical needle on phantom MR images.

*Ex vivo* tissue phantom MR images have realistic noise characteristics and also tissue features in the background, which resemble features expected on *in vivo* interventional MRI (**Figure 4-9c-e**). The statistical comparisons showed that the physical needle tip localization accuracy was improved by using the fine-tuned singe-slice model trained by fusing simulated needle features with tissue background patches. Even though the overall difference of the accuracy is not very large, the percentage of dxy >2.5 mm using the non-fine-tuned model is three times larger than the fine-tuned model. The threshold of 2.5 mm is informative, as clinically relevant tissue targets for minimally invasive interventions have diameters of 5-10 mm or larger[56]. Therefore, the fine-tuned model has potential to reduce mistargeting during MRI-guided interventions, especially for precise maneuvers in smaller targets. Furthermore, the physical needle localization error using the proposed network was lower than the localization error caused by the discrepancy between the physical needle and the needle feature. Overall, our results demonstrate that our proposed deep learning-based framework using single-slice model is an accurate and fast approach (processing time of 200 ms/image) to overcome the discrepancy, thereby achieving accurate physical needle localization on MRI. The fine-tuning scheme implemented in our framework can be used in future work to adapt it for specific *in vivo* applications (i.e., fine-tuning with additional *in vivo* datasets relevant for an MRI-guided procedure).

Our extended FORECAST method for the 3-slice physics-based simulation took about three days and 1 Gbyte storage space to generate the training data. Since the input and output of the 3-slice model are different from the single-slice model and other Mask R-CNN models for in-plane object detection and segmentation, no pretrained model was used during the training. *Ex vivo* tissue phantom images for 3-slice model testing considered a specified range of misalignment between the imaging plane and physical needle. Statistical comparisons of dxyz and dϕ demonstrated that the 3-slice model reduced the through-plane needle localization error compared with the single-slice model. Overall, the median 3D physical needle tip localization error was 2.2 mm and more than 50% of the results were <2.5 mm. This corresponds to 1 to 2 pixels in-plane and is less than the 5-mm slice thickness. While this localization performance is not at the subpixel level, as we have demonstrated for the case when the imaging plane is aligned with the needle, the direct 3D localization accuracy already can be sufficient for certain targeting applications (e.g., targets around 10 mm in diameter). If subpixel accuracy is needed, the current 3-slice model can provide information for updating the MRI scan plane to realign it with the physical needle during MRI-guided procedures using standard manual adjustments or new automated methods[131], followed by using our single-slice model for physical needle localization.

There are limitations in this study. Firstly, we only tested the GRE sequence with 3 different sets of imaging parameters that we often use in our research work. The proposed method could be applied to different interventional MRI sequences and imaging parameters by adjusting the simulation steps or by including the MRI parameters as inputs to the framework. Secondly, *in vivo* interventional MRI datasets were not included to evaluate the proposed technique. Due to difficulties of ground truth labeling of the physical needle position on *in vivo* datasets for training and testing, unsupervised or weakly supervised training strategies may be needed. Future work can acquire *in vivo* interventional MRI datasets from well-controlled animal experiments to further improve and evaluate our proposed technique.

## 4.5 Conclusion

In summary, we have developed a new physical needle localization framework based on physics-driven Mask R-CNN for MRI-guided percutaneous interventions. By calibrating the needle susceptibility value, the physics-based simulated needle feature achieved close agreement with actual MRI scans of the physical needle. We trained a single-slice physical needle Mask R-CNN model, in which the imaging plane is perfectly aligned with the needle. The validation results showed that the single-slice model uses the 2D passive needle feature on MRI to predict the physical needle with accuracy on the order of the model element size. The testing results in *ex vivo* tissue phantoms demonstrated sub-millimeter accuracy of physical needle localization with real-time processing. In addition, we trained a 3-slice physical needle Mask R-CNN model, in which the imaging plane is not aligned with the needle. The testing results in *ex vivo* tissue phantoms demonstrated improved through-plane needle localization accuracy compared with the single-slice model. Overall, the proposed framework can help to overcome the discrepancy between the passive needle feature and the physical needle during interventional MRI procedures.

# Chapter 5 Summary and Future Directions

## 5.1 Dissertation Summary

MRI-guided percutaneous interventions have advantages of excellent soft tissue contrast and absence of ionizing radiation exposure to both physicians and patients to improve needle-based targeted biopsy and focal therapy. A variety of cancerous lesions invisible in other image modalities such as CT and US can be visualized on MRI to provide target visualization for procedural guidance during interventions[21]. Compared to dynamic imaging modalities such as CTF, continuous guidance throughout a procedure can be accomplished without radiation using real-time MRI. However, the existing workflow of using MRI guidance is challenged by limited access to patients inside the scanner and tissue displacement due to physiological motion.

To overcome these challenges and expand the benefits of MRI guidance to more needle-based procedures, real-time MRI can be combined with a remote-controlled system to establish a real-time workflow for needle manipulation. Accurate target tissue tracking in the abdominal region and needle tracking are both critical for this new type of workflow, where MRI-guided computer-assisted navigation is a potential solution that does not require additional specialized hardware (e.g., optical sensors). However, multiple technical challenges must be addressed: firstly, target tracking under respiration motion is undermined by unavoidable system latencies and existing temporal prediction techniques were limited by the intrinsic trade-off between tracking accuracy and system latency in the conventional target tracking methods; secondly, needle tracking based on the passive needle feature is challenged by the signal-void feature variations across different MRI parameters and needle orientations; lastly, discrepancies between needle feature on MRI and underlying physical needle position could induce additional error for targeting procedures. This dissertation developed multiple techniques to resolve these issues and can help to improve MRI-guided computer-assisted navigation for percutaneous interventions.

Chapter 2 first developed an online real-time MRI motion tracking pipeline implemented using custom software modules for real-time image reconstruction of GA radial MRI, target motion tracking and prediction, and visualization. Calibration of system latency and tracking accuracy of the pipeline validated the respective advantages of surrogate-based tracking (lower latency) and image-based tracking (lower tracking error). A fusion-based respiratory motion tracking and prediction framework was developed using multi-rate Kalman filtering and real-time GA radial MRI. The retrospective *in vivo* results demonstrated that the proposed fusion-based method could achieve sub-pixel prediction error of targets during respiratory motion. Thus, this framework has the potential to improve the tracking accuracy of tissue targets in mobile organs and provide real-time motion information feedback for computer-assisted navigated procedures under manual or robotics-assisted control.

Chapter 3 adapted and trained Mask R-CNN for needle feature detection and segmentation on intra-procedural and real-time MR images. By applying an additional needle localization algorithm on the Mask R-CNN output, this automatic needle tracking algorithm consistently achieved pixel-level spatial accuracy for both needle feature tip localization in the prostate dataset and needle feature tracking in the *ex vivo* tissue dataset. The processing time of this algorithm is in real time since no ensemble step or test time augmentation was required. The needle position information from the algorithm has the potential to directly improve the accuracy of the needle manipulation by physicians in existing MRI-guided biopsy or provide accurate feedback information for dynamic robotics-assisted needle control with real-time MRI.

Chapter 4 proposed a two-stage Mask R-CNN framework for physical needle localization based on the passive needle feature on MRI. The initial validation and evaluation of the single-slice physical needle model illustrated that the in-plane discrepancies between needle features and underlying physical needles could be addressed using Mask R-CNN trained by simulated images. Evaluation using *ex vivo* tissue phantom MR images with a more realistic tissue background representing interventional MRI demonstrated sub-millimeter physical needle localization accuracy when the needle is perfectly aligned with the imaging plane within real-time processing time. Furthermore, the 3-slice physical needle model used in the framework can reduce through-plane needle localization error and rapidly estimate the overall 3D physical needle position. Both models in the framework can achieve physical needle localization in real-time for different situations. The physical needle position information obtained from this framework can be displayed as a virtual needle in the visual interface during the insertion and confirmation phases of needle-based targeting procedures.

Preliminary versions of the real-time MRI pipeline and computer-assisted navigation methods were implemented as a sensing module in an MRI-guided robotic system for adaptive tracking control of needle position in targets undergoing one-dimensional respiration induced motion[10]. This can be the basis for a real-time workflow to continuously update the needle path without asking patients to hold their breath for insertion steps. The overall procedural time could be reduced by eliminating the waiting time needed to reach a consistent respiratory motion state to update the needle path during breath-holding[141] Manual control of the needle to follow the target while avoiding cutting the tissue during free breathing is challenging. Robust and accurate robotic control with MRI-guided computer-assisted navigation has the potential to realize this new workflow. The updated navigation techniques in this dissertation have the potential to further improve the procedural accuracy and efficiency of such a real-time workflow using the MRI-guided robotic system.

Based on the fusion-based respiratory motion prediction framework implemented in a real-time MRI pipeline, the reduced system latency and improved in-plane target tissue tracking accuracy will benefit the motion-adaptive control of needle manipulation with respect to the target during respiratory motion, especially under fast or variable breathing patterns. With accurate needle feature and physical needle tracking techniques, robotics-assisted needle control relying on needle position feedback can be expanded to multi-degree of freedom (DOF), which is essential to support procedures in the abdomen. In addition, the proposed needle tracking method may also assist in the automatic update of needle guide geometric orientation parameters in the existing step-and-shoot workflow of MRI-guided procedures, such as in-bore prostate biopsy at UCLA medical center and other clinical sites. Furthermore, there are several future directions covered in sections 5.2 to 5.5 to address the limitations of the current techniques or improve the implementation to further explore the clinical impact.

## 5.2 Real-Time 3D Motion Prediction Model

Our proposed fusion-based multi-rate Kalman filter method in Chapter 2 demonstrated superior respiratory motion prediction accuracy in one dimension, the dominant superior-inferior (SI) direction. This framework can be readily extended to all three dimensions by acquiring more imaging planes such as interleaved orthogonal multi-slice real-time MRI[5]. In addition, measuring and providing the whole 3D deformation fields of the abdominal region has advantages to simultaneously monitor the deformable target tissue and surrounding critical structures to avoid[142]. However, it may be challenging to track 3D tissue deformation from real-time 2D multi-slice MRI. Therefore, a compelling strategy is to create a dynamic model to predict the 3D motion of the essential features. In the training phase, the respiratory motion can be modeled using principal component analysis (PCA) of deformation vector fields (DVF) from each motion state[143]. In the training phase, the respiratory motion can be modeled using principal component analysis (PCA) of deformation vector fields (DVF) from each motion state[144,145]. Real-time 2D multi-slice MRI can be acquired and registered with the planning image to initialize the DVF. The dynamic model is defined as a transformation of DVF(1 to t-1) to DVF(2 to t), where t is the time step. The motion state variable, including DVF and motion model, would be processed by an extended Kalman filter (EKF). 2D feature motion and 1D navigator signal (i.e., center of k-space signal every TR) can be simultaneously measured with different sampling rates and fused to overcome the system latency[10].

## 5.3 Automatic Real-Time Scan Plane Control for Needle Tracking

In the automatic needle tracking study (Chapter 3), misalignment between the MRI scan plane and needle can cause algorithm failure due to incomplete or missing features. Automatic alignment of scan planes with the needle can improve visualization to ensure procedural success and improve efficiency. However, existing techniques require additional hardware (e.g., fiber optic Bragg grating sensors) to monitor the device for scan plane alignment[146,147]. Recent studies have used deep learning (DL)-based methods to localize anatomical features for automatic cardiac MRI scan plane selection[148]. One possible approach is to develop an automatic method for MRI scan plane alignment with the needle using DL-based needle localization. In a preliminary study, I implemented a scan plane control (SPC) software module on an external workstation to automatically adjust and align the scan plane of the imaging sequence by leveraging accurate needle localization information obtained from the passive needle feature using our needle tracking Mask R-CNN (**Figure 5-1**)[131]. The scan plane alignment with a needle can be achieved using this module by localizing the needle feature on an orthogonal image. An initial workflow is proposed to update the imaging plane on the final plane scan (**Figure 5-2**).

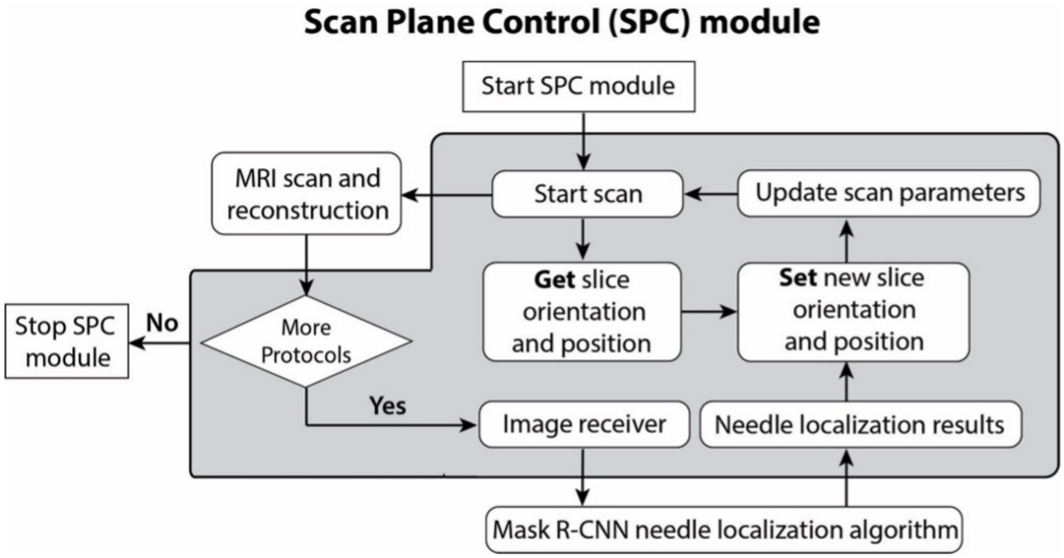

**Figure 5-1 The scan plane control (SPC) module used needle localization results from the Mask R-CNN algorithm to automatically align the MRI scan plane with the needle.**

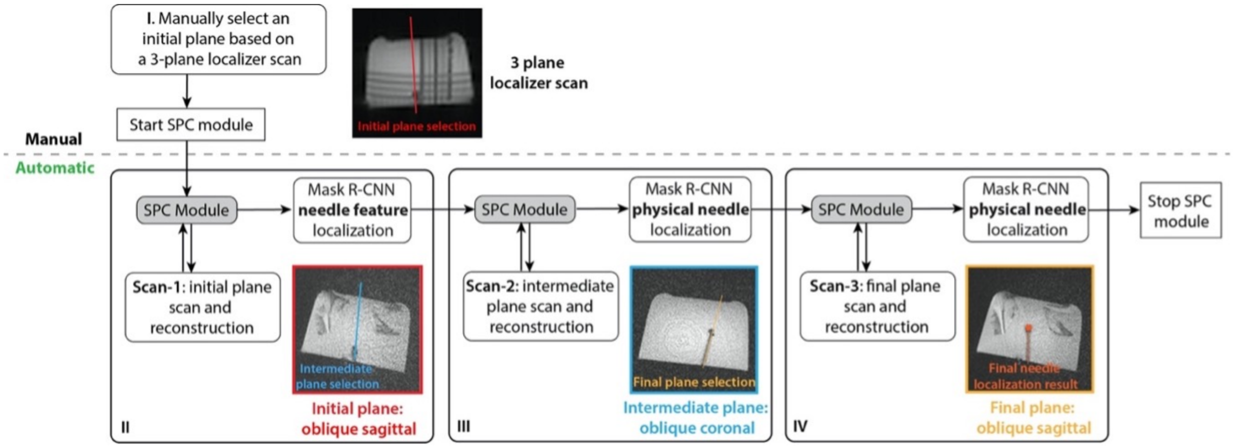

**Figure 5-2 The workflow for automatic MRI scan plane alignment with the needle using Mask R-CNN and the scan plane control (SPC) module. (I) An initial plane was manually selected based on the needle feature at the entry point on 3-plane localizer images. (II-IV) Scans 1-3 automatically started using the plane selection from the previous step. Mask R-CNN needle localization results were used to automatically select a new plane that aligned with the needle.**

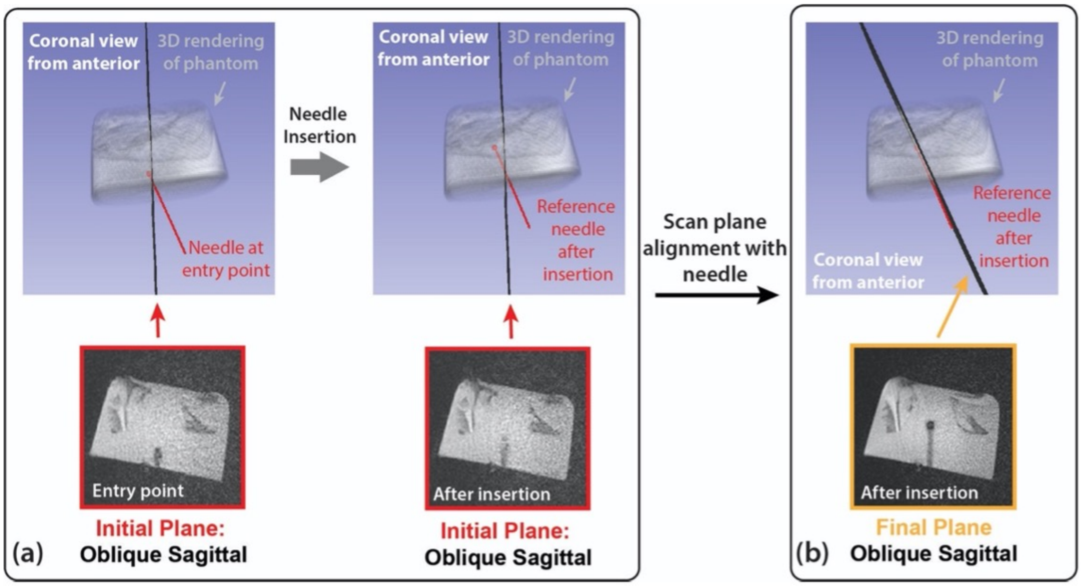

**Figure 5-3 The needle feature at the entry point and after insertion are displayed for the initial plane. The incomplete needle feature after insertion was caused by misalignment between the initial plane with the needle trajectory. Orientation difference (dθ) and Hausdorff distance (HD) are 19.2° and 13.9 mm. The reference needle was extracted by segmenting the needle feature on a high-resolution 3D confirmation scan. (b) After executing the proposed automated workflow, the final plane is aligned with the needle and the complete needle feature is visible. dθ and HD are 1.8° and 1.8 mm.**

Accurate scan plane alignment results of 1-DOF needle insertion experiments (**Figure 5-3**) demonstrated its potential to automatically update the image plane for each confirmation image of the step-and-shoot workflow. In future work, the software pipeline within the module can be modified to reduce both communication and processing time to fulfill the requirement of continuous scan plane alignment with a needle in an interactive real-time MRI sequence.

## 5.4 Improvements for 3D Physical Needle Localization

In the proposed physical needle localization framework based on physics-driven Mask R-CNN (Chapter 4), although the 3-slice model significantly reduced the through-plane physical needle localization error, the overall accuracy of the 3D physical needle localization was not yet at the level of the sub-pixel 2D localization results from the single-slice model for perfectly aligned imaging planes. Therefore, improving the current network may require a weighting factor to emphasize features on a specific channel location that is more representative of spatial information in the through-plane direction. One possible approach is designing a new spatial-channel attention to exploring spatial and channel interdependencies[149] to improve the learning of through-plane needle position based on passive needle feature distributed on each imaging plane.

## 5.5 Visual Software Interface

To integrate all these technical developments of MRI-guided computer-assisted navigation to achieve accurate and time-efficient percutaneous interventions, a visual software interface is necessary to display tissue and needle tracking results for physicians. An example (**Figure 5-4**) shows the needle visualization combined with (a) oblique axial intra-procedural MRI with needle insertion and (b) axial pre-procedural MRI without the needle in the 3D environment. The visualization node implemented in the 3D Slicer graphical interface needs to be augmented with a real-time MRI display and interactive graphical toolbox[42]. This visual interface will become a pivotal component to improve the user experience of physicians as the full system proceeds through phantom or pre-clinical evaluation in the future.

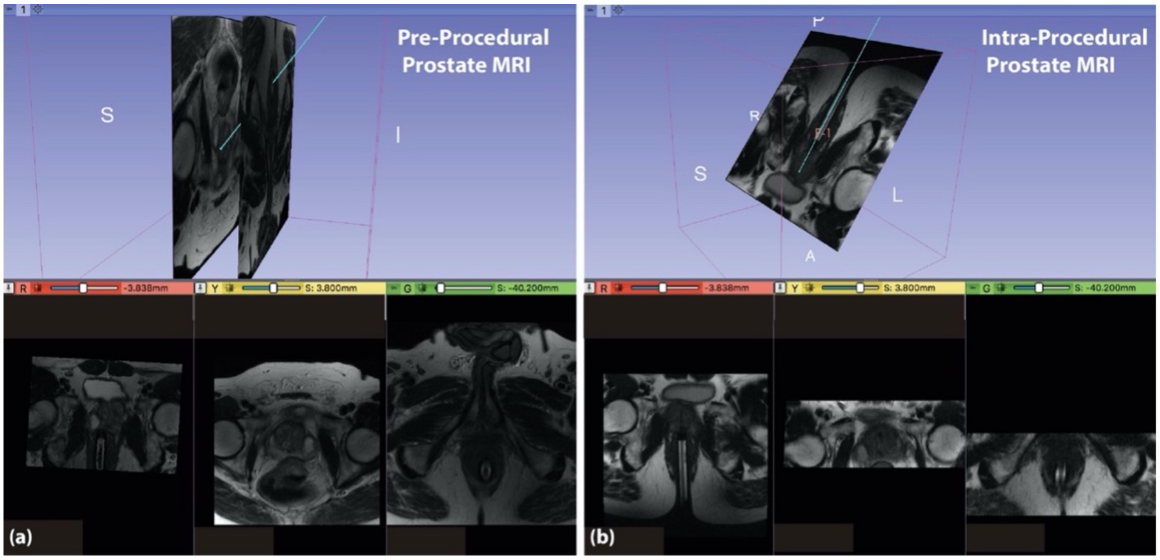

**Figure 5-4 (a) Needle model (blue) integrated with pre-procedural prostate MRI. (b) Needle model (blue) integrated with intra-procedural prostate MRI in the display interface.**

## 5.6 Conclusion

With the improved respiratory motion prediction and needle tracking algorithms, the new computer-assisted navigation techniques developed in this dissertation can extract accurate tissue and instrument positions from MRI in real time and have the potential to realize new workflows for accurate and efficient MRI-guided needle-based interventional procedures. Furthermore, a combination of these computer-assisted navigation methods with a real-time MRI pipeline has been established as a platform to further assist the dynamic procedural guidance for moving targets. The improved targeting accuracy during dynamic guidance will be essential to realize and expand the clinical value of MRI-guided percutaneous interventions.

# Appendix

The Kalman filter[150] recursively solves a linear problem for stochastic estimation of an underlying state in a dynamic system, taking into consideration the noise in the state transition and measurement processes. For respiratory motion state prediction, a state space model is constructed based on the discretized-time dynamic system of respiratory motion and a common linear measurement system. $F$ and $H$ denote the linear matrix form of the state transition function and the measurement function, respectively. $t$ denotes the discretized time step index in the dynamic model, $x$ denotes the unknown true motion state, and $y$ denotes the motion state measurement. The fundamental assumption of using the Kalman filter to estimate the true motion state is that the noise of the transition process model $w$ and the noise of the measurement model $v$ have Gaussian distribution with zero mean and covariance (Q, R), while the state space variable is also a Gaussian random variable with mean of $\bar{x}$ and covariance of $P$:

**Equation A-1**

$$x(t) = Fx(t-1) + w(t) \sim \mathcal{N}(0, Q(t))$$

**Equation A-2**

$$y(t) = Hx(t) + v(t) \sim \mathcal{N}(0, R(t))$$

The one-step update for the estimated mean of the motion state based on the state transition model and previous estimation $\bar{x}(t|t-1)$ is denoted as $\bar{x}(t|t)$ and the associated covariance $P(t|t-1)$ is also updated:

**Equation A-3**

$$\bar{x}(t|t-1) = F\bar{x}(t-1|t-1)$$

**Equation A-4**

$$P(t|t-1) = FP(t-1|t-1)F^T + Q(t-1)$$

The linear solution to minimize mean squared error (MSE) of the estimation is described in the following equation, where *z* denotes the motion tracking measurement:

**Equation A-5**

$$\boldsymbol{\overline{x}(t|t) = \overline{x}(t|t-1) + K(t)(z(t) - H\overline{x}(t|t-1))}$$

**Equation A-6**

$$P(t|t) = (I - K(t)H)P(t|t-1)$$

$K(t+1)$ is the Kalman gain, which is updated at each time step to maximize the likelihood that the MSE of the estimated mean approaches zero.

**Equation A-7**

$$K(t) = P(t|t-1)H^T(P(t|t-1)HP(t|t-1)^T + R(t))^{-1}$$

# References

1. McWilliams JP, Lee EW, Yamamoto S, Loh CT, Kee ST. Image-Guided Tumor Ablation: Emerging Technologies and Future Directions. *Semin Interv Radiol* 2010;27(3):302-313. doi:10.1055/s-0030-1261789
2. Gupta S, Madoff DC. Image-Guided Percutaneous Needle Biopsy in Cancer Diagnosis and Staging. *Tech Vasc Interv Radiol* 2007;10(2):88-101. doi:10.1053/j.tvir.2007.09.005
3. Stattaus J, Kuehl H, Ladd S, Schroeder T, Antoch G, Baba HA, Barkhausen J, Forsting M. CT-Guided Biopsy of Small Liver Lesions: Visibility, Artifacts, and Corresponding Diagnostic Accuracy. *Cardiovasc Intervent Radiol* 2007;30(5):928-935. doi:10.1007/s00270-007-9023-8
4. Kim PN, Choi D, Rhim H, Rha SE, Hong HP, Lee J, Choi JI, Kim JW, Seo JW, Lee EJ, Lim HK. Planning Ultrasound for Percutaneous Radiofrequency Ablation to Treat Small (≤ 3 cm) Hepatocellular Carcinomas Detected on Computed Tomography or Magnetic Resonance Imaging: A multicenter Prospective Study to Assess Factors Fffecting Ultrasound Visibility. *J Vasc Interv Radiol* 2012;23(5):627-634. doi:10.1016/j.jvir.2011.12.026
5. Stattaus J, Maderwald S, Baba HA, Gerken G, Barkhausen J, Forsting M, Ladd ME. MR-Guided Liver Biopsy within a Short, Wide-Bore 1.5 Tesla MR System. *Eur Radiol* 2008;18(12):2865-2873. doi:10.1007/s00330-008-1088-5
6. Stattaus J, Maderwald S, Forsting M, Barkhausen J, Ladd ME. MR-Guided Core Biopsy with MR Fluoroscopy Using a Short, Wide-Bore 1.5-Tesla Scanner: Feasibility and Initial Results. *J Magn Reson Imaging* 2008;27(5):1181-1187. doi:10.1002/jmri.21075

7. Tan N, Lin W-C, Khoshnoodi P, Asvadi NH, Yoshida J, Margolis DJA, Lu DSK, Wu H, Sung KH, Lu DY, Huang J, Raman SS. In-bore 3-T MR-guided Transrectal Targeted Prostate Biopsy: Prostate Imaging Reporting and Data System Version 2–Based Diagnostic Performance for Detection of Prostate Cancer. *Radiology* 2016;283(1):130-139. doi:10.1148/radiol.2016152827

8. Moche M, Heinig S, Garnov N, Fuchs J, Petersen TO, Seider D, Brandmaier P, Kahn T, Busse H. Navigated MRI-Guided Liver Biopsies in a Closed-Bore Scanner: Experience in 52 Patients. *Eur Radiol* 2016;26(8):2462-2470. doi:10.1007/s00330-015-4097-1

9. Busse H, Garnov N, Thörmer G, Zajonz D, Gründer W, Kahn T, Moche M. Flexible Add-on Solution for MR image-Guided Interventions in a Closed-Bore Scanner Environment. *Magn Reson Med* 2010;64(3):922-928. doi:10.1002/mrm.22464

10. Lee Y-H, Li X, Simonelli J, Lu D, Wu HH, Tsao T-C. Adaptive Tracking Control of One-Dimensional Respiration Induced Moving Targets by Real-Time Magnetic Resonance Imaging Feedback. *IEEE/ASME Int Conf Adv Intell Mechatron* 2020;25(4):1894 - 1903. doi:10.1109/TMECH.2020.2998150

11. Wu D, Li G, Patel N, Yan J, Monfaredi R, Cleary K, Iordachita I. Remotely Actuated Needle Driving Device for MRI-Guided Percutaneous Interventions. *Proc International Symposium on Medical Robotics (ISMR)* 2019:1-7. doi:10.1109/ISMR.2019.8710176

12. Simonelli J, Lee Y, Chen C, Li X, Mikaiel S, Lu D, Wu HH, Tsao T. Hydrostatic Actuation for Remote Operations in MR Environment. *IEEE/ASME Trans Mechatronics* 2019;25(2):894 - 905. doi:10.1109/TMECH.2019.2959805

13. Campbell-Washburn AE, Rogers T, Stine AM, Khan JM, Ramasawmy R, Schenke WH, McGuirt DR, Mazal JR, Grant LP, Grant EK, Herzka DA, Lederman RJ. Right Heart

Catheterization Using Metallic Guidewires and Low SAR Cardiovascular Magnetic Resonance Fluoroscopy at 1.5 Tesla: First in Human Experience. *J Cardiovasc Magn Reson* 2018;20(1):41. doi:10.1186/s12968-018-0458-7

14. Campbell-Washburn AE, Tavallaei MA, Pop M, Grant EK, Chubb H, Rhode K, Wright GA. Real-Time MRI Guidance of Cardiac Interventions. *J Magn Reson Imaging* 2017;46(4):935-950. doi:10.1002/jmri.25749

15. Ahmed M, Solbiati L, Brace CL, Breen DJ, Callstrom MR, Charboneau JW, Chen M-H, Choi BI, de Baère T, Dodd GD, Dupuy DE, Gervais DA, Gianfelice D, Gillams AR, Lee FT, Leen E, Lencioni R, Littrup PJ, Livraghi T, Lu DS, McGahan JP, Meloni MF, Nikolic B, Pereira PL, Liang P, Rhim H, Rose SC, Salem R, Sofocleous CT, Solomon SB, Soulen MC, Tanaka M, Vogl TJ, Wood BJ, Goldberg SN. Image-Guided Tumor Ablation: Standardization of Terminology and Reporting Criteria—A 10-Year Update. *Radiology* 2014;273(1):241-260. doi:10.1148/radiol.14132958

16. Marien A, Gill I, Ukimura O, Nacim B, Villers A. Target Ablation—Image-Guided Therapy in Prostate Cancer. *Urol Oncol* 2014;32(6):912-923. doi:10.1016/j.urolonc.2013.10.014

17. Paltieli Y, Degani S, Zrayek A, Gonen R, Lewinski MR, Zamberg Y, Ohel G. A New Guidance System for Freehand, Obstetric Ultrasound-Guided Procedures. *Ultrasound Obstet Gynecol* 2002;19(3):269-273. doi:10.1046/j.1469-0705.2002.00607.x

18. Heerink W. CT-Guided Percutaneous Interventions [Thesis fully internal (DIV)]. Groningen: Rijksuniversiteit Groningen; 2019.

19. Gupta S. New Techniques in Image-Guided Percutaneous Biopsy. *Cardiovasc Intervent Radiol* 2004;27(2):91-104. doi:10.1007/s00270-003-0056-3

20. Kim EE. Image-Guided Cancer Therapy: A Multidisciplinary Approach. *J Nucl Med* 2014;55(7):1214. doi:10.2967/jnumed.114.141085

21. Gombos EC, Jagadeesan J, Richman DM, Kacher DF. Magnetic Resonance Imaging-Guided Breast Interventions: Role in Biopsy Targeting and Lumpectomies. *Magn Reson Imaging Clin N Am* 2015;23(4):547-561. doi:10.1016/j.mric.2015.05.004

22. Lim S, Lee MW, Rhim H, Cha DI, Kang TW, Min JH, Song KD, Choi S-y, Lim HK. Mistargeting after Fusion Imaging Guided Percutaneous Radiofrequency Ablation of Hepatocellular Carcinomas. *J Vasc Interv Radiol* 2014;25(2):307-314. doi:10.1016/j.jvir.2013.10.025

23. Schenck JF, Jolesz FA, Roemer PB, Cline HE, Lorensen WE, Kikinis R, Silverman SG, Hardy CJ, Barber WD, Laskaris ET, et al. Superconducting Open-Configuration MR Imaging System for Image-Guided Therapy. *Radiology* 1995;195(3):805-814. doi:10.1148/radiology.195.3.7754014

24. Fischbach F, Bunke J, Thormann M, Gaffke G, Jungnickel K, Smink J, Ricke J. MR-Guided Freehand Biopsy of Liver Lesions With Fast Continuous Imaging Using a 1.0-T Open MRI Scanner: Experience in 50 Patients. *Cardiovasc Intervent Radiol* 2010;34:188-192. doi:10.1007/s00270-010-9836-8

25. Streitparth F, Althoff C, Jonczyk M, Guettler F, Maurer M, Rathke H, Sponheuer KM, Hamm B, Teichgräber UK, de Bucourt M. Tailored Interactive Sequences for Continuous MR-Image-Guided Freehand Biopsies of Different Organs in an Open System at 1.0 Tesla (T) – Initial Experience. *Biomedical Engineering / Biomedizinische Technik* 2017;62(6):557-563. doi:doi:10.1515/bmt-2015-0163

26. Fritz J, Thomas C, Clasen S, Claussen CD, Lewin JS, Pereira PL. Freehand Real-Time MRI-Guided Lumbar Spinal Injection Procedures at 1.5 T: Feasibility, Accuracy, and Safety. *AJR Am J Roentgenol* 2009;192(4):W161-167. doi:10.2214/ajr.08.1569

27. Rothgang E, Gilson WD, Wacker F, Hornegger J, Lorenz CH, Weiss CR. Rapid Freehand MR-Guided Percutaneous Needle Interventions: An Image-Based Approach to Improve Workflow and Feasibility. *J Magn Reson Imaging* 2013;37(5):1202-1212. doi:10.1002/jmri.23894

28. Fischbach F, Wien L, Krueger S, Schnackenburg B, Baumunk D, Friebe B, Schostak M, Ricke J, Fischbach K. Feasibility Study of MR-Guided Transgluteal Targeted In-Bore Biopsy for Suspicious Lesions of the Prostate at 3 Tesla Using a Freehand Approach. *Eur Radiol* 2018;28(6):2690-2699. doi:10.1007/s00330-017-5187-z

29. Pokorny M, Kua B, Esler R, Yaxley J, Samaratunga H, Dunglison N, Gianduzzo T, Coughlin G, Holt R, Laing B, Ault D, Brown N, Parkinson R, Thompson L. MRI-Guided In-Bore Biopsy for Prostate Cancer: What Does the Evidence Say? A Case Series of 554 Patients and a Review of the Current Literature. *World J Urol* 2019;37(7):1263-1279. doi:10.1007/s00345-018-2497-y

30. Schimmöller L, Blondin D, Arsov C, Rabenalt R, Albers P, Antoch G, Quentin M. MRI-Guided In-Bore Biopsy: Differences Between Prostate Cancer Detection and Localization in Primary and Secondary Biopsy Settings. *AJR Am J Roentgenol* 2015;206(1):92-99. doi:10.2214/AJR.15.14579

31. Li G, Patel NA, Wang Y, Dumoulin C, Loew W, Loparo O, Schneider K, Sharma K, Cleary K, Fritz J, Iordachita I. Fully Actuated Body-Mounted Robotic System for MRI-Guided

Lower Back Pain Injections: Initial Phantom and Cadaver Studies. *IEEE Robot Autom Lett* 2020;5(4):5245-5251. doi:10.1109/LRA.2020.3007459

32. Burkhard N, Frishman S, Gruebele A, Whitney JP, Goldman R, Daniel B, Cutkosky M. A Rolling-Diaphragm Hydrostatic Transmission for Remote MR-Guided Needle Insertion. *Proc IEEE International Conference on Robotics and Automation* 2017:1148-1153. doi:10.1109/ICRA.2017.7989137

33. Meyer BC, Brost A, Kraitchman DL, Gilson WD, Strobel N, Hornegger J, Lewin JS, Wacker FK. Percutaneous Punctures with MR Imaging Guidance: Comparison between MR Imaging–Enhanced Fluoroscopic Guidance and Real-Time MR Imaging Guidance. *Radiology* 2013;266(3):912-919. doi:10.1148/radiol.12120117

34. Campbell-Washburn AE, Faranesh AZ, Lederman RJ, Hansen MS. Magnetic Resonance Sequences and Rapid Acquisition for MR-Guided Interventions. *Magn Reson Imaging Clin N Am* 2015;23(4):669-679. doi:10.1016/j.mric.2015.05.006

35. Adluru G, McGann C, Speier P, Kholmovski EG, Shaaban A, DiBella EVR. Acquisition and Reconstruction of Undersampled Radial Data for Myocardial Perfusion Magnetic Resonance Imaging. *J Magn Reson Imaging* 2009;29(2):466-473. doi:10.1002/jmri.21585

36. Winkelmann S, Schaeffter T, Koehler T, Eggers H, Doessel O. An Optimal Radial Profile Order Based on the Golden Ratio for Time-Resolved MRI. *IEEE Trans Med Imaging* 2007;26(1):68-76. doi:10.1109/TMI.2006.885337

37. Rasche V, Boer RWD, Holz D, Proksa R. Continuous Radial Data Acquisition for Dynamic MRI. *Magn Reson Med* 1995;34(5):754-761. doi:10.1002/mrm.1910340515

38. Hansen MS, Sørensen TS. Gadgetron: An Open Source Framework for Medical Image Reconstruction. *Magn Reson Med* 2013;69(6):1768-1776. doi:10.1002/mrm.24389

39. Keall PJ, Mageras GS, Balter JM, Emery RS, Forster KM, Jiang SB, Kapatoes JM, Low DA, Murphy MJ, Murray BR, Ramsey CR, Van Herk MB, Vedam SS, Wong JW, Yorke E. The Management of Respiratory Motion in Radiation Oncology Report of AAPM Task Group 76a). *Med Phys* 2006;33(10):3874-3900. doi:10.1118/1.2349696

40. He Z, Dong Z, Fang G, Ho JD, Cheung C, Chang H, Chong CC, Chan JY, Chan DTM, Kwok K. Design of a Percutaneous MRI-Guided Needle Robot With Soft Fluid-Driven Actuator. *IEEE Robot Autom Lett* 2020;5(2):2100-2107. doi:10.1109/LRA.2020.2969929

41. Henken K, Van Gerwen D, Dankelman J, Van Den Dobbelsteen J. Accuracy of Needle Position Measurements Using Fiber Bragg Gratings. *Minim Invasive Ther Allied Technol* 2012;21(6):408-414. doi:10.3109/13645706.2012.666251

42. Fedorov A, Beichel R, Kalpathy-Cramer J, Finet J, Fillion-Robin JC, Pujol S, Bauer C, Jennings D, Fennessy F, Sonka M, Buatti J, Aylward S, Miller JV, Pieper S, Kikinis R. 3D Slicer as an Image Computing Platform for the Quantitative Imaging Network. *Magn Reson Med* 2012;30(9):1323-1341. doi:10.1016/j.mri.2012.05.001

43. Mewes A, Heinrich F, Hensen B, Wacker F, Lawonn K, Hansen C. Concepts for Augmented Reality Visualization to Support Needle Guidance Inside the MRI. *Healthc Technol Lett* 2018;5(5):172-176. doi:10.1049/htl.2018.5076

44. Heinrich F, Schmidt G, Bornemann K, Roethe AL, Essayed W, Hansen C. Visualization Concepts to Improve Spatial Perception for Instrument Navigation in Image-Guided Surgery. *Proc SPIE 10951, Medical Imaging 2019: Image-Guided Procedures, Robotic Interventions, and Modeling* 2019:1095125. doi:10.1117/12.2512761

45. Xu H, Lasso A, Fedorov A, Tuncali K, Tempany C, Fichtinger G. Multi-Slice-to-Volume Registration for MRI-Guided Transperineal Prostate Biopsy. *Int J Comput Assist Radiol Surg* 2015;10(5):563-572. doi:10.1007/s11548-014-1108-7

46. Mastmeyer A, Pernelle G, Ma R, Barber L, Kapur T. Accurate Model-Based Segmentation of Gynecologic Brachytherapy Catheter Collections in MRI-Images. *Med Image Anal* 2017;42:173-188. doi:10.1016/j.media.2017.06.011

47. Seregni M, Paganelli C, Lee D, Greer PB, Baroni G, Keall PJ, Riboldi M. Motion Prediction in MRI-Guided Radiotherapy Based on Interleaved Orthogonal Cine-MRI. *Phys Med Biol* 2016;61(2):872-887. doi:10.1088/0031-9155/61/2/872

48. Sharp GC, Jiang SB, Shimizu S, Shirato H. Prediction of Respiratory Tumour Motion for Real-Time Image-Guided Radiotherapy. *Phys Med Biol* 2004;49(3):425-425. doi:10.1088/0031-9155/49/3/006

49. Paganelli C, Seregni M, Fattori G, Summers P, Bellomi M, Baroni G, Riboldi M. Magnetic Resonance Imaging-Guided versus Surrogate-Based Motion Tracking in Liver Radiation Therapy: a Prospective Comparative Study. *Int J Radiat Oncol Biol Phys* 2015;91(4):840-848. doi:10.1016/j.ijrobp.2014.12.013

50. Seregni M, Paganelli C, Summers P, Bellomi M, Baroni G, Riboldi M. A Hybrid Image Registration and Matching Framework for Real-Time Motion Tracking in MRI-Guided Radiotherapy. *IEEE Trans Biomed Eng* 2018;65(1):131-139. doi:10.1109/TBME.2017.2696361

51. Jin Lee S, Motai Y. Prediction and Classification of Respiratory Motion. Volume 525; 2014.

52. Zijlstra F, Bouwman JG, Braškutė I, Viergever MA, Seevinck PR. Fast Fourier-Based Simulation of Off-Resonance Artifacts in Steady-State Gradient Echo MRI Applied to Metal Object Localization. *Magn Reson Med* 2017;78(5):2035-2041. doi:10.1002/mrm.26556

53. Weine J, Breton E, Garnon J, Gangi A, Maier F. Deep Learning Based Needle Localization on Real-Time MR Images of Patients Acquired during MR-Guided Percutaneous Interventions. *Proc ISMRM 27th Annual Meeting* 2019:973.

54. Mehrtash A, Ghafoorian M, Pernelle G, Ziaei A, Heslinga FG, Tuncali K, Fedorov A, Kikinis R, Tempany CM, Wells WM, Abolmaesumi P, Kapur T. Automatic Needle Segmentation and Localization in MRI With 3-D Convolutional Neural Networks: Application to MRI-Targeted Prostate Biopsy. *IEEE Trans Med Imaging* 2019;38(4):1026-1036. doi:10.1109/TMI.2018.2876796

55. Song S-E, Cho NB, Iordachita II, Guion P, Fichtinger G, Whitcomb LL. A Study of Needle Image Artifact Localization in Confirmation Imaging of MRI-Guided Robotic Prostate Biopsy. *Proc IEEE International Conference on Robotics and Automation* 2011;2011:4834-4839. doi:10.1109/ICRA.2011.5980309

56. Kim YK, Kim YK, Park HJ, Park MJ, Lee WJ, Choi D. Noncontrast MRI with diffusion-weighted imaging as the sole imaging modality for detecting liver malignancy in patients with high risk for hepatocellular carcinoma. *Magn Reson Imaging* 2014;32(6):610-618. doi:10.1016/j.mri.2013.12.021

57. Sonnow L, Gilson WD, Raithel E, Nittka M, Wacker F, Fritz J. Instrument Visualization Using Conventional and Compressed Sensing SEMAC for Interventional MRI at 3T. *J Magn Reson Imaging* 2018;47(5):1306-1315. doi:10.1002/jmri.25858

58. Bollmann S, Rasmussen KGB, Kristensen M, Blendal RG, Østergaard LR, Plocharski M, O'Brien K, Langkammer C, Janke A, Barth M. DeepQSM - Using Deep Learning to Solve the Dipole Inversion for Quantitative Susceptibility Mapping. *Neuroimage* 2019;195:373-383. doi:10.1016/j.neuroimage.2019.03.060

59. Yoon J, Gong E, Chatnuntawech I, Bilgic B, Lee J, Jung W, Ko J, Jung H, Setsompop K, Zaharchuk G, Kim EY, Pauly J, Lee J. Quantitative Susceptibility Mapping Using Deep Neural Network: QSMnet. *Neuroimage* 2018;179:199-206. doi:10.1016/j.neuroimage.2018.06.030

60. Sedaghat F, Tuncali K. Enabling Technology for MRI-Guided Intervention. *Top Magn Reson Imaging* 2018;27(1). doi:10.1097/RMR.0000000000000148

61. Kaye EA, Granlund KL, Morris EA, Maybody M, Solomon SB. Closed-Bore Interventional MRI: Percutaneous Biopsies and Ablations. *AJR Am J Roentgenol* 2015;205(4):W400-W410. doi:10.2214/AJR.15.14732

62. Eslami S, Shang W, Li G, Patel N, Fischer GS, Tokuda J, Hata N, Tempany CM, Iordachita I. In-Bore Prostate Transperineal Interventions with an MRI-Guided Parallel Manipulator: System Development and Preliminary Evaluation. *Int J Med Robot* 2016;12(2):199-213. doi:10.1002/rcs.1671

63. Vartholomeos P, Qin L, Dupont PE. MRI-Powered Actuators for Robotic Interventions. *Proc IEEE International Conference on Intelligent Robots and Systems* 2011:4508-4515. doi:10.1109/IROS.2011.6048692

64. Fischer GS, Iordachita I, Csoma C, Tokuda J, Mewes PW, Tempany CM, Hata N, Fichtinger G. Pneumatically Operated MRI-Compatible Needle Placement Robot for

Prostate Interventions. *Proc IEEE International Conference on Robotics and Automation* 2008:2489-2495. doi:10.1109/ROBOT.2008.4543587

65. Cole GA, Harrington K, Su H, Camilo A, Pilitsis JG, Fischer GS. Closed-Loop Actuated Surgical System Utilizing Real-Time In-Situ MRI Guidance. *Proc 12th International Symposium on Experimental Robotics* 2014:785-798. doi:10.1007/978-3-642-28572-1_54

66. Mikaiel S, Simonelli J, Li X, Lee Y-H, Lee YS, Sung K, Lu DS, Tsao T-C, Wu HH. MRI-Guided Targeted Needle Placement during Motion Using Hydrostatic Actuators. *Int J Med Robot* 2020;16(2):e2041. doi:10.1002/rcs.2041

67. Zamecnik P, Schouten MG, Krafft AJ, Maier F, Schlemmer H-P, Barentsz JO, Bock M, Fütterer JJ. Automated Real-Time Needle-Guide Tracking for Fast 3-T MR-Guided Transrectal Prostate Biopsy: A Feasibility Study. *Radiology* 2014;273(3):879-886. doi:10.1148/radiol.14132067

68. Tokuda J, Fischer GS, DiMaio SP, Gobbi DG, Csoma C, Mewes PW, Fichtinger G, Tempany CM, Hata N. Integrated Navigation and Control Software System for MRI-Guided Robotic Prostate Interventions. *Comput Med Imaging Graph* 2010;34(1):3-8. doi:10.1016/j.compmedimag.2009.07.004

69. Roujol S, Ries M, Quesson B, Moonen C, Denis de Senneville B. Real-Time MR-Thermometry and Dosimetry for Interventional Guidance on Abdominal Organs. *Magn Reson Med* 2010;63(4):1080-1087. doi:10.1002/mrm.22309

70. Ries M, de Senneville BD, Roujol S, Berber Y, Quesson B, Moonen C. Real-Time 3D Target Tracking in MRI Guided Focused Ultrasound Ablations in Moving Tissues. *Magn Reson Med* 2010;64(6):1704-1712. doi:10.1002/mrm.22548

71. Menten MJ, Wetscherek A, Fast MF. MRI-Guided Lung SBRT: Present and Future Developments. *Phys Med* 2017;44:139-149. doi:10.1016/j.ejmp.2017.02.003

72. Fischer-Valuck BW, Henke L, Green O, Kashani R, Acharya S, Bradley JD, Robinson CG, Thomas M, Zoberi I, Thorstad W, Gay H, Huang J, Roach M, Rodriguez V, Santanam L, Li H, Li H, Contreras J, Mazur T, Hallahan D, Olsen JR, Parikh P, Mutic S, Michalski J. Two-and-a-Half-Year Clinical Experience with the World's First Magnetic Resonance Image Guided Radiation Therapy System. *Adv Radiat Oncol* 2017;2(3):485-493. doi:10.1016/j.adro.2017.05.006

73. Heerkens HD, Van Vulpen M, Van Den Berg CAT, Tijssen RHN, Crijns SPM, Molenaar IQ, Van Santvoort HC, Reerink O, Meijer GJ. MRI-Based Tumor Motion Characterization and Gating Schemes for Radiation Therapy of Pancreatic Cancer. *Radiother Oncol* 2014;111(2):252-257. doi:10.1016/j.radonc.2014.03.002

74. Ge Y, O'Brien RT, Shieh CC, Booth JT, Keall PJ. Toward the Development of Intrafraction Tumor Deformation Tracking Using a Dynamic Multi-Leaf Collimator. *Med Phys* 2014;41(6). doi:10.1118/1.4873682

75. Shi X, Diwanji T, Mooney KE, Lin J, Feigenberg S, D'Souza WD, Mistry NN. Evaluation of Template Matching for Tumor Motion Management with Cine-MR Images in Lung Cancer Patients. *Med Phys* 2014;41(5). doi:10.1118/1.4870978

76. Bjerre T, Crijns S, Rosenschöld PMa, Aznar M, Specht L, Larsen R, Keall P. Three-Dimensional MRI-Linac Intra-Fraction Guidance Using Multiple Orthogonal Cine-MRI Planes. *Phys Med Biol* 2013;58(14):4943-4950. doi:10.1088/0031-9155/58/14/4943

77. Bourque AE, Bedwani S, Filion É, Carrier J-F. A Particle Filter Based Autocontouring Algorithm for Lung Tumor Tracking Using Dynamic Magnetic Resonance Imaging. *Med Phys* 2016;43(9):5161-5169. doi:10.1118/1.4961403

78. Acharya KA, Babu RV, Vadhiyar SS. A Real-Time Implementation of SIFT Using GPU. *J Real-Time Image Process* 2018;14(2):267–277. doi:10.1007/s11554-014-0446-6

79. Zachiu C, Papadakis N, Ries M, Moonen C, Senneville BDd. An Improved Optical Flow Tracking Technique for Real-Time MR-Guided Beam Therapies in Moving Organs. *Phys Med Biol* 2015;60(23):9003.

80. Mittauer K, Paliwal B, Hill P, Bayouth JE, Geurts MW, Baschnagel AM, Bradley KA, Harari PM, Rosenberg S, Brower JV, Wojcieszynski AP, Hullett C, Bayliss RA, Labby ZE, Bassetti MF. A New Era of Image Guidance with Magnetic Resonance-Guided Radiation Therapy for Abdominal and Thoracic Malignancies. *Cureus* 2018;10(4):e2422-e2422. doi:10.7759/cureus.2422

81. Green OL, Rankine LJ, Cai B, Curcuru A, Kashani R, Rodriguez V, Li HH, Parikh PJ, Robinson CG, Olsen JR, Mutic S, Goddu SM, Santanam L. First Clinical Implementation of Real-Time, Real Anatomy Tracking and Radiation Beam Control. *Med Phys* 2018;45(8):3728-3740. doi:10.1002/mp.13002

82. Lamb JM, Ginn JS, O'Connell DP, Agazaryan N, Cao M, Thomas DH, Yang Y, Lazea M, Lee P, Low DA. Dosimetric Validation of a Magnetic Resonance Image gated Radiotherapy System Using a Motion Phantom and Radiochromic Film. *J Appl Clin Med Phys* 2017;18(3):163-169. doi:10.1002/acm2.12088

83. Gopalakrishnan A, Kaisare NS, Narasimhan S. Incorporating Delayed and Infrequent Measurements in Extended Kalman Filter Based Nonlinear State Estimation. *J Process Control* 2011;21(1):119-129. doi:10.1016/j.jprocont.2010.10.013

84. Spincemaille P, Nguyen TD, Prince MR, Wang Y. Kalman Filtering for Real-Time Navigator Processing. *Magn Reson Med* 2008;60(1):158-168. doi:10.1002/mrm.21649

85. Fatehi A, Huang B. Kalman Filtering Approach to Multi-Rate Information Fusion in the Presence of Irregular Sampling Rate and Variable Measurement Delay. *J Process Control* 2017;53:15-25. doi:10.1016/j.jprocont.2017.02.010

86. Alexander HL. State Estimation for Distributed Systems with Sensing Delay. *Proc SPIE 1470, Data Structures and Target Classification* 1991. doi:10.1117/12.44843

87. Larsen TD, Andersen NA, Ravn O, Poulsen NK. Incorporation of Time Delayed Measurements in a Discrete-Time Kalman Filter. *Proc 37th IEEE Conference on Decision and Control* 1998;4:3972-3977 vol.3974. doi:10.1109/CDC.1998.761918

88. Digalakis V, Rohlicek JR, Ostendorf M. ML Estimation of a Stochastic Linear System with the EM Algorithm and its Application to Speech Recognition. *IEEE Trans on Speech and Audio Processing* 1993;1(4):431-442. doi:10.1109/89.242489

89. Li X, Mikaiel S, Simonelli J, Lee Y-h, Tsao T-c, Wu HH. Real-Time Motion Prediction for Feedback Control of MRI-Guided Interventions. *Proc ISMRM 25th Annual Meeting* 2017:5540.

90. Wu HH, Gurney PT, Hu BS, Nishimura DG, McConnell MV. Free-breathing Multiphase Whole-Heart Coronary MR Angiography Using Image-Based Navigators and Three-Dimensional Cones Imaging. *Magn Reson Med* 2013;69(4):1083-1093. doi:10.1002/mrm.24346

91. Foroosh H, Zerubia JB, Berthod M. Extension of Phase Correlation to Subpixel Registration. *IEEE Trans Image Process* 2002;11(3):188-200. doi:10.1109/83.988953

92. Bernstein MA, Fain SB, Riederer SJ. Effect of Windowing and Zero-Filled Reconstruction of MRI Data on Spatial Resolution and Acquisition Strategy. *J Magn Reson Imaging* 2001;14(3):270-280. doi:10.1002/jmri.1183

93. Adelson E, Anderson C, Bergen J, Burt P, Ogden J. Pyramid Methods in Image Processing. *RCA Eng* 1983;29.

94. Simonelli J, Lee Y-H, Mikaiel S, Chen C-W, Li X, Sung K, Lu D, Wu H, Tsao T-C. An MR-Compatible Stage for Respiratory Motion Emulation. *Proc International Federation of Automatic Control* 2017;50(1):6073-6078. doi:10.1016/j.ifacol.2017.08.1381

95. Sørensen TS, Atkinson D, Schaeffter T, Hansen MS. Real-Time Reconstruction of Sensitivity Encoded Radial Magnetic Resonance Imaging Using a Graphics Processing Unit. *IEEE Trans Med Imaging* 2009;28(12):1974-1985. doi:10.1109/TMI.2009.2027118

96. Rempp H, Loh H, Hoffmann R, Rothgang E, Pan L, Claussen CD, Clasen S. Liver Lesion Conspicuity during Real-Time MR-Guided Radiofrequency Applicator Placement Using Spoiled Gradient Echo and Balanced Steady-State Free Precession Imaging. *J Magn Reson Imaging* 2014;40(2):432-439. doi:10.1002/jmri.24371

97. Barth MM, Smith MP, Pedrosa I, Lenkinski RE, Rofsky NM. Body MR Imaging at 3.0 T: Understanding the Opportunities and Challenges. *Radiographics* 2007;27(5):1445-1462. doi:10.1148/rg.275065204

98. Crawley AP, Wood ML, Henkelman RM. Elimination of Transverse Coherences in FLASH MRI. *Magn Reson Med* 1988;8(3):248-260. doi:10.1002/mrm.1910080303

99. Ingle RR, Wu HH, Addy NO, Cheng JY, Yang PC, Hu BS, Nishimura DG. Nonrigid Autofocus Motion Correction for Coronary MR Angiography with a 3D Cones Trajectory. *Magn Reson Med* 2014;72(2):347-361. doi:10.1002/mrm.24924

100. Seibert TM, White NS, Kim G-Y, Moiseenko V, McDonald CR, Farid N, Bartsch H, Kuperman J, Karunamuni R, Marshall D, Holland D, Sanghvi P, Simpson DR, Mundt AJ, Dale AM, Hattangadi-Gluth JA. Distortion Inherent to Magnetic Resonance Imaging can Lead to Geometric Miss in Radiosurgery Planning. *Pract Radiat Oncol* 2016;6(6):e319-e328. doi:10.1016/j.prro.2016.05.008

101. Sümbül U, Santos JM, Pauly JM. A Practical Acceleration Algorithm for Real-Time Imaging. *IEEE Trans Med Imaging* 2009;28(12):2042-2051. doi:10.1109/TMI.2009.2030474

102. Schaetz S, Voit D, Frahm J, Uecker M. Accelerated Computing in Magnetic Resonance Imaging: Real-Time Imaging Using Nonlinear Inverse Reconstruction. *Comput Math Methods Med* 2017;2017:3527269-3527269. doi:10.1155/2017/3527269

103. Zhou Z, Han F, Ghodrati V, Gao Y, Yin W, Yang Y, Hu P. Parallel Imaging and Convolutional Neural Network Combined Fast MR Image Reconstruction: Applications in Low-Latency Accelerated Real-Time Imaging. *Med Phys* 2019;46(8):3399-3413. doi:10.1002/mp.13628

104. Hauptmann A, Arridge S, Lucka F, Muthurangu V, Steeden JA. Real-Time Cardiovascular MR with Spatio-Temporal Artifact Suppression Using Deep Learning-Proof of Concept in Congenital Heart Disease. *Magn Reson Med* 2019;81(2):1143-1156. doi:10.1002/mrm.27480

105. Görlitz RA, Tokuda J, Hoge SW, Chu R, Panych LP, Tempany C, Hata N. Development and Validation of a Real-Time Reduced Field of View Imaging Driven by Automated Needle Detection for MRI-Guided interventions. *SPIE Medical Imaging* 2010;7625:762515-762519. doi:10.1117/12.840837

106. DiMaio SP, Samset E, Fischer G, Iordachita I, Fichtinger G, Jolesz F, Tempany CM. Dynamic MRI Scan Plane Control for Passive Tracking of Instruments and Devices. *Medical image computing and computer-assisted intervention (MICCAI)* 2007:50-58. doi:10.1007/978-3-540-75759-7_7

107. P DiMaio S, Kacher D, Ellis R, Fichtinger G, Hata N, Zientara G, Panych L, Kikinis R, Jolesz F. Needle Artifact Localization in 3T MR Images. *Stud Health Technol Inform* 2006;119:120-125.

108. Verma S, Choyke PL, Eberhardt SC, Oto A, Tempany CM, Turkbey B, Rosenkrantz AB. The Current State of MR Imaging–Targeted Biopsy Techniques for Detection of Prostate Cancer. *Radiology* 2017;285(2):343-356. doi:10.1148/radiol.2017161684

109. Moore CM, Robertson NL, Arsanious N, Middleton T, Villers A, Klotz L, Taneja SS, Emberton M. Image-Guided Prostate Biopsy Using Magnetic Resonance Imaging–Derived Targets: A Systematic Review. *Eur Urol* 2013;63(1):125-140. doi:10.1016/j.eururo.2012.06.004

110. Ladd ME, Erhart P, Debatin JF, Romanowski BJ, Boesiger P, McKinnon GC. Biopsy needle susceptibility artifacts. *Magn Reson Med* 1996;36(4):646-651. doi:10.1002/mrm.1910360423

111. Zijlstra F, Viergever MA, Seevinck PR. SMART Tracking: Simultaneous Anatomical Imaging and Real-Time Passive Device Tracking for MR-Guided Interventions. *Phys Med* 2019;64:252-260. doi:10.1016/j.ejmp.2019.07.019

112. Ho M, Kim Y, Cheng SS, Gullapalli R, Desai JP. Design, Development, and Evaluation of an MRI-Guided SMA Spring-Actuated Neurosurgical Robot. *Int J Rob Res* 2015;34(8):1147-1163. doi:10.1177/0278364915579069

113. Bergeles C, Vartholomeos P, Qin L, Dupont PE. Closed-Loop Commutation Control of an MRI-Powered Robot Actuator. *Proc IEEE International Conference on Robotics and Automation* 2013:698-703. doi:10.1109/ICRA.2013.6630649

114. Moreira P, Patel N, Wartenberg M, Li G, Tuncali K, Heffter T, Burdette EC, Iordachita I, Fischer GS, Hata N, Tempany CM, Tokuda J. Evaluation of Robot-Assisted MRI-Guided Prostate Biopsy: Needle Path Analysis during Clinical Trials. *Phys Med Biol* 2018;63(20):20NT02. doi:10.1088/1361-6560/aae214

115. Mwikirize C, Nosher JL, Hacihaliloglu I. Convolution Neural Networks for Real-Time Needle Detection and Localization in 2D Ultrasound. *Int J Comput Assist Radiol Surg* 2018;13(5):647-657. doi:10.1007/s11548-018-1721-y

116. Uherčík M, Kybic J, Liebgott H, Cachard C. Model Fitting Using RANSAC for Surgical Tool Localization in 3-D Ultrasound Images. *IEEE Trans Biomed Eng* 2010;57(8):1907-1916. doi:10.1109/TBME.2010.2046416

117. Goodfellow I, Bengio Y, Courville A. Deep Learning. Boston, US: MIT Press; 2016.

118. Pourtaherian A, Ghazvinian Zanjani F, Zinger S, Mihajlovic N, Ng G, Korsten H, de With P. Improving Needle Detection in 3D Ultrasound Using Orthogonal-Plane Convolutional

Networks. *Medical Image Computing and Computer-Assisted Intervention (MICCAI)* 2017:610-618. doi:10.1007/978-3-319-66185-8_69

119. He K, Gkioxari G, Dollár P, Girshick R. Mask R-CNN. *Proc IEEE International Conference on Computer Vision (ICCV)* 2017:2980-2988. doi:10.1109/ICCV.2017.322

120. Li X, Raman SS, Lu D, Lee Y-h, Tsao T-c, Wu HH. Real-Time Needle Detection and Segmentation Using Mask R-CNN for MRI-Guided interventions. *Proc ISMRM 27th Annual Meeting* 2019:972.

121. Li X, Lee Y, Mikaiel S, Simonelli J, Tsao T, Wu HH. Respiratory Motion Prediction Using Fusion-Based Multi-Rate Kalman Filtering and Real-Time Golden-Angle Radial MRI. *IEEE Trans Biomed Eng* 2020;67(6):1727-1738. doi:10.1109/TBME.2019.2944803

122. Lin T-Y, Maire M, Belongie S, Hays J, Perona P, Ramanan D, Dollár P, Zitnick CL. Microsoft COCO: Common Objects in Context. *Computer Vision - ECCV* 2014:740-755.

123. Yosinski J, Clune J, Bengio Y, Lipson H. How Transferable are Features in Deep Neural Networks? *NeurIPS* 2014:3320-3328.

124. Abdulla W. Mask R-CNN for Object Detection and Instance Segmentation on Keras and TensorFlow. *GitHub repository* 2017.

125. Boggs PT, Rogers JE. Orthogonal Distance Regression. *Contemp Math* 1990;112:183-194. doi:10.6028/nist.ir.89-4197

126. Patel NA, Katwijk Tv, Li G, Moreira P, Shang W, Misra S, Fischer GS. Closed-Loop Asymmetric-Tip Needle Steering under Continuous Intraoperative MRI Guidance. *Proc 37th Annual International Conference of the IEEE Engineering in Medicine and Biology Society (EMBC)* 2015:4869-4874. doi:10.1109/EMBC.2015.7319484

127. Stamey TA, Freiha FS, McNeal JE, Redwine EA, Whittemore AS, Schmid HP. Localized Prostate Cancer. Relationship of Tumor Volume to Clinical Significance for Treatment of Prostate Cancer. *Cancer* 1993;71(3 Suppl):933-938.

128. Renfrew M, Griswold M, Çavuşoĝlu MC. Active Localization and Tracking of Needle and Target in Robotic Image-Guided Intervention Systems. *Auton Robots* 2018;42(1):83-97. doi:10.1007/s10514-017-9640-2

129. Li X, Young AS, Raman SS, Lu DS, Lee Y-H, Tsao T-C, Wu HH. Automatic Needle Tracking Using Mask R-CNN for MRI-Guided Percutaneous Interventions. *Int J Comput Assist Radiol Surg* 2020;15(10):1673-1684. doi:10.1007/s11548-020-02226-8

130. P DiMaio S, Kacher D, Ellis R, Fichtinger G, Hata N, Zientara G, Panych L, Kikinis R, Jolesz F. Needle Artifact Localization in 3T MR Images. *Stud Health Technol Inform* 2006;119:120-125.

131. Li X, Lee Y-h, Lu D, Tsao T-c, Wu HH. Deep Learning-Driven Automatic Scan Plane Alignment for Needle Tracking in MRI-GuidedInterventions. *Proc ISMRM 29th Annual Meeting* 2021:0861.

132. Müller-Bierl B, Graf H, Lauer U, Steidle G, Schick F. Numerical Modeling of Needle Tip Artifacts in MR Gradient Echo Imaging. *Med Phys* 2004;31(3):579-587. doi:10.1118/1.1640971

133. Liu T, Spincemaille P, de Rochefort L, Kressler B, Wang Y. Calculation of Susceptibility Through Multiple Orientation Sampling (COSMOS): A Method for Conditioning the Inverse Problem from Measured Magnetic Field Map to Susceptibility Source Image in MRI. *Magn Reson Med* 2009;61(1):196-204. doi:10.1002/mrm.21828

134. Rothgang E, Gilson WD, Strehl W, Pan L, Roland J, Lorenz CH, Hornegger J. Interventional MR-Imaging for Thermal Ablation Therapy. *Proc IEEE International Symposium on Biomedical Imaging: From Nano to Macro* 2011:1864-1868. doi:10.1109/ISBI.2011.5872771

135. Salomir R, de Senneville BD, Moonen CTW. A Fast Calculation Method for Magnetic Field Inhomogeneity due to an Arbitrary Distribution of Bulk Susceptibility. *Concepts Magn Reson Part B Magn Reson Eng* 2003;19B(1):26-34. doi:10.1002/cmr.b.10083

136. Fessler JA, Sutton BP. Nonuniform Fast Fourier Transforms Using Min-Max Interpolation. *IEEE Trans Signal Process* 2003;51(2):560-574. doi:10.1109/TSP.2002.807005

137. Park Y, Elayaperumal S, Daniel B, Ryu SC, Shin M, Savall J, Black RJ, Moslehi B, Cutkosky MR. Real-Time Estimation of 3-D Needle Shape and Deflection for MRI-Guided Interventions. *IEEE/ASME Trans Mechatronics* 2010;15(6):906-915. doi:10.1109/TMECH.2010.2080360

138. Franco E, Ristic M, Rea M, Gedroyc WMW. Robot-Assistant for MRI-Guided Liver Ablation: A Pilot Study. *Med Phys* 2016;43(10):5347-5356. doi:10.1118/1.4961986

139. Hata N, Song S-E, Olubiyi O, Arimitsu Y, Fujimoto K, Kato T, Tuncali K, Tani S, Tokuda J. Body-Mounted Robotic Instrument Guide for Image-Guided Cryotherapy of Renal Cancer. *Med Phys* 2016;43(2):843-853. doi:10.1118/1.4939875

140. Song S-E, Cho NB, Iordachita II, Guion P, Fichtinger G, Kaushal A, Camphausen K, Whitcomb LL. Biopsy Needle Artifact Localization in MRI-Guided Robotic Transrectal Prostate Intervention. *IEEE Trans Biomed Eng* 2012;59(7):1902-1911. doi:10.1109/TBME.2012.2192118

141. Pour Arab D, Voros S, Essert C. Dynamic Path Planning for Percutaneous Procedures in the Abdomen during Free Breathing. *Int J Comput Assist Radiol Surg* 2020;15(7):1195-1203. doi:10.1007/s11548-020-02153-8

142. Li G, Liu Y, Nie X. Respiratory-Correlated (RC) vs. Time-Resolved (TR) Four-Dimensional Magnetic Resonance Imaging (4DMRI) for Radiotherapy of Thoracic and Abdominal Cancer. *Front Oncol* 2019;9:1024. doi:10.3389/fonc.2019.01024

143. Nonomura T, Shibata H, Takaki R. Extended-Kalman-Filter-Based Dynamic Mode Decomposition for Simultaneous System Identification and Denoising. *PLoS One* 2019;14(2):e0209836. doi:10.1371/journal.pone.0209836

144. Ha IY, Wilms M, Handels H, Heinrich MP. Model-Based Sparse-to-Dense Image Registration for Realtime Respiratory Motion Estimation in Image-Guided Interventions. *IEEE Trans Biomed Eng* 2019;66(2):302-310. doi:10.1109/TBME.2018.2837387

145. Stemkens B, Paulson ES, Tijssen RHN. Nuts and Bolts of 4D-MRI for Radiotherapy. *Phys Med Biol* 2018;63(21):21TR01. doi:10.1088/1361-6560/aae56d

146. Neumann M. Automatic Multimodal Real-Time Tracking for Image Plane Alignment in Interventional Magnetic Resonance Imaging: Université de Strasbourg; 2014.

147. Elayaperumal S, Plata JC, Holbrook AB, Park Y, Pauly KB, Daniel BL, Cutkosky MR. Autonomous Real-Time Interventional Scan Plane Control With a 3-D Shape-Sensing Needle. *IEEE Trans Med Imaging* 2014;33(11):2128-2139. doi:10.1109/TMI.2014.2332354

148. Blansit K, Retson T, Masutani E, Bahrami N, Hsiao A. Deep Learning–Based Prescription of Cardiac MRI Planes. *Radiology: Artificial Intelligence* 2019;1(6):e180069. doi:10.1148/ryai.2019180069

149. Zhao P, Zhang J, Fang W, Deng S. SCAU-Net: Spatial-Channel Attention U-Net for Gland Segmentation. *Front Bioeng Biotechnol* 2020;8(670). doi:10.3389/fbioe.2020.00670

150. Welch G, Bishop G. An introduction to the Kalman Filter: Siggraph Course; 2001.